NASA
Technical
Paper
2717

July 1987

Effect of a Trade Between Boattail Angle and Wedge Size on the Performance of a Nonaxisymmetric Wedge Nozzle

George T. Carson, Jr.,
E. Ann Bare, and
James R. Burley II

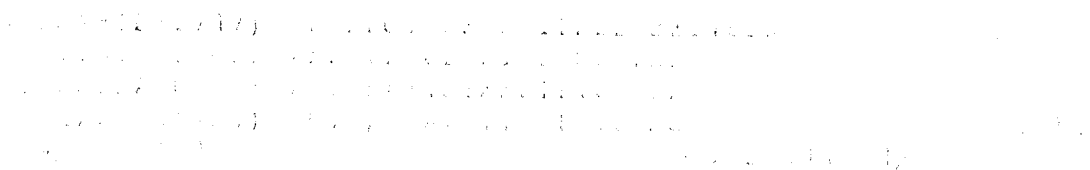

NASA

NASA Technical Paper 2717

1987

Effect of a Trade Between Boattail Angle and Wedge Size on the Performance of a Nonaxisymmetric Wedge Nozzle

George T. Carson, Jr.,
E. Ann Bare, and
James R. Burley II

Langley Research Center
Hampton, Virginia

National Aeronautics and Space Administration

Scientific and Technical Information Office

Summary

An investigation was conducted in the Langley 16-Foot Transonic Tunnel to determine the effect of a boattail-angle and wedge-size trade on the performance of nonaxisymmetric wedge nozzles installed on a generic twin-engine fighter aircraft model. Test data were obtained at static conditions and at Mach numbers from 0.60 to 1.25. Angle of attack was held constant at 0°. High-pressure air was used to simulate jet exhaust, and the nozzle pressure ratio was varied from 1.0 (jet off) to slightly over 15.0. In this study as the size of the wedge was reduced, the external boattail angle had to increase, since constant nozzle throat and exit areas were maintained. Three nozzles were each tested in the dry power mode and the afterburning power mode. For the configurations tested, results indicated that wedge size could be reduced without significantly affecting aeropropulsive performance.

Introduction

The mission requirements for the next generation of fighter aircraft may dictate a highly versatile vehicle capable of operating over a wide range of flight conditions. This range of design characteristics may include efficient supersonic cruise capability, at least current levels of maneuverability, and short takeoff and landing performance. These capabilities require the designer to employ emerging technological concepts such as close-coupled canards, relaxed static stability, active controls, vortex control, and multifunction nozzles with thrust vectoring and reversing.

During the last decade many studies on multifunctional nonaxisymmetric nozzles have been conducted. (See refs. 1 to 15 for example.) Three nozzle concepts have been the primary focus of attention: the convergent-divergent nozzle, the single expansion ramp nozzle, and the wedge nozzle. System studies where these nozzles have been integrated into several current high-performance aircraft have been conducted (refs. 16 to 25). The results have pointed out both the advantages and disadvantages of these unique nozzles. The advantages are primarily associated with the increase in performance and system effectiveness gained through the more efficient integration of these nozzles into the aircraft and through the utilization of thrust vectoring and thrust reversing. The primary disadvantage of these nozzles is high weight, especially for the wedge nozzle (ref. 25). In fact, the weight associated with the original large-wedge concept essentially eliminated this nozzle from consideration in the high-performance aircraft of today. If, however, the size of the wedge could be reduced without reducing the performance, then this nozzle may be of significant interest. To reduce the size of the wedge while maintaining constant nozzle throat and exit areas requires an increase in external boattail angle. This study was initiated to determine the transonic performance of a nonaxisymmetric wedge nozzle with this geometric trade between decreased wedge size and increased boattail angle. Therefore, an investigation was conducted in the Langley 16-Foot Transonic Tunnel which measured the effect of a boattail-angle and wedge-size trade on the performance of nonaxisymmetric wedge nozzles installed on a generic twin-engine fighter aircraft model. Test data were obtained at static conditions and at Mach numbers from 0.60 to 1.25. Angle of attack was held constant at 0°. High-pressure air was used to simulate jet exhaust, and the nozzle pressure ratio was varied from 1.0 (jet off) to slightly over 15.0. Three nozzles were each tested in the dry power mode and the afterburning power mode.

Symbols

The stability axis system was used as the reference for model forces. Dimensions are given in the International System of Units (SI). Aerodynamic coefficients are nondimensionalized with respect to the free-stream dynamic pressure and wing area of the model except at static conditions, for which atmospheric pressure is substituted for the free-stream dynamic pressure.

A_e	nozzle exit area, cm^2 (see fig. 5)
A_{max}	maximum cross-sectional area of model, cm^2 (see fig. 5)
A_{seal}	cross-sectional area enclosed by seal strip at FS 113.67 cm, cm^2 (see fig. 2)
A_t	nozzle throat area, cm^2 (see fig. 5)
AR	nozzle throat aspect ratio, $\frac{b_n^2}{A_t}$
b_n	nozzle span, 10.92 cm (see fig. 7)
$C_{D,n}$	nozzle drag coefficient
C_p	pressure coefficient, $\frac{p-p_\infty}{q_\infty}$
$\bar{c}$	wing mean geometric chord, 44.42 cm
D_f	skin-friction drag, N
D_n	nozzle drag, N
$F_{A,bal}$	axial force measured by balance, positive forward, N
$F_{A,mom}$	momentum tare axial force due to bellows, N
F_i	ideal isentropic gross thrust, N

F_j	thrust along body axis, N
h_w	wedge height from centerline, cm (see fig. 5)
l_n	length from nozzle throat to wedge trailing edge, cm (see fig. 5)
l_w	length of wedge, cm (see fig. 5)
M	free-stream Mach number
$\dot{m}$	measured mass-flow rate, kg/sec
$\dot{m}_i$	ideal mass-flow rate, kg/sec
NPR	nozzle pressure ratio, $p_{t,j}/p_a$ for $M = 0$ and $p_{t,j}/p_\infty$ for $M > 0$
p	local static pressure, Pa
p_a	atmospheric pressure, Pa
p_i	internal body cavity static pressure, Pa
p_s	average external static pressure at metric break, Pa
$p_{t,j}$	jet total pressure, Pa
p_∞	free-stream static pressure, Pa
q_∞	free-stream dynamic pressure, Pa
R	ideal gas constant for air, 287.3 J/kg-K
$T_{t,j}$	jet total temperature, K
x	axial distance from baseline (forward-thrust) nozzle throat, positive downstream, cm (see fig. 7)
y	lateral distance measured from nozzle centerline, positive to the right looking upstream, cm (see fig. 7)
β	nozzle boattail angle, deg
γ	ratio of specific heats, 1.3997 for air at 300 K
θ_w	nozzle wedge half-angle, deg

Subscripts:

A/B	afterburning power setting
D	dry power setting

Abbreviations:

ASME	American Society of Mechanical Engineers
BL	buttock line, cm
FS	fuselage station, cm
WL	waterline, cm

Apparatus and Procedure

Wind Tunnel

This investigation was conducted in the Langley 16-Foot Transonic Tunnel. This facility is a single-return, continuous-flow, exchange-air-cooled, atmospheric-pressure wind tunnel with an octagonal, slotted-throat test section. It has a continuously variable air speed up to a Mach number of 1.30. A detailed description of this wind tunnel is given in reference 26.

Models and Support System

A set of six nonaxisymmetric wedge nozzles were installed on a wingtip-supported model simulating a generic twin-engine fighter aircraft without empennage surfaces. A photograph of this wind-tunnel model installed in the 16-Foot Transonic Tunnel is shown in figure 1. A detailed sketch of the aircraft-nozzle model and support system is shown in figure 2. The support system for the wedge nozzle consisted of three major components: the wingtip support booms, the forebody, and the wing-centerbody combination. The forebody approximated the forward fuselage of a high-performance aircraft with faired-over inlets. The centerbody had a constant height and width of 12.70 cm and 25.40 cm and had rounded corners of 2.54-cm radius, which resulted in a model maximum cross-sectional area of 317.04 cm^2. The wing, whose half-span planform geometry is shown in figure 3, was mounted on the fuselage centerbody in a high position. (See fig. 1.) It had an aspect ratio of 2.40, a taper ratio of 0.43, and a cranked trailing edge. The NACA 64-series airfoil had a thickness ratio of 0.067 near the wing root to provide a realistic wake on the afterbody. However, outboard on the wing, from BL 27.94 cm to the support booms, it was necessary to increase the thickness ratio from 0.077 to 0.100 for structural support and for compressed air and instrumentation passages.

The metric portion of the model (aft of FS 113.67 cm), which consisted of the propulsion system, the afterbody, and the nozzles, was supported by a strain-gage force balance. The afterbody lines were chosen to provide a length of constant cross section aft of the nonmetric centerbody and to enclose the balance and jet simulation system apparatus while fairing smoothly downstream into the closely spaced nozzles. A clearance gap formed the metric break at station 113.67; the gap separated the nonmetric and metric portions of the model to prevent fouling. A flexible plastic strip was inserted into

machined grooves in each component to impede flow into or out of the internal model cavity.

Twin-Jet-Propulsion Simulation System

For jet-propulsion simulation, the Langley 16-Foot Transonic Tunnel is equipped with an external high-pressure air system that provides a continuous flow of clean, dry air at a nominal controlled temperature of 300 K ahead of the nozzle throat. Two remotely operated flow-regulating valves were used to balance the jet total pressure in the left- and right-hand nozzles. The airflow path can be traced by using the sketch in figure 2. Compressed air flowed through the wingtip support booms, then through passages in the wing and into two flow-transfer bellows assemblies. The bellows assemblies, one of which is shown in figure 4, provided the means of transferring compressed air from the nonmetric to the metric portion of the model. In order to eliminate incoming axial momentum, air was discharged radially through eight equally spaced sonic nozzles. Two flexible metal convolutions (bellows) served as seals. The airflow then passed successively through a tailpipe, a circular-to-rectangular transition section, a choke plate, and an instrumentation section and then expanded through the nozzle configuration being tested. (See fig. 2.)

Design Rationale of the Nozzle Models

In order to provide data within a realistic geometric range for the proposed family of nonaxisymmetric wedge nozzles, the following initial design values were set: nozzle boattail angles of 7°, 10°, and 12°; dry power setting wedge half-angle of 13°; afterburning power setting wedge half-angles of 7°, 8°, and 9° (see fig. 5 and table 1); sidewall angle of 5°; and $2A_t/A_{max} = 0.13$ (typical of twin-engine fighter aircraft). These nozzles were to be designed to be used on the generic twin-engine fighter aircraft wing-body model described in reference 2. The geometry of this model, in turn, dictated the nozzle span and dry power setting throat area and aspect ratio. In order to assure a smooth transition from the upstream stagnation plenum to the nozzle throat, an elliptical area distribution was used, i.e., working forward from the known throat area at a Mach number of unity to an estimated Mach number of 0.15, the flow area versus axial station was calculated from the equation of an ellipse. This flow area was formed by contouring the wedge forward section and the shroud interior. (See fig. 5.)

The afterburning power setting nozzles were considered to simulate a geometry in which the wedge was collapsed in order to increase throat area. Therefore, the shrouds of the companion dry and afterburning power setting nozzles are the same. The afterburning power setting aspect ratio was determined from the relationship $AR_D\left(\frac{AR_{A/B}}{AR_D}\right)$, where the second term represents the aspect ratios calculated by the method of reference 2. This determined the throat area and, therefore, the wedge size. Although the wedge length of each configuration was fixed, the wedge half-angle was allowed to vary as required, and the wedge upstream contour was calculated for an elliptic area distribution.

Table 1 gives the nozzle design parameters, and the sketches of figure 5 show the geometric details of these nozzles. The photographs of figure 6 show the nozzles with their left sidewalls removed.

Instrumentation

Forces on the metric portions of the model were measured with a six-component strain-gage balance. The balance connected the nonmetric wing-centerbody combination and the metric aft-end model parts and measured forces (external and internal) on the nozzles and the afterbody.

Jet exhaust conditions were measured in an instrumentation section upstream of each nozzle at FS 150.18 cm. This instrumentation consisted of a total-temperature probe and a total-pressure rake in each section. These total-pressure rakes contained four total-pressure probes as shown in figure 2.

Eight static pressures were measured in the gap at the metric break (FS 113.67 cm) external to the plastic seal strip. All orifices were located on the nonmetric centerbody and spaced symmetrically around the model perimeter. Also, two internal pressures were measured at the fuselage station where the metric break was located. All the aforementioned pressures were used for pressure-area corrections to the balances as described in the "Data Reduction" section.

Table 2 gives the locations of external and internal nozzle pressure orifices. The orientation of these orifices and the identification of the model components are indicated in figure 7.

Mass-flow rate was measured by using the multiple critical venturi system described in reference 27.

Data Reduction

All data from the instrumentation of the aircraft-nozzle model and the wind-tunnel facility were recorded simultaneously on magnetic tape. For each data point, 50 frames of data were taken over a period of 5 sec and the average value was used for

computation. The recorded data were used to compute standard force and pressure coefficients. All force coefficients in this report are referenced to the model wing surface area.

The balance (see fig. 2) measured thrust and aerodynamic forces on the metric portion (afterbody and nozzles) of the model. Force interactions existed between the balance and the bellows (flow-transfer) system because of the balance offset from the model centerline. (See fig. 2.) Consequently, single and combined normal-force calibrations were performed to determine these interactions with and without the jets operating. The determination of these interactions was similar to the method outlined in the appendix of reference 15.

Thrust minus drag was computed from the balance axial force by using the following relationship:

$$F_j - D_n = F_{A,\mathrm{bal}} + (p_s - p_\infty)(A_{\max} - A_{\mathrm{seal}}) + (p_i - p_\infty) A_{\mathrm{seal}} - F_{A,\mathrm{mom}} + D_f$$

The first term, $F_{A,\mathrm{bal}}$, is the total axial force measured with the balance and corrected for the bellows interaction discussed earlier. The second term, $(p_s - p_\infty)(A_{\max} - A_{\mathrm{seal}})$, is the correction for the pressure-area force in the metric break gap at FS 113.67 cm. The third term, $(p_i - p_\infty) A_{\mathrm{seal}}$, is the correction for the pressure-area force caused by the difference between internal-cavity and free-stream pressure. The term $F_{A,\mathrm{mom}}$, which ideally should be zero, is an exhaust flow momentum tare correction and is a function of the bellows internal pressure, which is a function of the chamber pressure in the supply pipes just ahead of the sonic nozzles. It was correlated with chamber pressure by static tests ($M = 0$) by using ASME standard calibration nozzles (ref. 28) for which F_j/F_i was known for a wide range of chamber pressure. The last term, D_f, is the computed skin-friction drag of the model afterbody section from FS 113.67 cm to FS 149.61 cm. This friction term was computed from the flat-plate formula for turbulent, compressible boundary layers given in reference 29 and was added to the axial-force measurement in order to eliminate afterbody (nonnozzle) drag. For jet-off runs, the thrust-minus-drag equation reduces to the drag of the nozzles. Since the afterbody section is cylindrical, it does not contribute any pressure drag to the drag of the vehicle.

The ideal isentropic gross thrust F_i, which was used to evaluate measured performance, is defined as

$$F_i = \dot{m} \left\{ \frac{2\gamma}{\gamma - 1} R T_{t,j} \left[1 - \left(\frac{p_\infty}{p_{t,j}} \right)^{\frac{\gamma - 1}{\gamma}} \right] \right\}^{1/2}$$

where $\dot{m}$ is the mass-flow rate measured by the multiple critical venturi system (ref. 27).

Test Conditions

This investigation was conducted in the Langley 16-Foot Transonic Tunnel at static conditions ($M = 0$) and at free-stream Mach numbers from 0.60 to 1.25. The nozzle pressure ratio was varied from 1.0 (jet off) to slightly over 15.0, depending on free-stream Mach number. The angle of attack was held at 0° for all tests.

In accordance with the criteria of reference 30 boundary-layer transition strips were used to ensure a turbulent boundary layer over the afterbody and the nozzles. A 0.254-cm-wide strip of No. 120 silicon carbide grit, sparsely distributed in a lacquer film, was located 2.54 cm from the nose of the forebody and proportionally along the wing at 5 percent of the root chord and 10 percent of the tip chord. The average Reynolds number per meter varied from 7.0×10^6 to 13.5×10^6.

Presentation of Results

The results of this investigation are presented graphically in figures 8 to 18. Figures 8 to 11 present thrust data; figure 12 presents nozzle drag data; and figures 13 to 18 present pressure distribution data. An index relating the nozzle configurations to thrust, nozzle drag, and pressure distribution data figures is given in table 3.

Discussion

Static and Aeropropulsive Performance

Dry power nozzles. The static performance F_j/F_i and discharge coefficient $\dot{m}/\dot{m}_i$ for the dry power nozzles (configurations 1 Dry, 2 Dry, and 3 Dry) are presented in figure 8. As indicated by these data, the static performance for all three configurations was essentially the same. This is to be expected since the nozzle throat area A_t and internal expansion ratio A_e/A_t remained constant. The discharge coefficient for configuration 3 Dry was significantly higher than the discharge coefficient for either configuration 1 Dry or 2 Dry. It is believed that the higher value resulted from the increased radius of the forward portion of the wedge, which reduced the losses in the nozzle duct.

The aeropropulsive performance for the dry power nozzles at Mach numbers from 0.6 to 1.2 is presented in figure 9. The thrust-minus-drag performance for these nozzles was essentially the same at each subsonic Mach number. (See figs. 9(a) to 9(d).) The pressure data for these configurations are presented

in figures 13 to 15. The pressure distribution on the wedge, though indicating flow separation, was very similar for all the dry power configurations at a given subsonic Mach number. As on the wedge, the pressure distribution on the external shroud was similar for the three configurations. There could be an indication of possible flow separation near the aft end of the boattail; however, there were too few pressure taps to state for sure if flow separation occurred, and there was no obvious effect between configurations on the thrust-minus-drag data. That is, the decrease in wedge size and corresponding increase in boattail angle had essentially no effect on the nozzle thrust-minus-drag performance.

At a Mach number of 1.2, configuration 3 Dry, the nozzle with the lowest boattail angle and the largest wedge, had the highest thrust-minus-drag performance. (See fig. 9(e).) Since the internal performance of the nozzles was the same, this higher thrust-minus-drag performance must have been the result of lower external drag for this configuration. Comparing part (e) of figures 13 to 15 again shows a similar pressure distribution between configurations, both on the shroud and on the wedge. Configuration 3 Dry had the lowest boattail angle and therefore the least rearward facing projected area over which the pressure acts, which accounts for the lower supersonic drag.

Afterburning power nozzles. The static performance F_j/F_i and discharge coefficient $\dot{m}/\dot{m}_i$ for the afterburning power nozzle configurations 1 A/B, 2 A/B, and 3 A/B are presented in figure 10. As with the dry power nozzles, results show that there was very little difference in the internal performance characteristics of the three configurations. The thrust-minus-drag characteristics presented in figure 11 also show only a small difference in the aeropropulsive characteristics at subsonic speeds. However, configuration 3 A/B had consistently lower performance at subsonic Mach numbers. (See figs. 11(a) to (d).) The pressure distributions for these configurations are shown in figures 16 to 18. Comparing configurations 1 A/B and 3 A/B at subsonic Mach numbers (see figs. 16(c) and 18(c) for example) shows that the pressure recovery on the external shroud (boattail) was less for the 3 A/B configuration. This lower pressure recovery resulted in a higher nozzle drag. The pressure distribution on the wedge was also very similar for the three configurations, but unlike the dry power nozzles it was necessary to slightly change the wedge half-angle in order to maintain constant throat and exit areas. Configuration 3 A/B had the largest wedge half-angle, and the pressures acting on the wedge could have also been a contributing factor to the lower performance.

At a Mach number of 1.2, configuration 1 A/B had significantly lower thrust-minus-drag performance than either 2 A/B or 3 A/B, which had essentially the same performance. As nozzle pressure ratio was increased these differences tended to disappear, such that at an operating pressure ratio typical of current engines (NPR of 5 to 6) for this Mach number, the thrust-minus-drag performance was nearly the same. Comparing the pressure data for the three configurations (figs. 16(e), 17(e), and 18(e)) shows that the performance difference appears to be caused by a combination of flow separation and pressure recovery on the nozzle boattail. All three configurations exhibited flow separation over most of the external shroud at the lower NPR values. As NPR was increased, the flow separation decreased. Configuration 3 A/B had separated flow over a larger portion of the boattail than did configuration 1 A/B, which would tend to increase the drag. However, configuration 3 A/B had a higher pressure recovery, which would decrease drag; the two factors tended to bring the overall thrust-minus-drag performance to approximately the same level as NPR was increased. Although all the configurations exhibited lower performance levels than desired, the data did show that for this design the wedge size could be reduced without significantly affecting the aeropropulsive performance.

Jet-Off Performance

Dry power nozzles. The variation of nozzle drag with Mach number for the dry power nozzle configurations at an angle of attack of 0° is presented in figure 12(a). At subsonic speed, increasing the wedge length and thickness reduced the external boattail angle and resulted in a higher nozzle drag. Although the larger nozzle would have a higher skin-friction drag, the boattail pressure drag also had an affect. In comparisons of the pressure data of figures 13, 14, and 15 at subsonic speeds, the overall pressure distribution for configuration 3 Dry indicated a lower pressure (more negative pressure coefficient). Even though the pressure acted over less rearward facing area because of the smaller boattail angle, the pressure drag was larger. At Mach 1.2, the pressure data of figures 13(e), 14(e), and 15(e) show the least negative pressure coefficients on the shroud of configuration 3 Dry. This, coupled with the fact that the smallest boattail angle presents the least rearward facing area over which the pressures act, leads to a considerable reduction in nozzle drag.

Afterburning power nozzles. The variation of nozzle drag with Mach number for the three afterburning power nozzle configurations is presented in figure 12(b). Results for these configurations were the same as those noted for the dry power nozzles. Configuration 3 A/B (largest wedge, smallest boattail angle) had the highest nozzle drag at subsonic speeds and the lowest nozzle drag at Mach = 1.2. The pressure data presented in figures 16 through 18 verify the effect of the boattail pressure drag.

The only difference between each dry power and afterburning power nozzle configuration (1 Dry to 1 A/B for example) was the thickness of the wedge and the wedge half-angle. The pressure distribution on the shroud with the jet off was very similar between the configurations. Therefore, the variation observed between the data of parts (a) and (b) of figure 12 is due to the pressure distribution over the external portion of the wedge and to differences in the rear facing cavity.

External and Internal Pressure Distributions

The pressure coefficient C_p along the exterior of the shroud and the pressure ratios $p/p_{t,j}$ along the interior of the shroud and along the wedge are shown for each of the configurations in figures 13 to 18. Since there were no obvious distinctions between the dry power and afterburning power configurations, this part of the presentation is categorized according to geometric region.

Shroud external pressure distribution. The pressure distribution on the external surface of the shroud shows the blockage effects caused by the jet plume. The local velocity on the surface decreased with increasing NPR. At subsonic speeds this jet effect was transmitted upstream over the entire nozzle boattail. (See fig. 14(c) for example.) At a Mach number of 1.2, the jet effects were far more limited and only at the higher NPR's was there any effect forward of the final two pressure taps on the shroud. (See fig. 15(e) for example.)

Shroud internal pressure distribution. In comparisons of the shroud internal pressure distribution in figures 13 to 15 or 16 to 18, it is apparent that the internal pressure on the shroud was affected only by NPR and Mach number and was not a function of either boattail angle or wedge size, as long as the throat area was held constant. The shroud internal static pressures, along with the first two upstream pressures on the wedge, show the positioning of the actual nozzle throat ($p/p_{t,j} = 0.528$) as related to the geometric nozzle throat, which was at $x/l_n = 0$. Examining these pressures shows that the actual nozzle throat was slightly skewed; that is, at a given NPR for a specific Mach number, sonic velocity was reached at a different point on the shroud than on the wedge. The amount of skew and the direction are configuration dependent. For the 1 Dry and 2 Dry configurations the flow reached sonic velocity on the shroud slightly upstream of the point at which sonic velocity was reached on the wedge, with the skew being less for configuration 2 Dry. The pressures for configuration 3 Dry show that the skew was reversed, with sonic velocity being reached on the wedge at a point upstream of where the flow was sonic on the shroud. Since the pressure distribution on the shroud was independent of the configuration for a given power setting, the throat movement is due to the change in wedge size. The three afterburning power configurations show the same effects due to wedge size change, with the exception that for configuration 3 A/B (fig. 18) the skew direction was dependent on the combination of NPR and Mach number.

Wedge surface pressure distribution. The wedge surface pressure distribution for these nozzles was typical of wedge nozzles in general. Namely, the pressure from the throat to slightly downstream of the exit was the same for all values of NPR, with flow separation then occurring on the wedge. The point at which flow separation occurred moved further downstream as NPR was increased (refs. 12 and 13), though flow separation was never eliminated for any configuration tested. The pressure data also show external expansion of the flow on the wedge, particularly at Mach 1.2.

Concluding Remarks

An investigation was conducted in the Langley 16-Foot Transonic Tunnel to determine the effect of a boattail-angle and wedge-size trade on the performance of nonaxisymmetric wedge nozzles installed on a generic twin-engine fighter aircraft model. This investigation was conducted at static conditions (a Mach number of 0) and at Mach numbers from 0.60 to 1.25 over a nozzle pressure ratio range from 1.0 (jet off) to slightly over 15.0 and at an angle of attack of 0°.

The results of this investigation indicate the following:

1. For the configurations of this investigation, wedge size can be reduced while increasing boattail angle without significantly affecting aeropropulsive performance.

2. All the configurations tested had separated flow on the wedge at all conditions, although the point at which flow separation occurred on the wedge was moved downstream by increasing the nozzle pressure ratio.

3. The point at which the flow on the wedge became sonic moved further downstream as wedge size was decreased, which caused the actual nozzle throat to be skewed.

4. The configuration with the largest wedge and smallest boattail angle had the highest drag at subsonic speeds and the lowest drag at supersonic speed for both the dry power and afterburning power nozzles.

5. Pressure distribution along the internal surface of the shroud was not affected by changing boattail angle.

NASA Langley Research Center
Hampton, VA 23665-5225
May 18, 1987

References

1. Stevens, H. L.; Thayer, E. B.; and Fullerton, J. F.: Development of the Multi-Function 2-D/C-D Nozzle. AIAA-81-1491, July 1981.
2. Yetter, Jeffery A.; and Leavitt, Laurence D.: *Effects of Sidewall Geometry on the Installed Performance of Nonaxisymmetric Convergent-Divergent Exhaust Nozzles.* NASA TP-1771, 1980.
3. Capone, Francis J.; Re, Richard J.; and Bare, E. Ann: Thrust Reversing Effects on Twin-Engine Aircraft Having Nonaxisymmetric Nozzles. AIAA-81-2639, Dec. 1981.
4. Carson, George T., Jr.; Capone, Francis J.; and Mason, Mary L.: *Aeropropulsive Characteristics of Nonaxisymmetric-Nozzle Thrust Reversers at Mach Numbers From 0 to 1.20.* NASA TP-2306, 1984.
5. Re, Richard J.; and Berrier, Bobby L.: *Static Internal Performance of Single Expansion-Ramp Nozzles With Thrust Vectoring and Reversing.* NASA TP-1962, 1982.
6. Berrier, Bobby L.; and Leavitt, Laurence D.: *Static Internal Performance of Single-Expansion-Ramp Nozzles With Thrust-Vectoring Capability up to* 60°. NASA TP-2364, 1984.
7. Mason, Mary L.; and Capone, Francis J.: *Aeropropulsive Characteristics of Twin Single-Expansion-Ramp Vectoring Nozzles Installed With Forward-Swept Wings and Canards.* NASA TP-2133, 1983.
8. Maiden, Donald L.: *Performance of an Isolated Two-Dimensional Variable-Geometry Wedge Nozzle With Translating Shroud and Collapsing Wedge at Speeds up to Mach 2.01.* NASA TN D-7906, 1975.
9. Maiden, Donald L.: *Performance of an Isolated Two-Dimensional Wedge Nozzle With Fixed Cowl and Variable Wedge Centerbody at Mach Numbers up to 2.01.* NASA TN D-8218, 1976.
10. Maiden, Donald L.; and Petit, John E.: Investigation of Two-Dimensional Wedge Exhaust Nozzles for Advanced Aircraft. *J. Aircr.*, vol. 13, no. 10, Oct. 1976, pp. 809–816.
11. Capone, Francis J.; and Maiden, Donald L.: *Performance of Twin Two-Dimensional Wedge Nozzles Including Thrust Vectoring and Reversing Effects at Speeds up to Mach 2.20.* NASA TN D-8449, 1977.
12. Carson, George T., Jr.; and Mason, Mary L.: *Experimental and Analytical Investigation of a Nonaxisymmetric Wedge Nozzle at Static Conditions.* NASA TP-1188, 1978.
13. Mason, Mary L.; and Abeyounis, William K.: *Experimental Investigation of Two Nonaxisymmetric Wedge Nozzles at Free-Stream Mach Numbers up to 1.20.* NASA TP-2054, 1982.
14. Berrier, Bobby L.; and Re, Richard J.: *Effect of Several Geometric Parameters on the Static Internal Performance of Three Nonaxisymmetric Nozzle Concepts.* NASA TP-1468, 1979.
15. Capone, Francis J.: *Static Performance of Five Twin-Engine Nonaxisymmetric Nozzles With Vectoring and Reversing Capability.* NASA TP-1224, 1978.
16. Hiley, P. E.; Wallace, H. W.; and Booz, D. E.: Nonaxisymmetric Nozzles Installed in Advanced Fighter Aircraft. *J. Aircr.*, vol. 13, no. 12, Dec. 1976, pp. 1000–1006.
17. Sedgwick, T. A.: Investigation of Non-Symmetric Two-Dimensional Nozzles Installed in Twin-Engine Tactical Aircraft. AIAA Paper No. 75-1319, Sept.–Oct. 1975.
18. Berrier, Bobby L.; Palcza, J. Lawrence; and Richey, G. Keith: Nonaxisymmetric Nozzle Technology Program—An Overview. AIAA Paper 77-1225, Aug. 1977.
19. Banks, D. W.; Quinto, P. F.; and Paulson, J. W., Jr.: Thrust-Induced Effects on Low-Speed Aerodynamics of Fighter Aircraft. AIAA-81-2612, Dec. 1981.
20. Nelson, B. D.; and Nicolai, L. M.: Application of Multi-Function Nozzles to Advanced Fighters. AIAA-81-2618, Dec. 1981.
21. Bowers, Douglas L.; and Laughrey, James A.: Application of Advanced Exhaust Nozzles for Tactical Aircraft. *ICAS Proceedings—1982*, Volume 1, B. Laschka and R. Staufenbiel, eds., Aug. 1982, pp. 132–141. (Available as ICAS-82-4.1.1.)
22. Wallace, Hoyt W.; and Bowers, Douglas L.: Advanced Nozzle Integration for Air Combat Fighter Application. AIAA-82-1135, June 1982.
23. Willard, C. M.; Capone, F. J.; Konarski, M.; and Stevens, H. L.: Static Performance of Vectoring/Reversing Non-Axisymmetric Nozzles. AIAA Paper 77-840, July 1977.
24. Stevens, H. L.: *F-15/Nonaxisymmetric Nozzle System Integration Study Support Program.* NASA CR-135252, 1978.
25. Capone, Francis J.: The Nonaxisymmetric Nozzle—It is for Real. AIAA Paper 79-1810, Aug. 1979.

26. Peddrew, Kathryn H., compiler: *A User's Guide to the Langley 16-Foot Transonic Tunnel.* NASA TM-83186, 1981.
27. Berrier, Bobby L.; Leavitt, Laurence D.; and Bangert, Linda S.: *Operating Characteristics of the Multiple Critical Venturi System and Secondary Calibration Nozzles Used for Weight-Flow Measurements in the Langley 16-Foot Transonic Tunnel.* NASA TM-86405, 1985.
28. Stratford, B. S.: The Calculation of the Discharge Coefficient of Profiled Choked Nozzles and the Optimum Profile for Absolute Air Flow Measurement. *J. Royal Aeronaut. Soc.*, vol. 68, no. 640, Apr. 1964, pp. 237–245.
29. Mercer, Charles E.; Berrier, Bobby L.; Capone, Francis J.; Grayston, Alan M.; and Sherman, C. D.: *Computations for the 16-Foot Transonic Tunnel—NASA, Langley Research Center.* NASA TM-86319, 1984.
30. Braslow, Albert L.; Hicks, Raymond M.; and Harris, Roy V., Jr.: *Use of Grit-Type Boundary-Layer-Transition Trips on Wind-Tunnel Models.* NASA TN D-3579, 1966.

Table 1. Nozzle Design Parameters

Configuration	Power setting	Boattail angle, deg	Wedge size		Wedge half-angle, deg
			l_n, cm	h_w, cm	
1 Dry	Dry	12	10.92	2.41	13
2 Dry	Dry	10	13.46	2.94	13
3 Dry	Dry	7	14.99	3.38	13
1 A/B	Afterburning	12	10.92	1.36	7
2 A/B	Afterburning	10	13.46	1.89	8
3 A/B	Afterburning	7	14.99	2.32	9

Configuration	Power setting	Internal values of—			
		A_t, cm^2	A_e/A_t	AR	Design NPR
1 Dry	Dry	20.61	1.15	5.80	3.47
2 Dry	Dry	20.61	1.15	5.80	3.47
3 Dry	Dry	20.61	1.15	5.80	3.47
1 A/B	Afterburning	43.55	1.05	2.74	2.63
2 A/B	Afterburning	43.55	1.05	2.74	2.63
3 A/B	Afterburning	43.55	1.05	2.74	2.63

Table 2. Nozzle Pressure Orifice Locations

[See fig. 7 for orientation]

Shroud exterior $(y/(b_n/2) = 0.500)$

FS, cm	x/l_n for configurations—		
	1 Dry and 1 A/B	2 Dry and 2 A/B	3 Dry and 3 A/B
150.26	−1.315	−1.067	−0.958
152.26	−1.132	−.918	−.825
154.26	−.943	−.769	−.691
156.26	−.765	−.621	−.558
158.01	−.605	−.491	−.441
159.51	−.468	−.379	−.341
160.76	−.353	−.287	−.257
161.26	−.307	−.249	−.224
162.26	−.216	−.175	−.157
162.76	−.170	−.138	−.124
165.25	.058	.047	.042

Shroud interior $(y/(b_n/2) = 0.500)$

FS, cm	x/l_n for configurations—		
	1 Dry and 1 A/B	2 Dry and 2 A/B	3 Dry and 3 A/B
156.36	−0.756	−0.613	−0.551
160.26	−.399	−.324	−.275
161.76	−.262	−.212	−.138
164.22	0	0	0

Wedge $(y/(b_n/2) = 0.500)$

FS, cm	x/l_n for configurations—		
	1 Dry and 1 A/B	2 Dry and 2 A/B	3 Dry and 3 A/B
156.36	−0.756	−0.613	−0.551
160.49	−.378	−.307	−.275
162.55	−.189	−.153	−.138
164.62	0	0	0
165.76	.105	.085	.076
169.19	.419	.340	.305
172.81	.750		
174.71		.750	
175.01	.951		
175.56		.962	
175.86			.767
179.25			.976

Table 3. Index to Data Figures

Configuration	Figure for—		
	Thrust data	Nozzle drag data	Pressure data
1 Dry	8, 9	12(a)	13
2 Dry	8, 9	12(a)	14
3 Dry	8, 9	12(a)	15
1 A/B	10, 11	12(b)	16
2 A/B	10, 11	12(b)	17
3 A/B	10, 11	12(b)	18

L-84-11,824

Figure 1. Generic twin-engine fighter aircraft wing-body model with nonaxisymmetric wedge nozzle configuration 1 Dry.

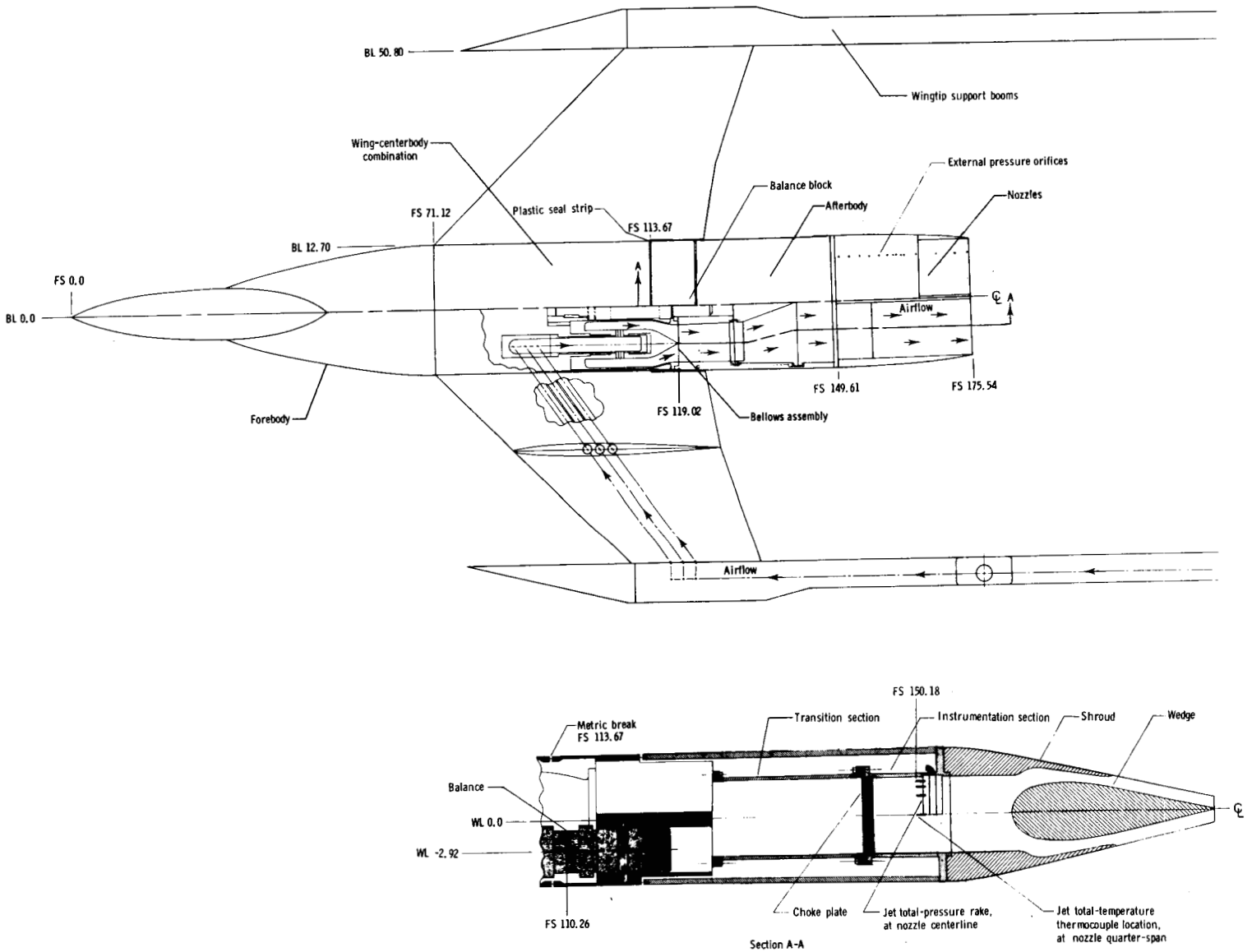

Figure 2. Model with nonaxisymmetric nozzle configuration 1 Dry showing wingtip support booms and jet simulation system. All dimensions are in centimeters.

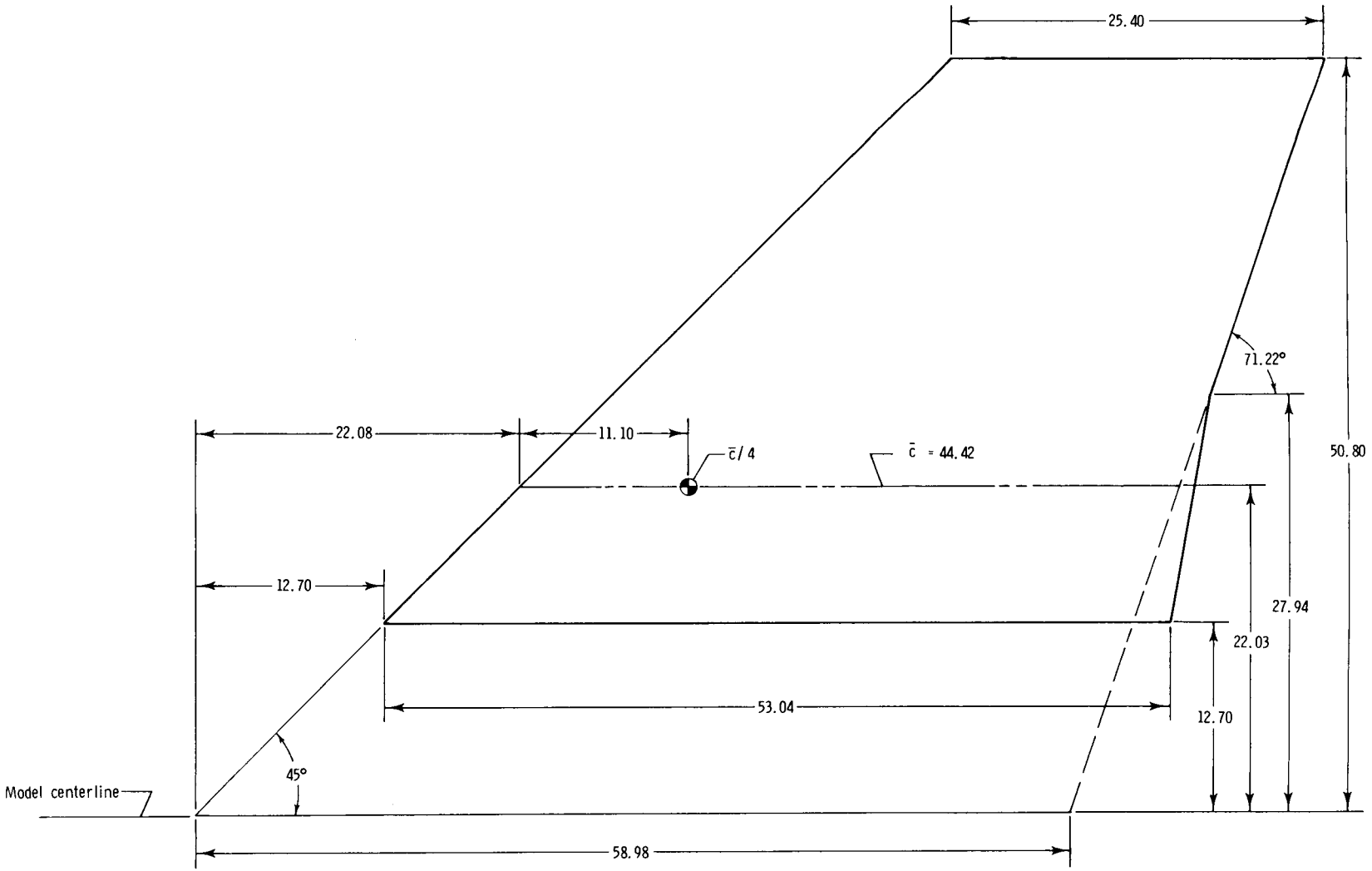

Figure 3. Wing half-span planform geometry. All linear dimensions are in centimeters.

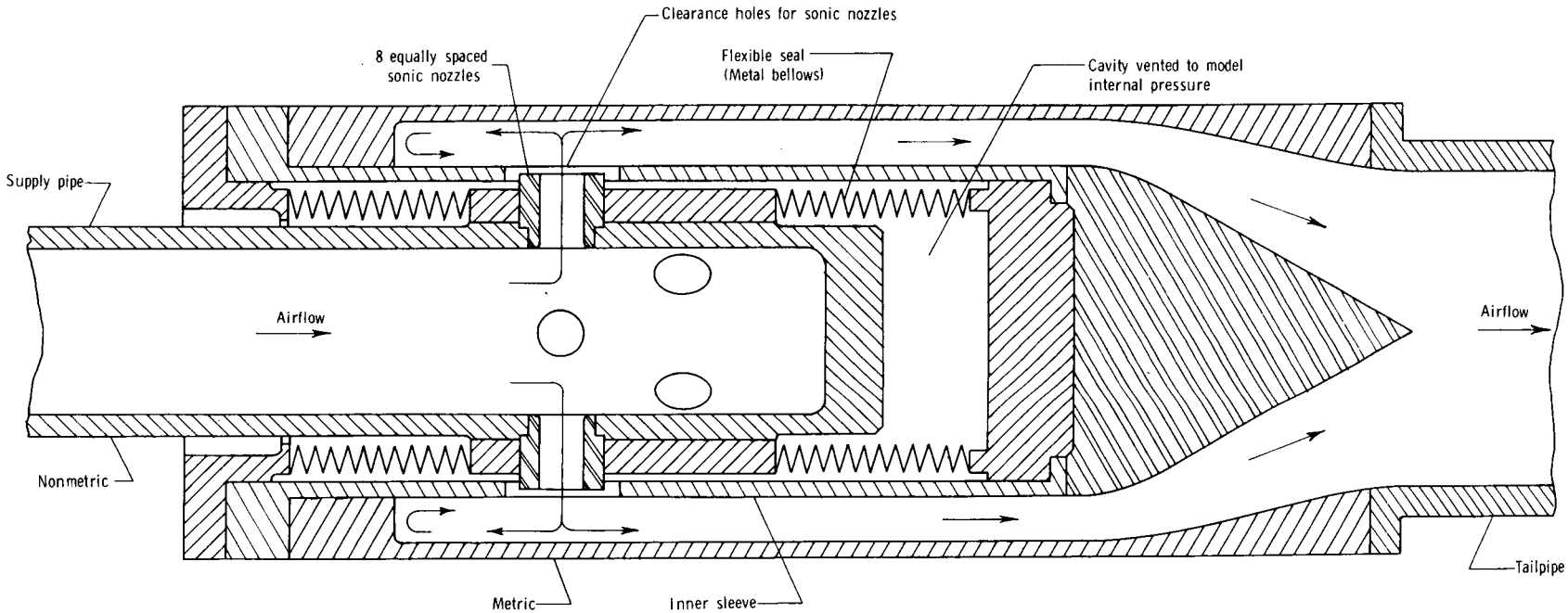

Figure 4. Details of bellows assemblies used to transfer air from nonmetric to metric portion of the model.

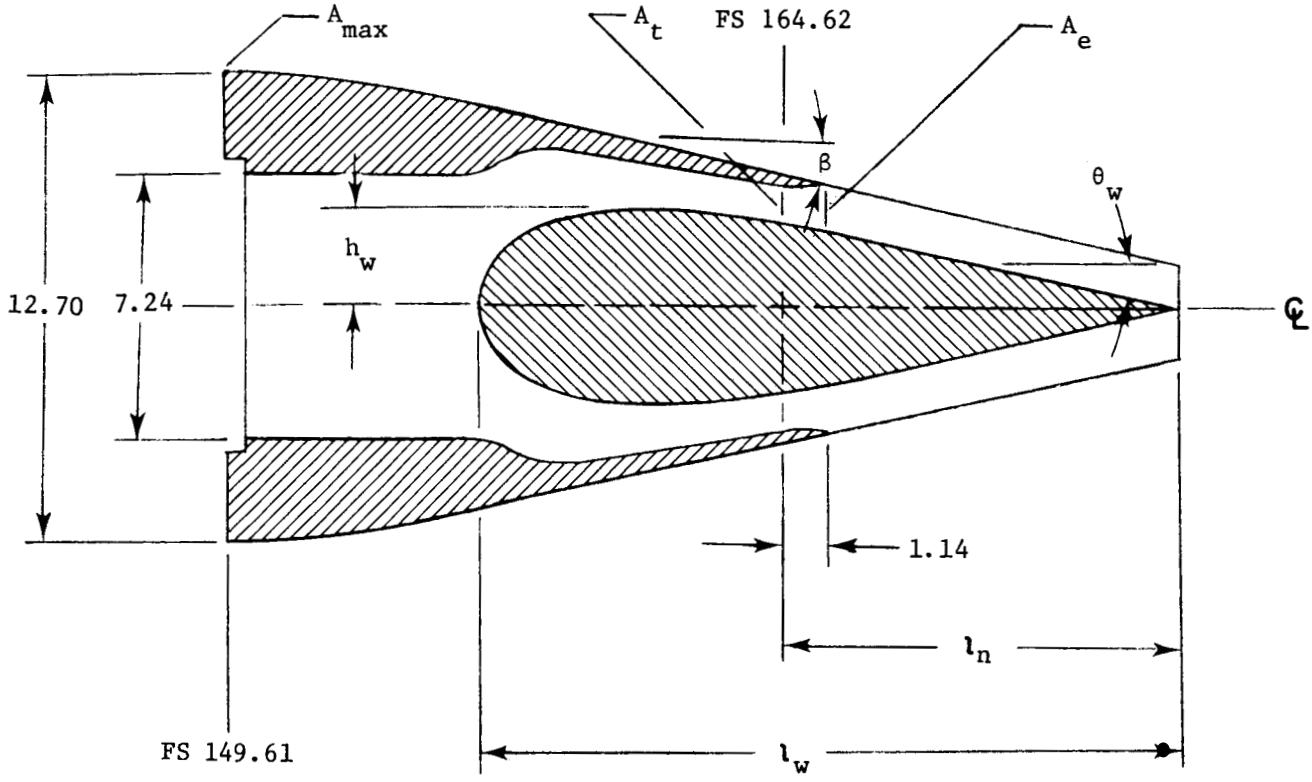

Configuration	β, deg	l_w, cm	l_n, cm	h_w, cm	θ_w, deg
1 Dry	12	19.18	10.92	2.41	13
2 Dry	10	21.72	13.46	2.94	13
3 Dry	7	23.24	14.99	3.38	13

(a) Nozzles with dry power settings. $A_{t_D} = 20.58$ cm^2, $A_{e_D}/A_{t_D} = 1.15$, and AR = 5.80.

Figure 5. Geometric details of nozzle configurations. Nozzle span b_n is 10.92 cm. All linear dimensions are in centimeters.

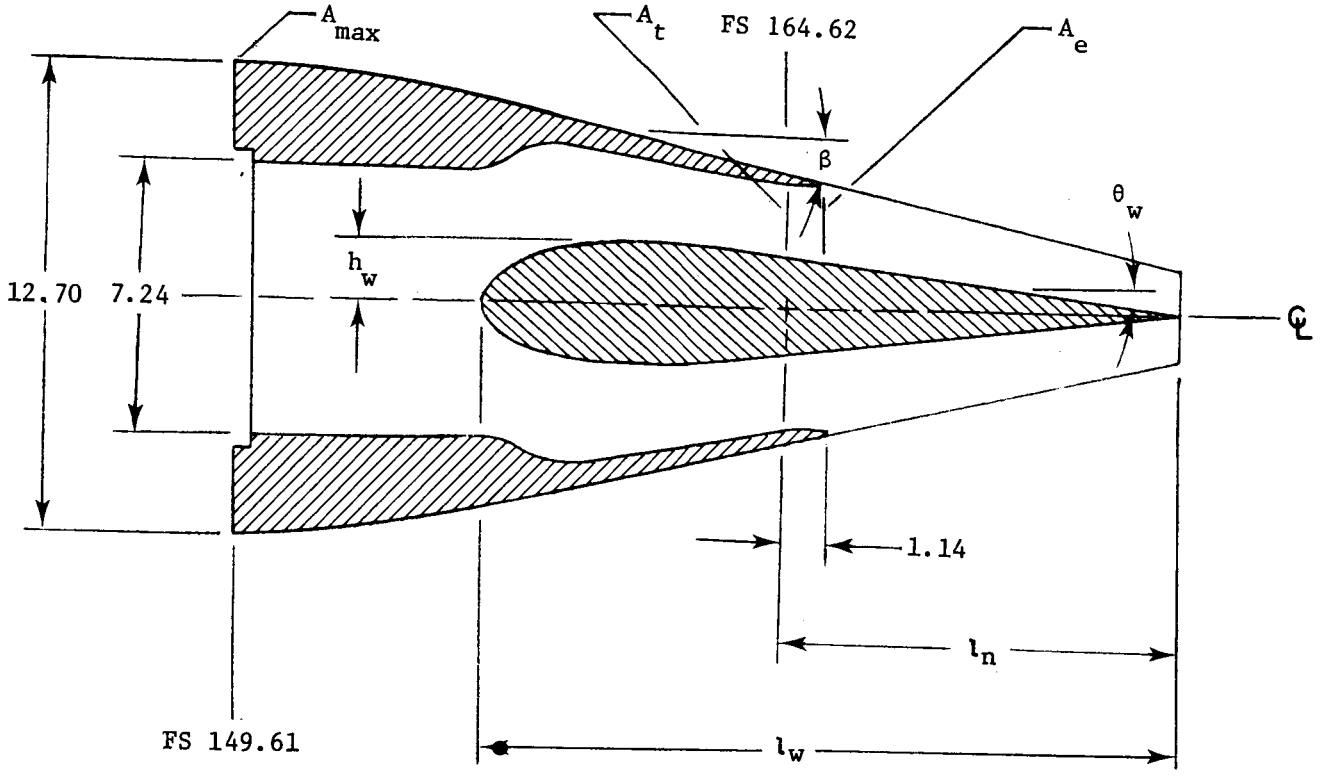

Configuration	β, deg	l_w, cm	l_n, cm	h_w, cm	θ_w, deg
1 A/B	12	19.18	10.92	1.36	7
2 A/B	10	21.72	13.46	1.89	8
3 A/B	7	23.24	14.99	2.32	9

(b) Nozzles with afterburning power settings. $A_{t_{A/B}} = 43.56$ cm^2, $A_{e_{A/B}}/A_{t_{A/B}} = 1.05$, AR = 2.74.

Figure 5. Concluded.

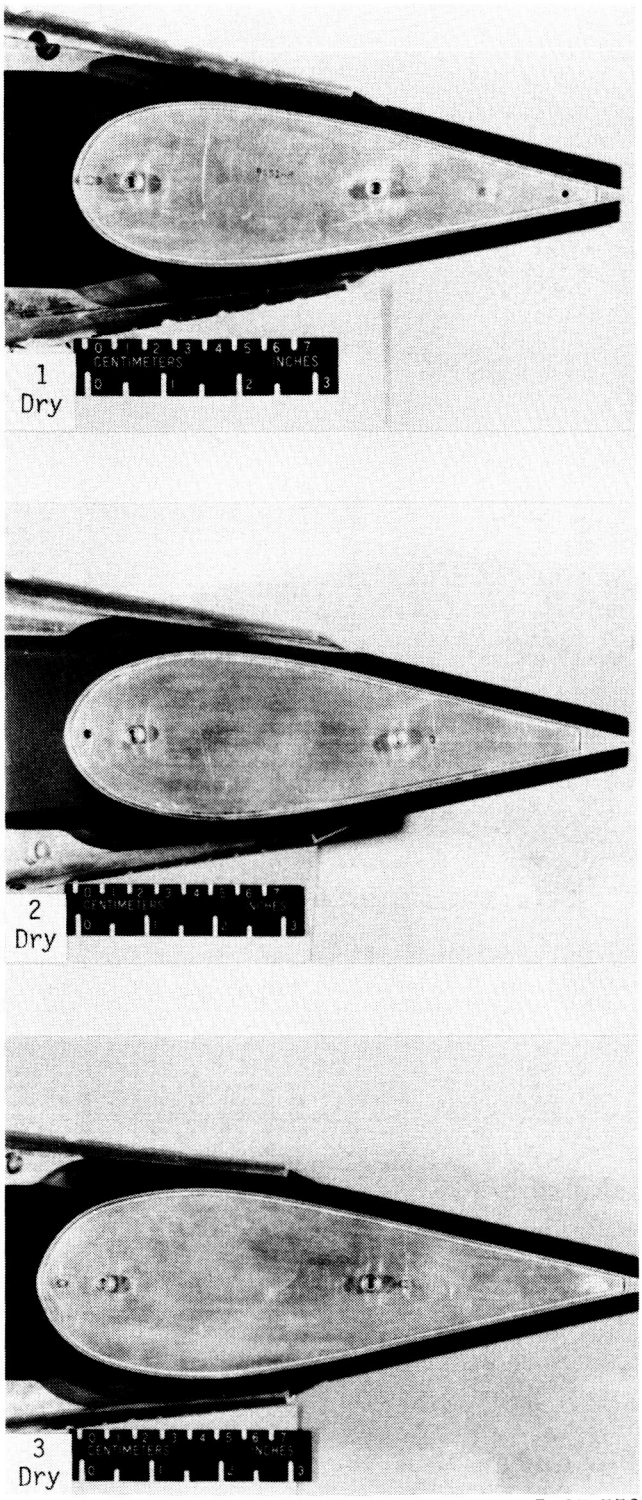

L-87-558

(a) Nozzles with dry power setting.

Figure 6. Nonaxisymmetric wedge nozzles with left sidewall removed.

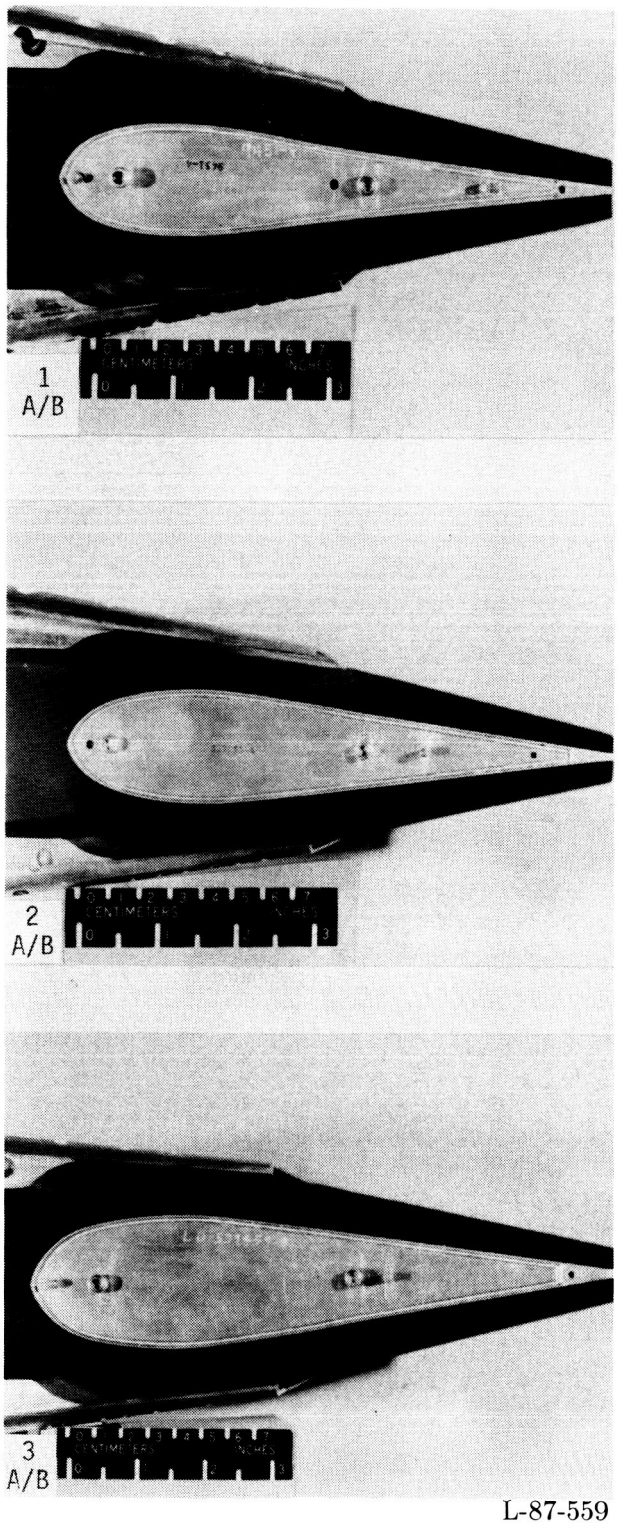

L-87-559

(b) Nozzles with afterburning power setting.

Figure 6. Concluded.

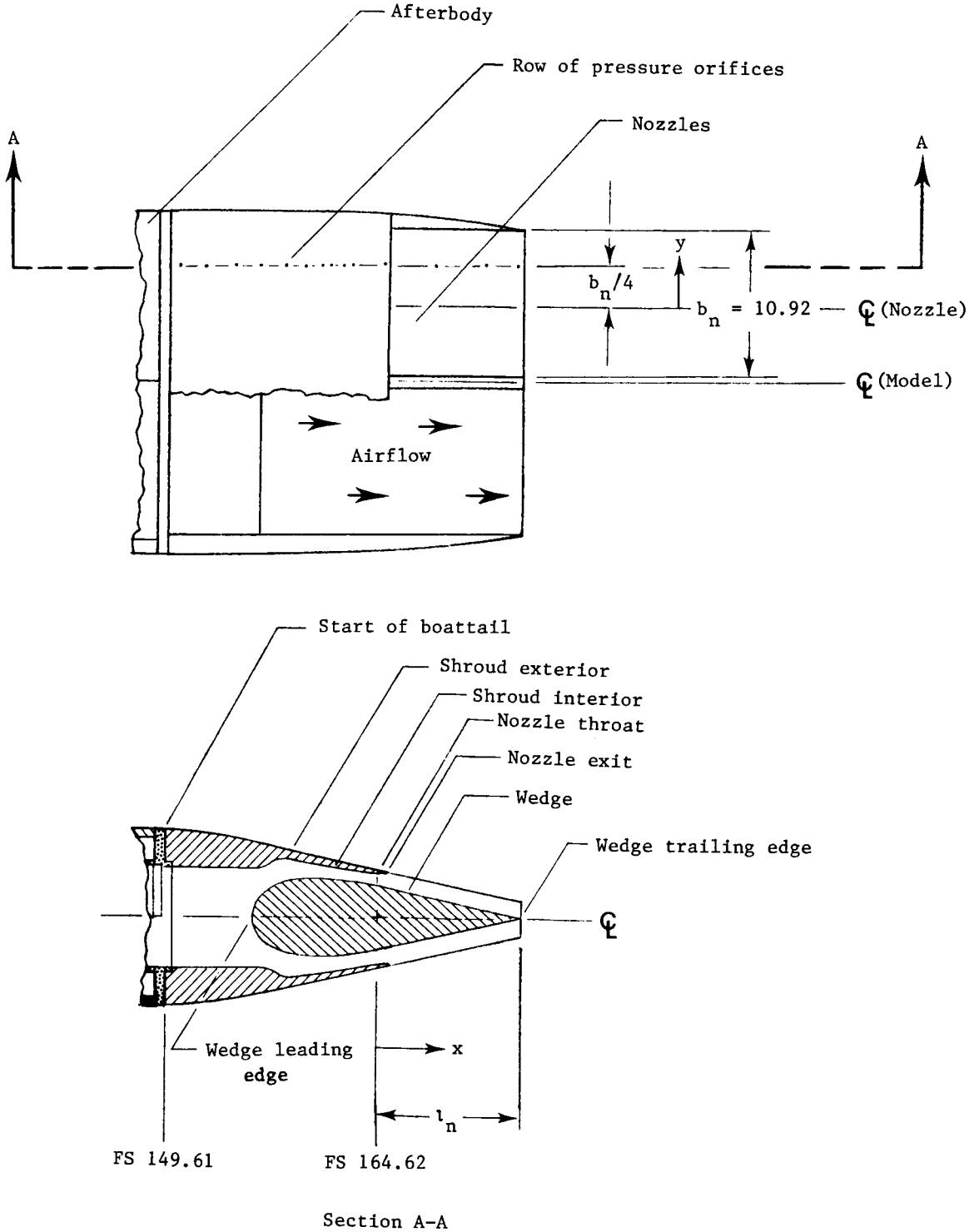

Figure 7. Orientation of nozzle pressure orifices. All dimensions are in centimeters.

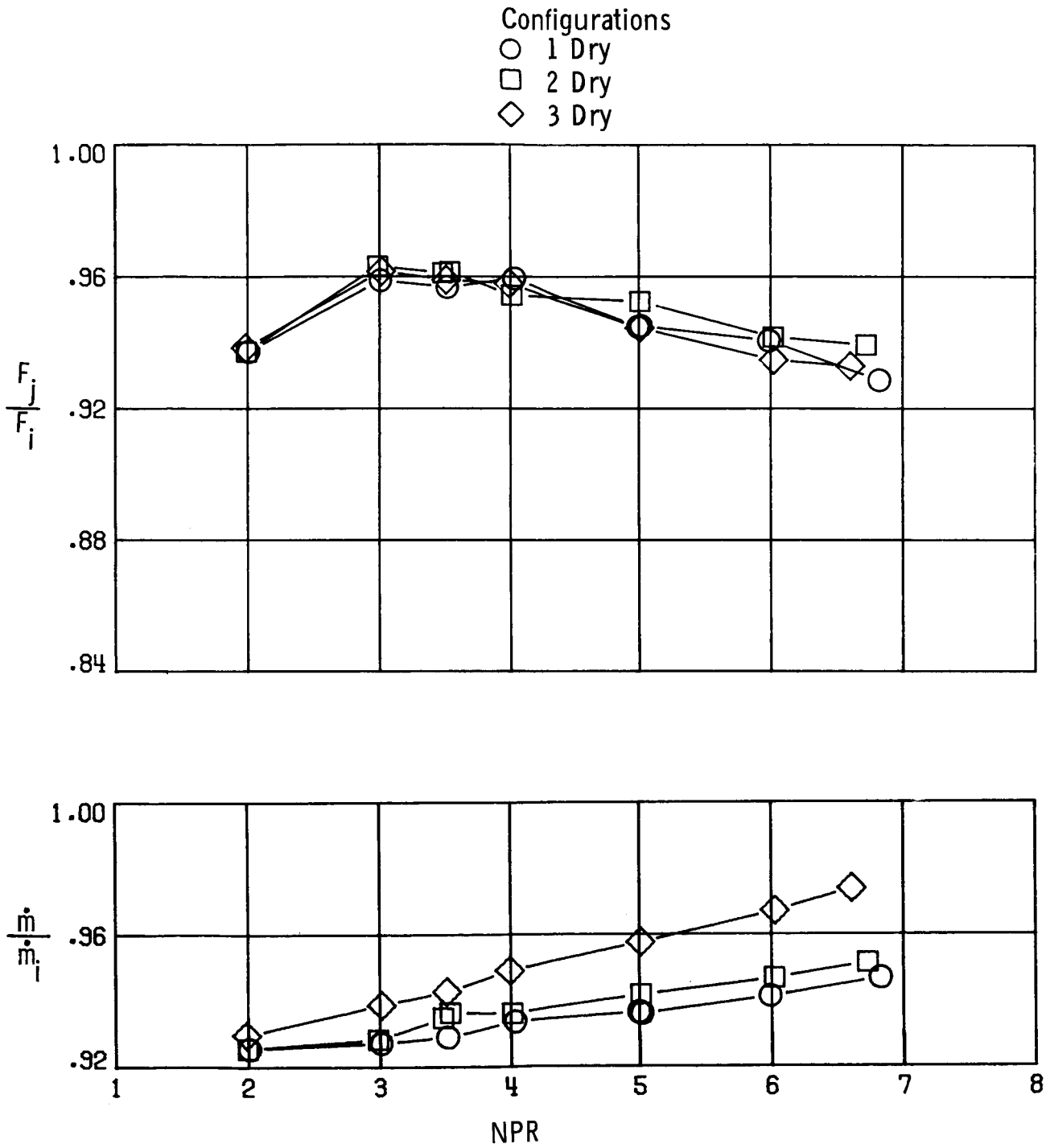

Figure 8. Static performance and discharge coefficient of dry power nozzles.

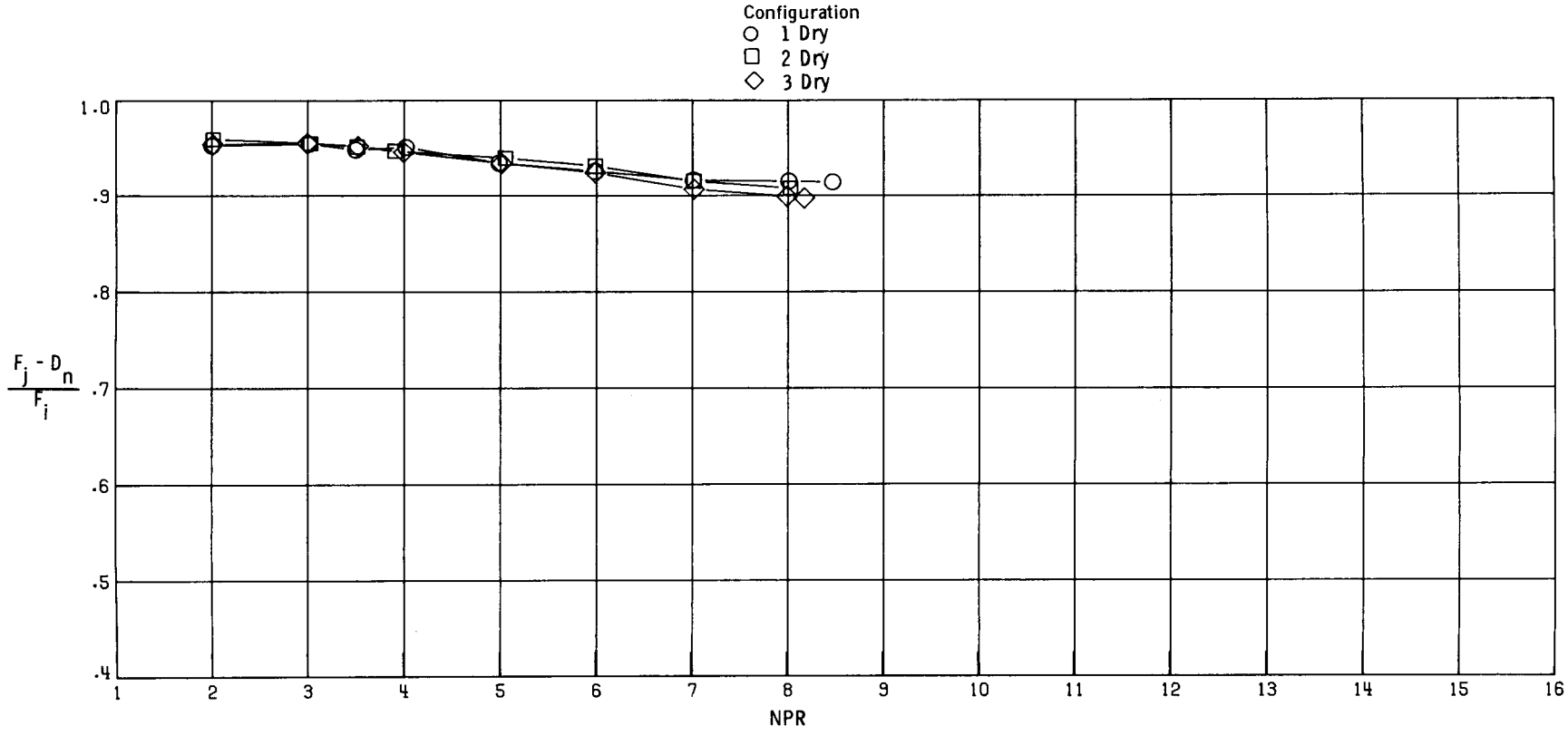

(a) $M = 0.60$.

Figure 9. Aeropropulsive performance of dry power nozzles.

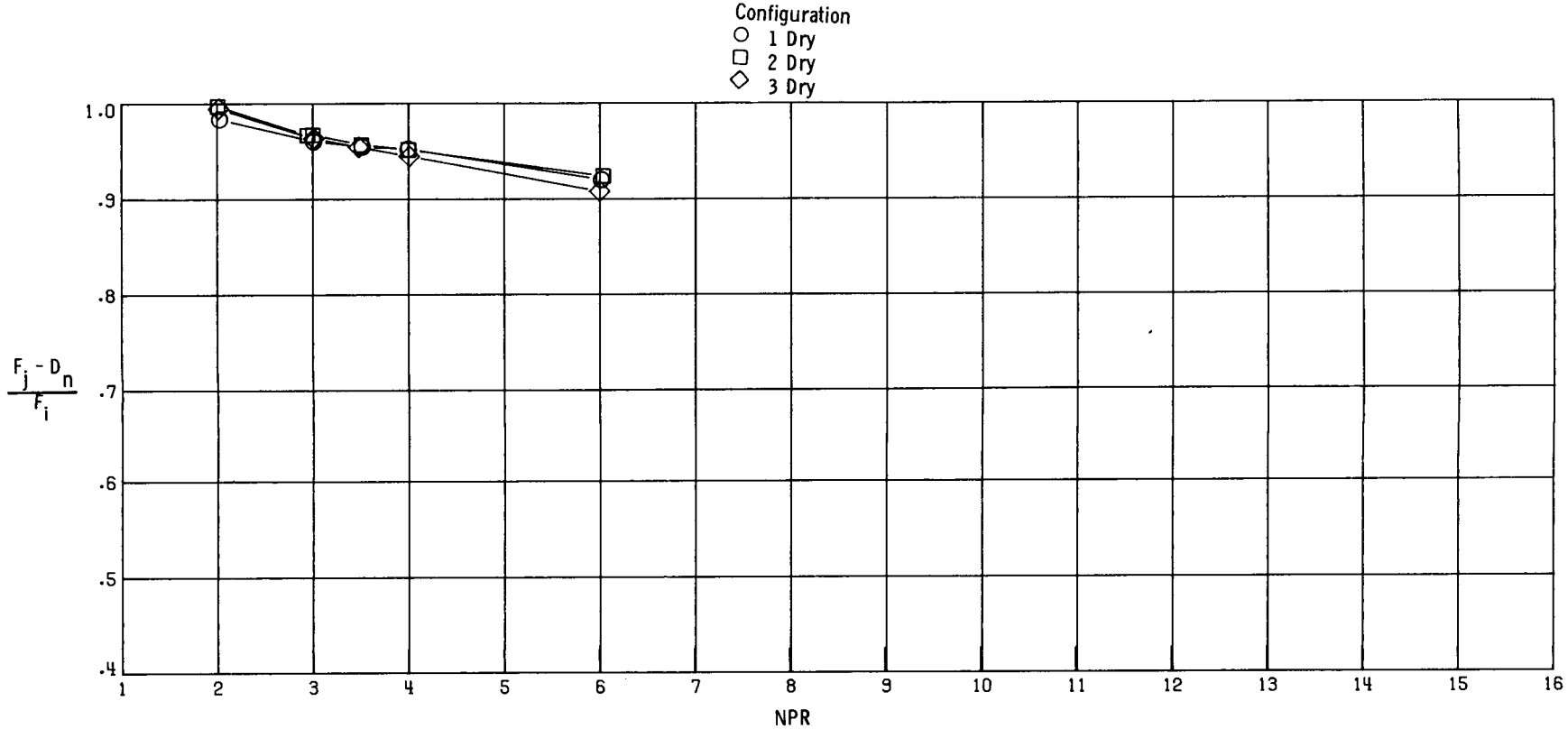

(b) $M = 0.80$.

Figure 9. Continued.

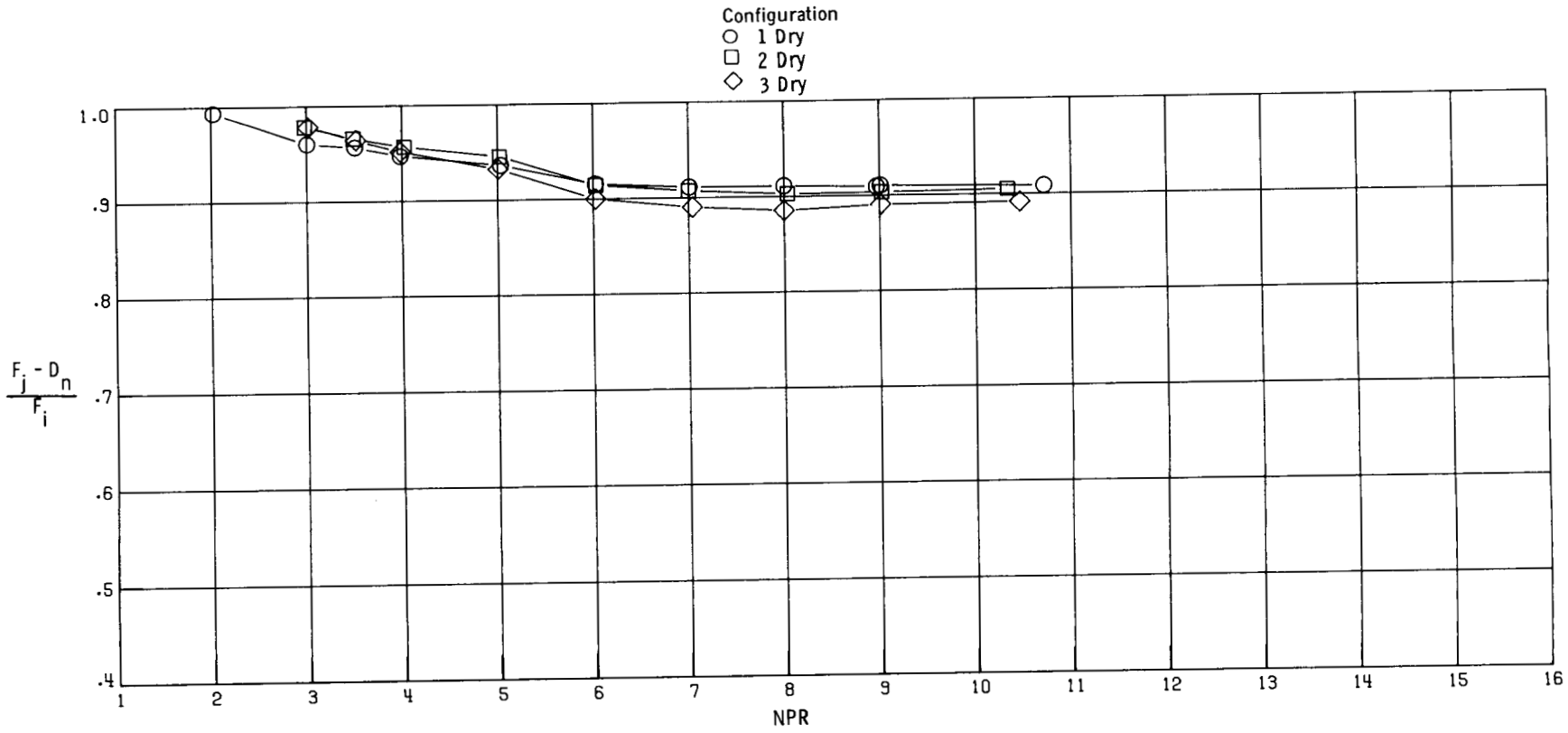

(c) $M = 0.90$.

Figure 9. Continued.

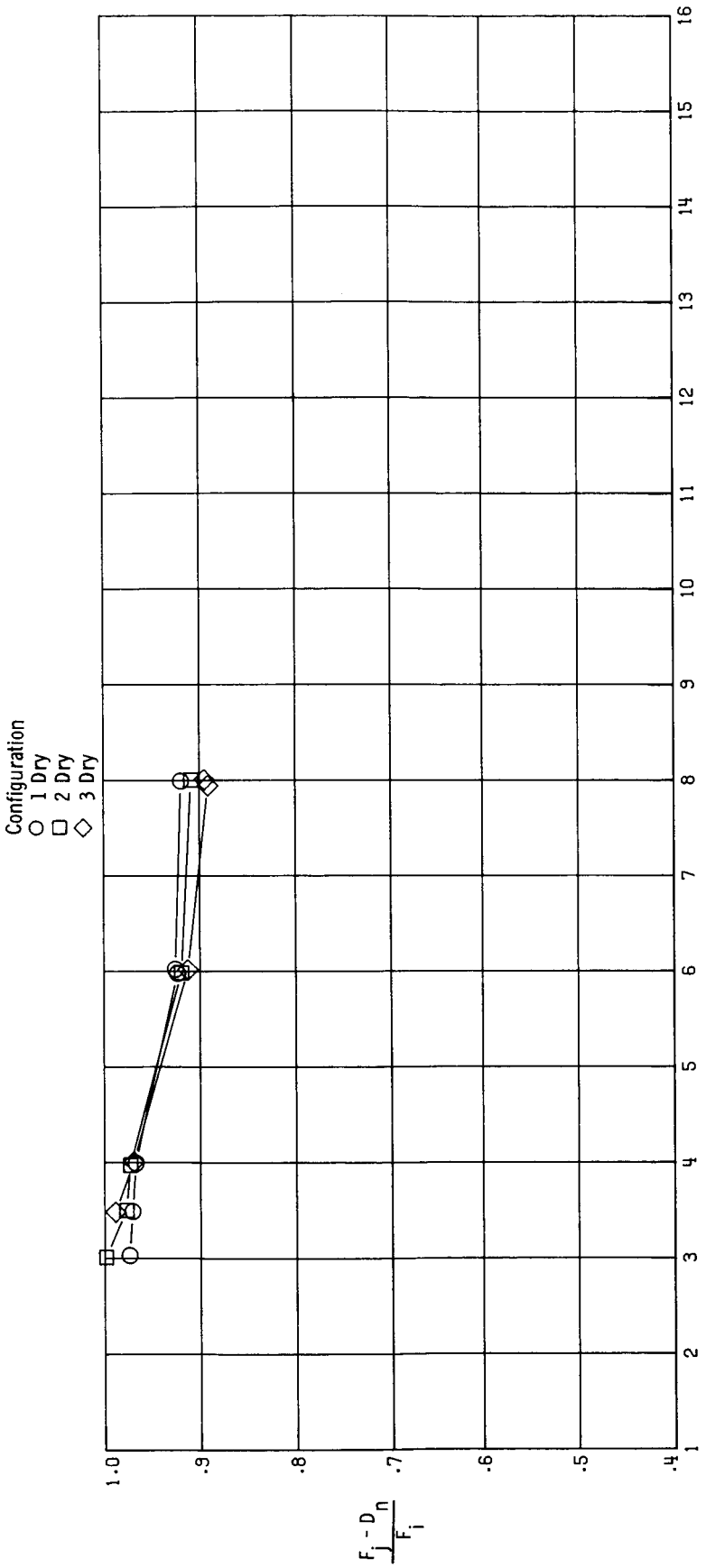

(d) $M = 0.94$.

Figure 9. Continued.

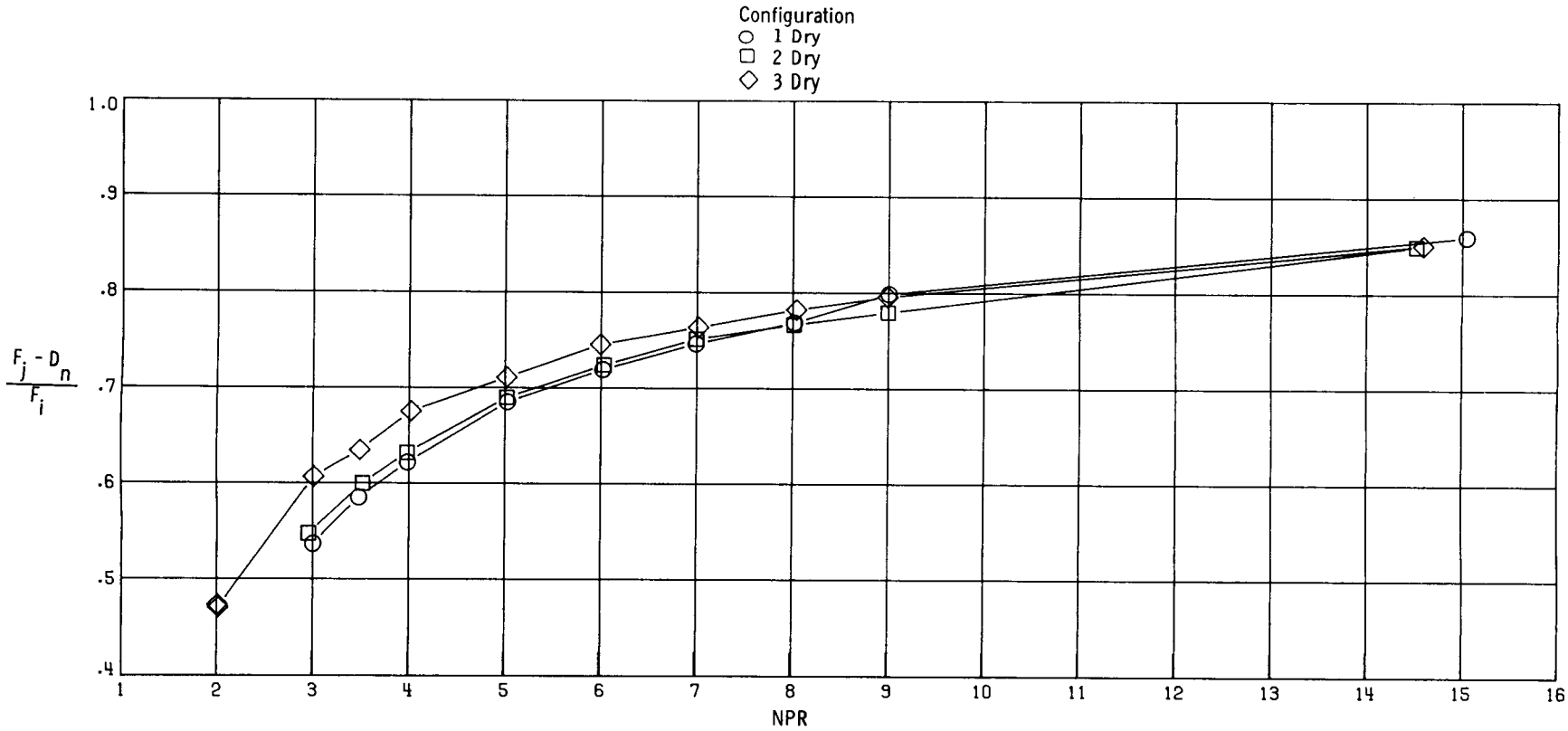

(e) $M = 1.20$.

Figure 9. Concluded.

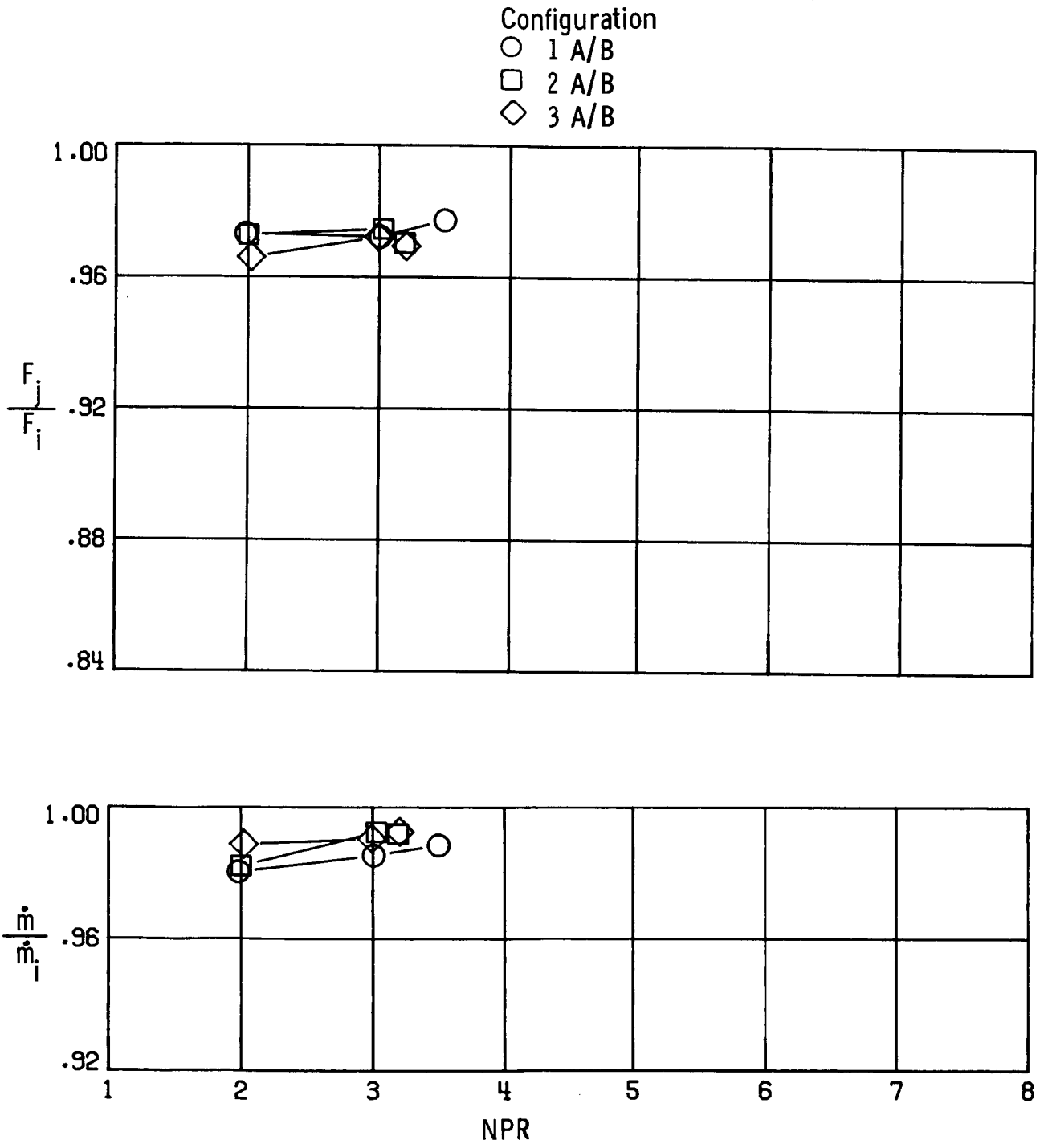

Figure 10. Static performance and discharge coefficient of afterburning power nozzles.

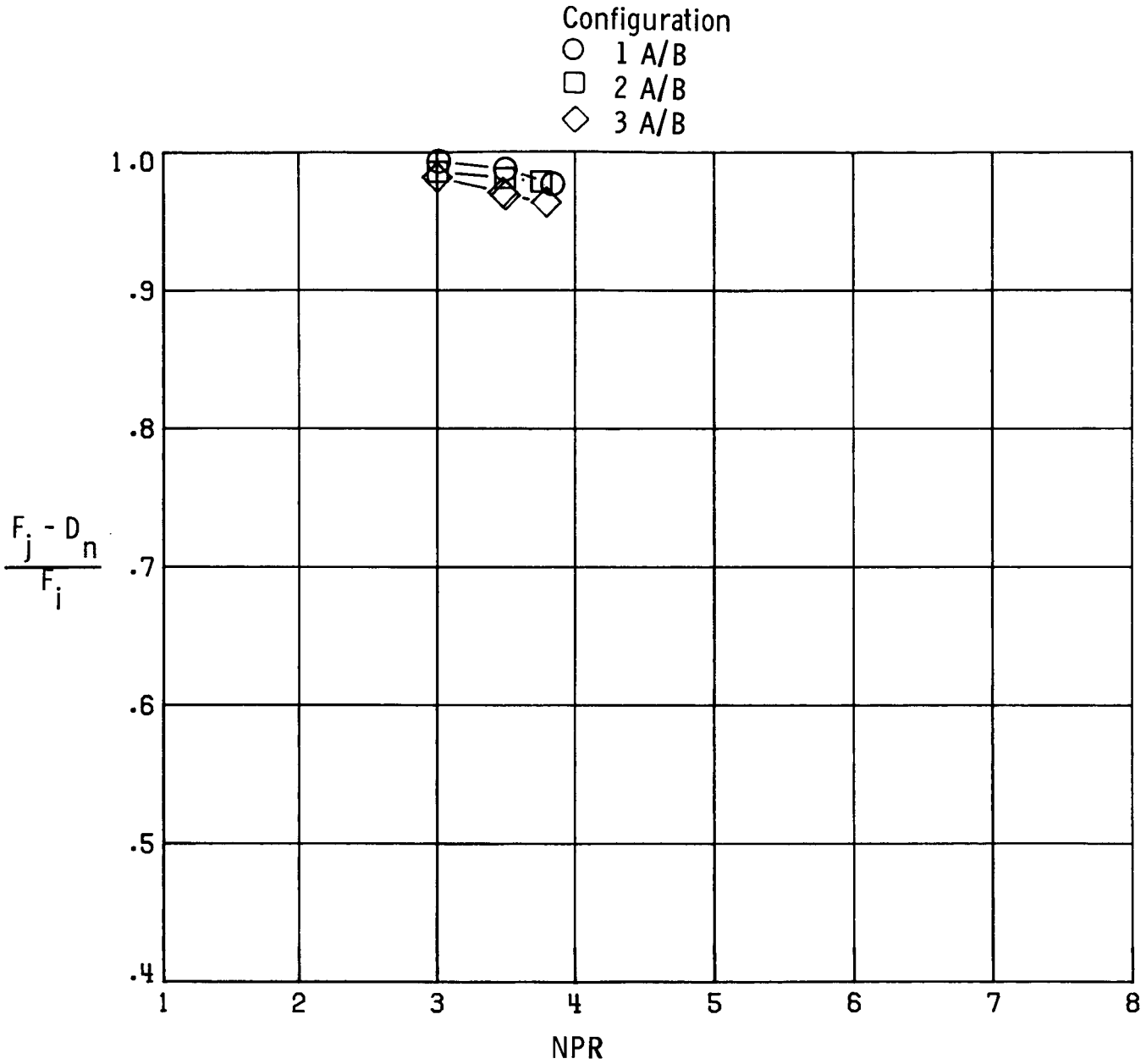

(a) $M = 0.60$.

Figure 11. Aeropropulsive performance of afterburning power nozzles.

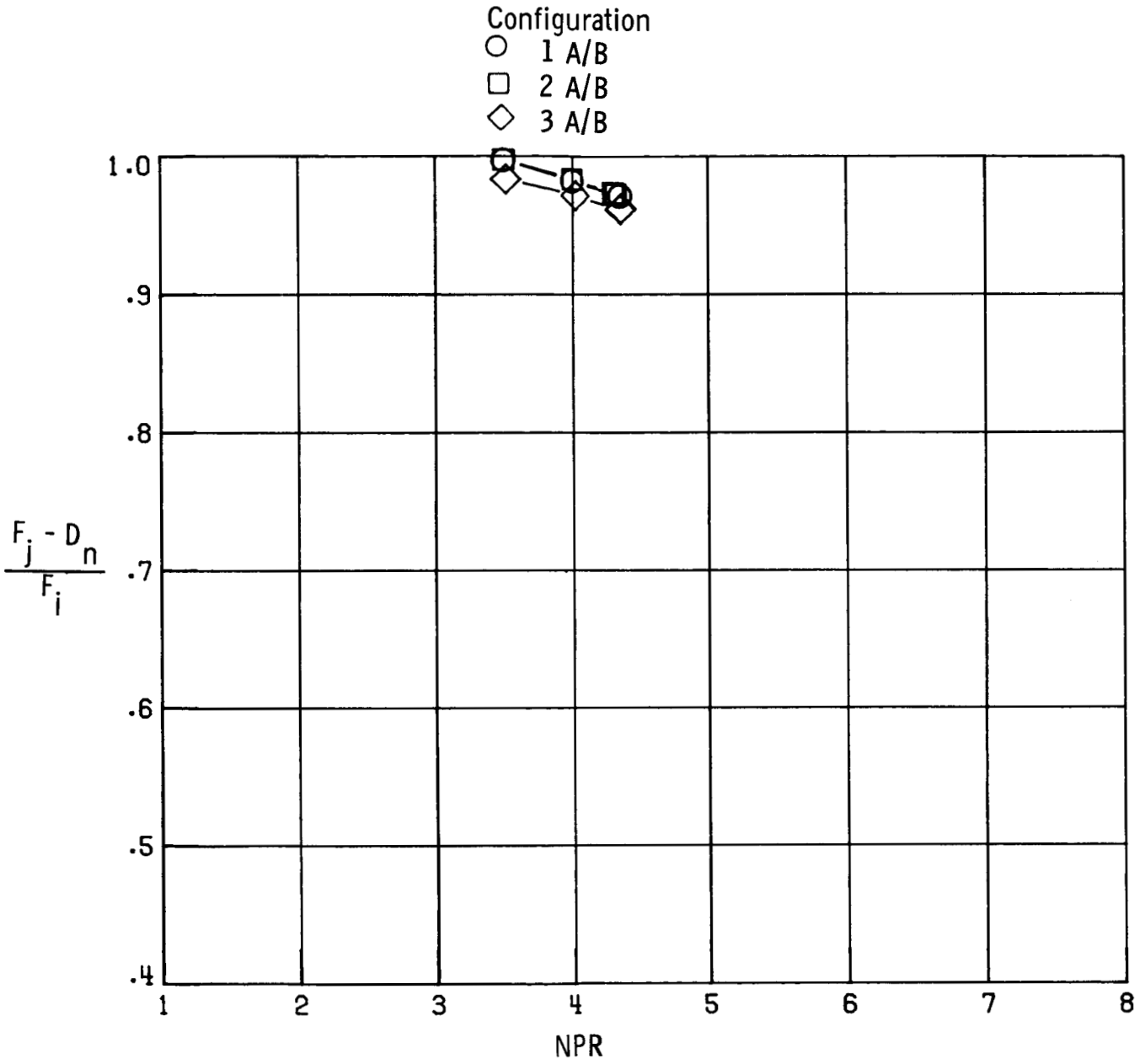

(b) $\dot{M} = 0.80$.

Figure 11. Continued.

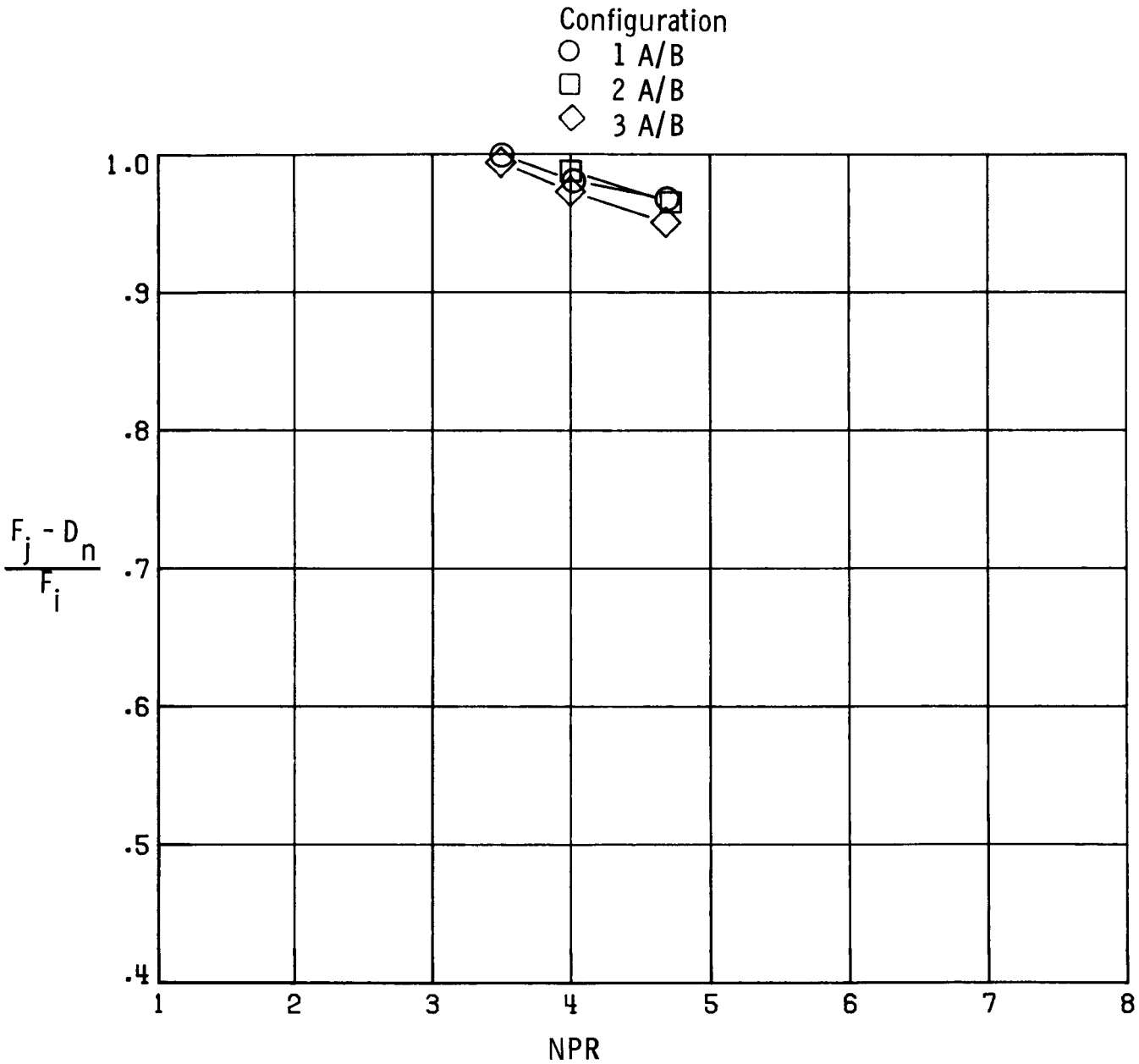

(c) $M = 0.90$.

Figure 11. Continued.

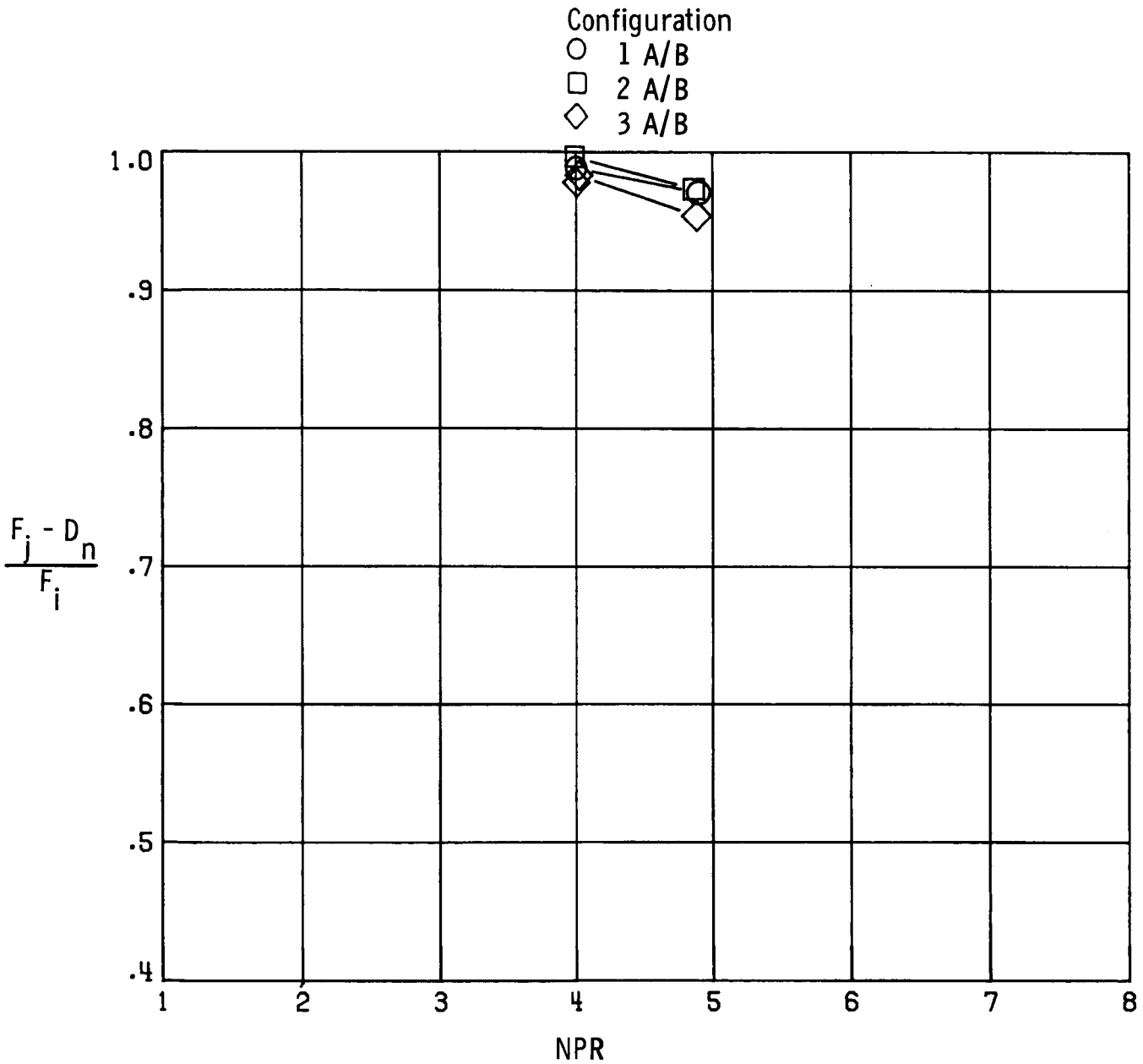

(d) $M = 0.94$.

Figure 11. Continued.

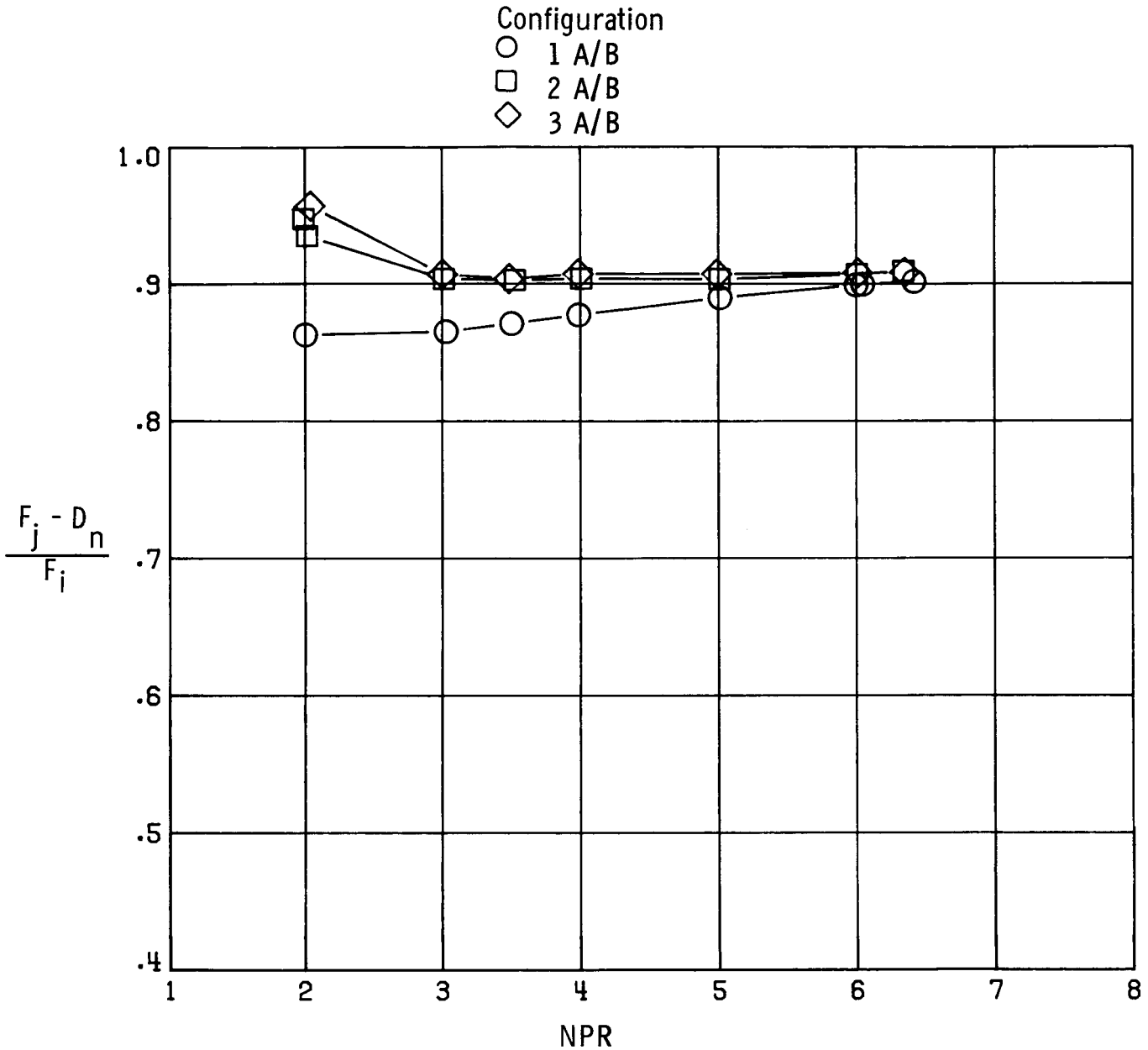

(e) $M = 1.20$.

Figure 11. Concluded.

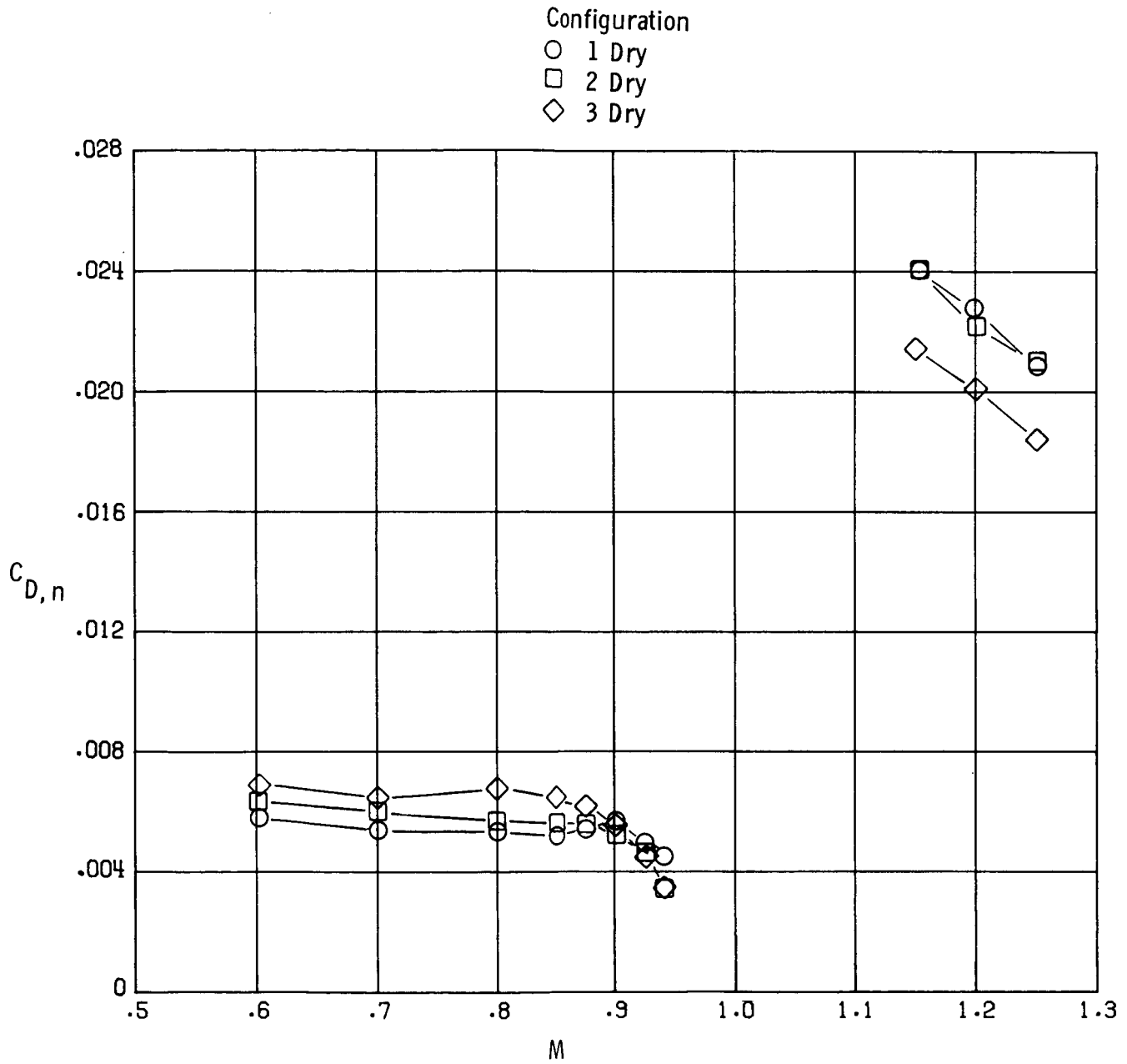

(a) Nozzles with dry power settings.

Figure 12. Variation of nozzle drag coefficient with free-stream Mach number at jet-off conditions for nonaxisymmetric wedge nozzles.

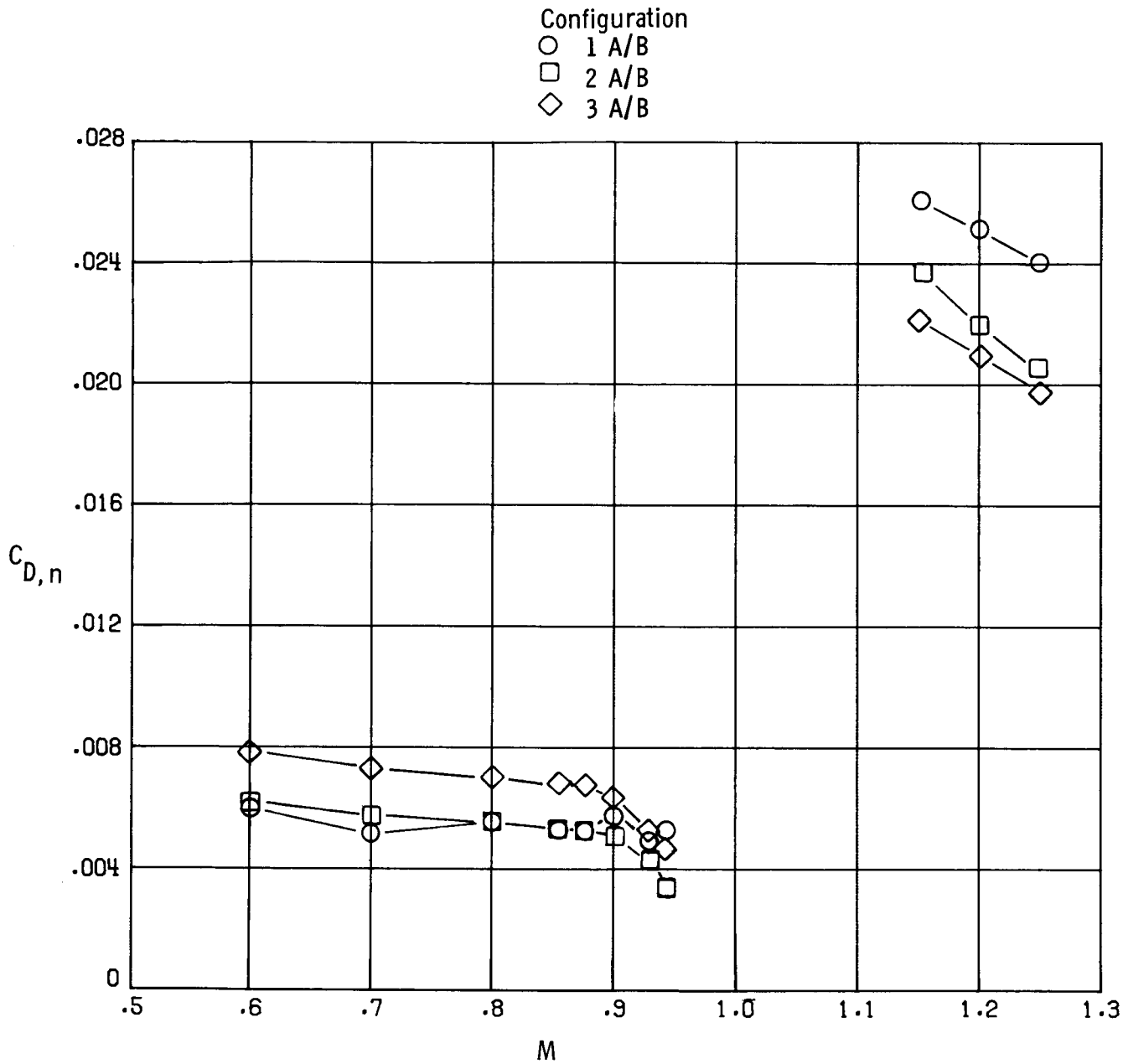

(b) Nozzles with afterburning power settings.

Figure 12. Concluded.

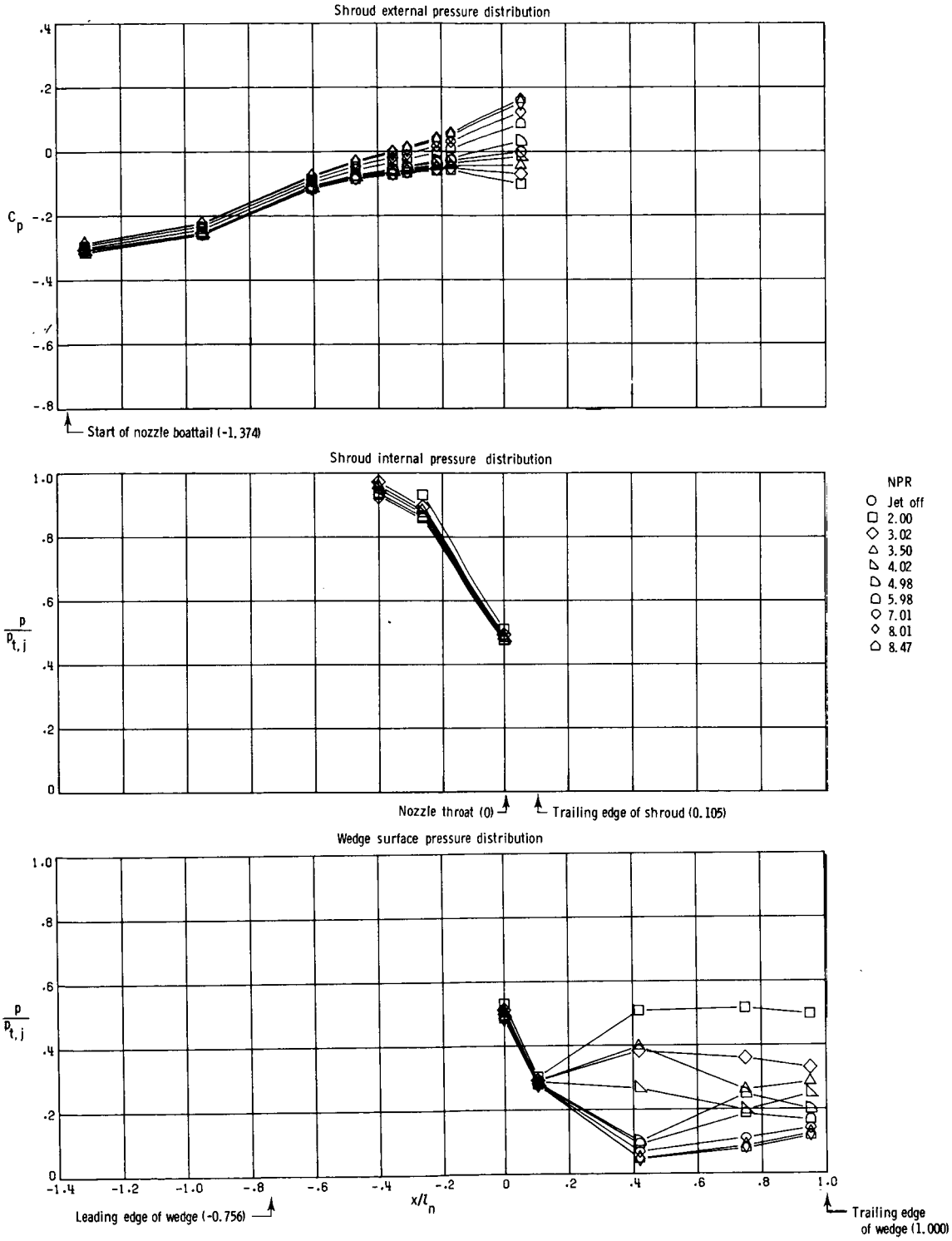

(a) $M = 0.60$.

Figure 13. External and internal surface pressure distributions $(y/(b_n/2) = 0.500)$ of configuration 1 Dry.

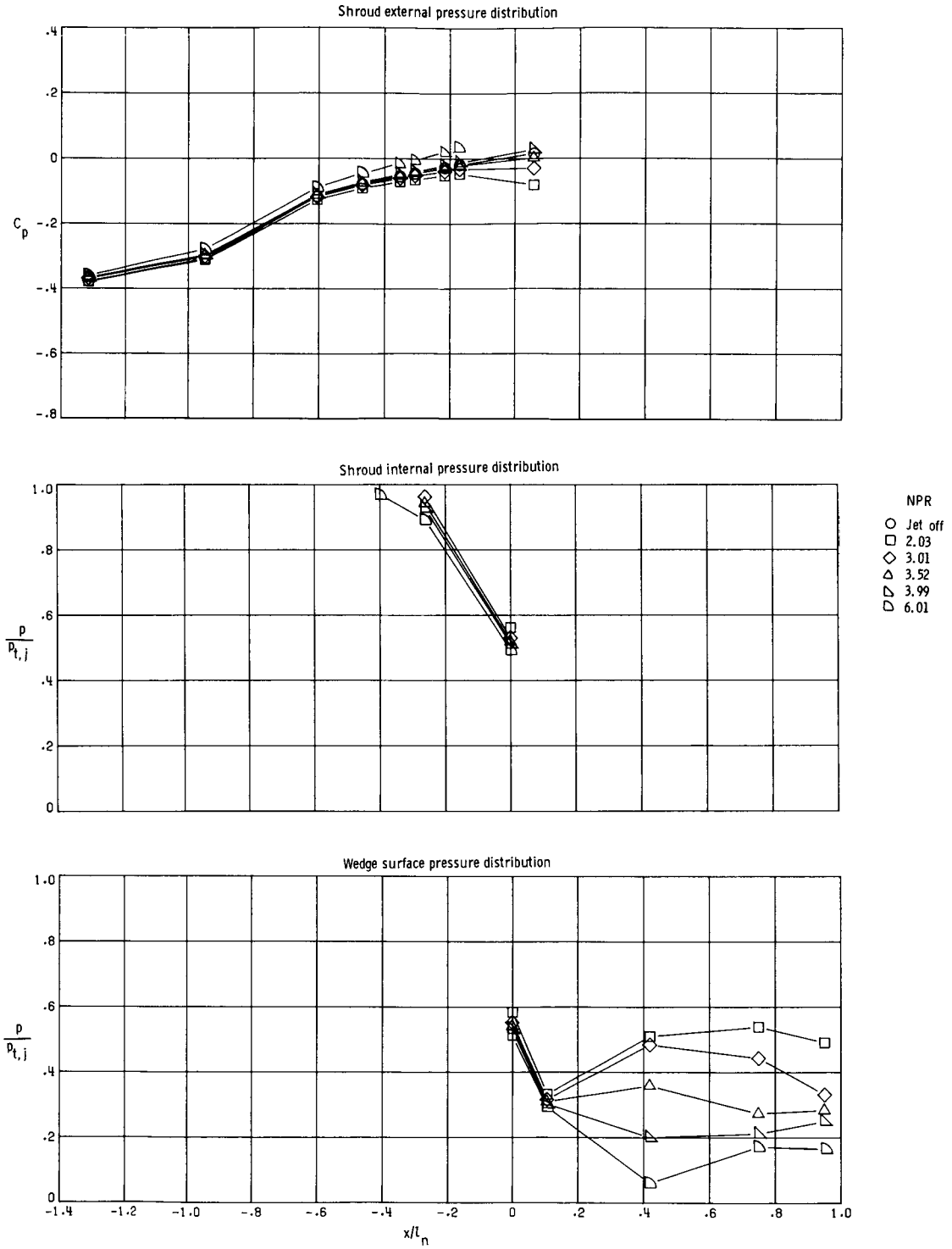

(b) $M = 0.80$.

Figure 13. Continued.

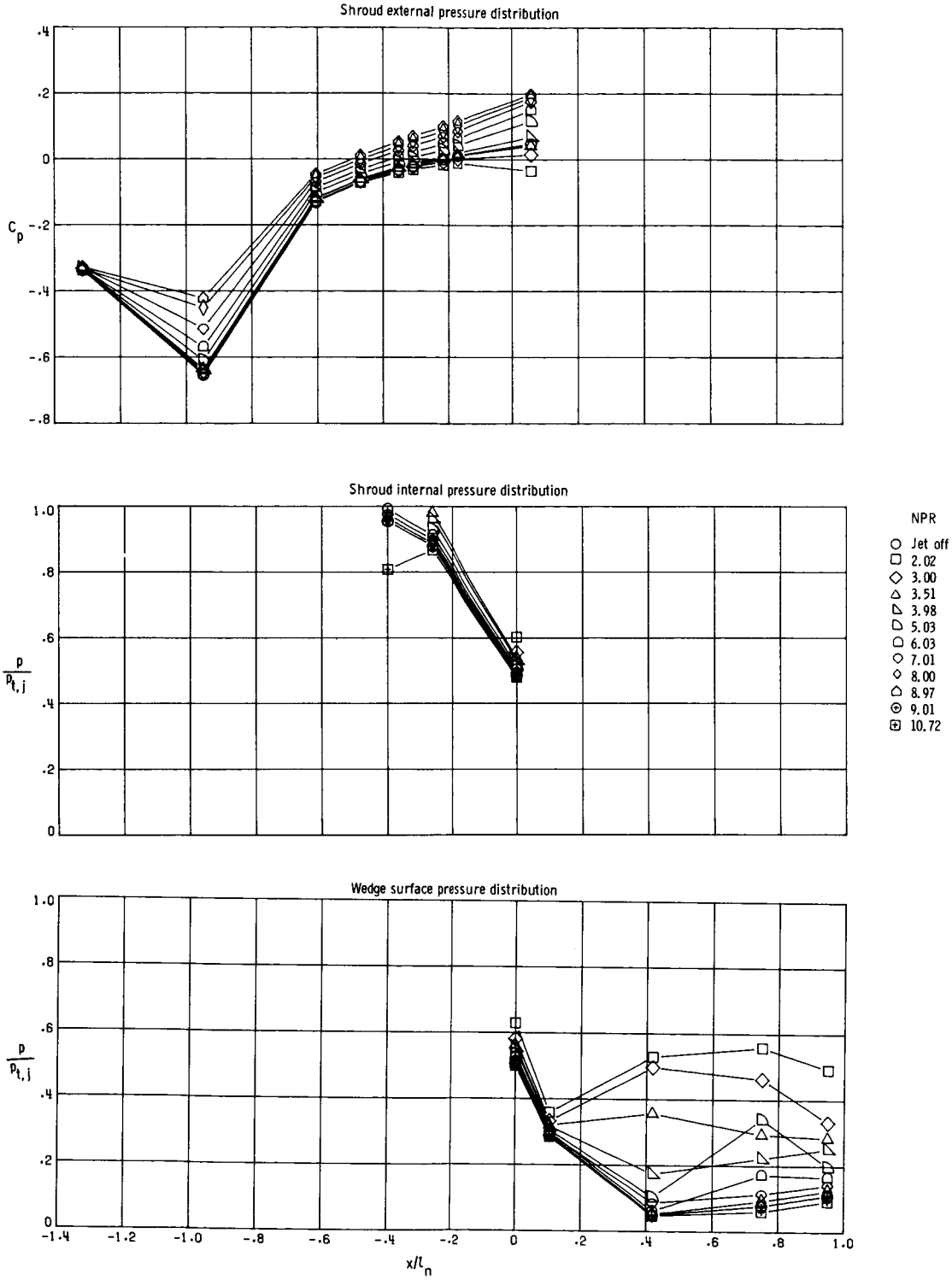

(c) $M = 0.90$.

Figure 13. Continued.

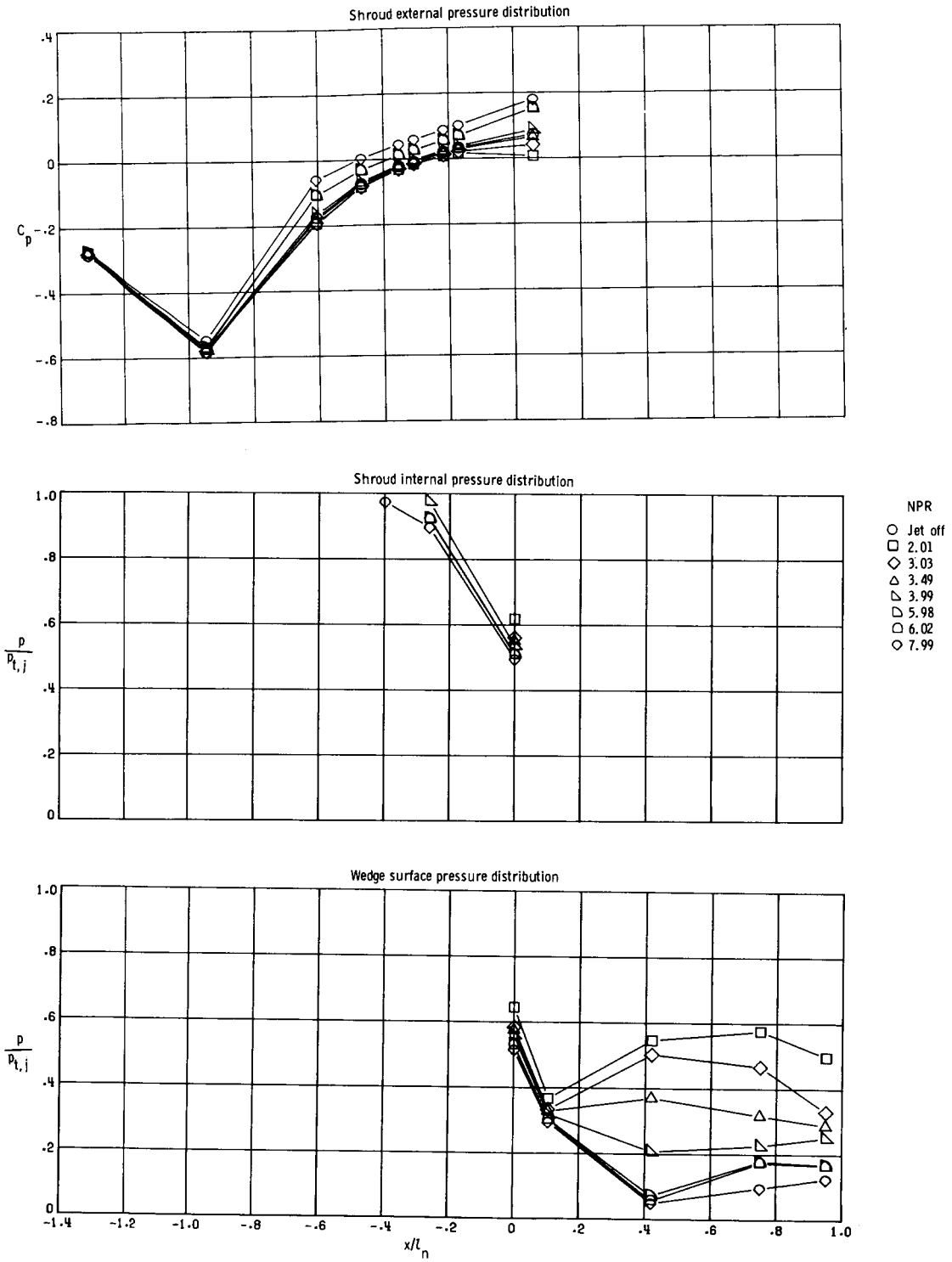

(d) $M = 0.94$.

Figure 13. Continued.

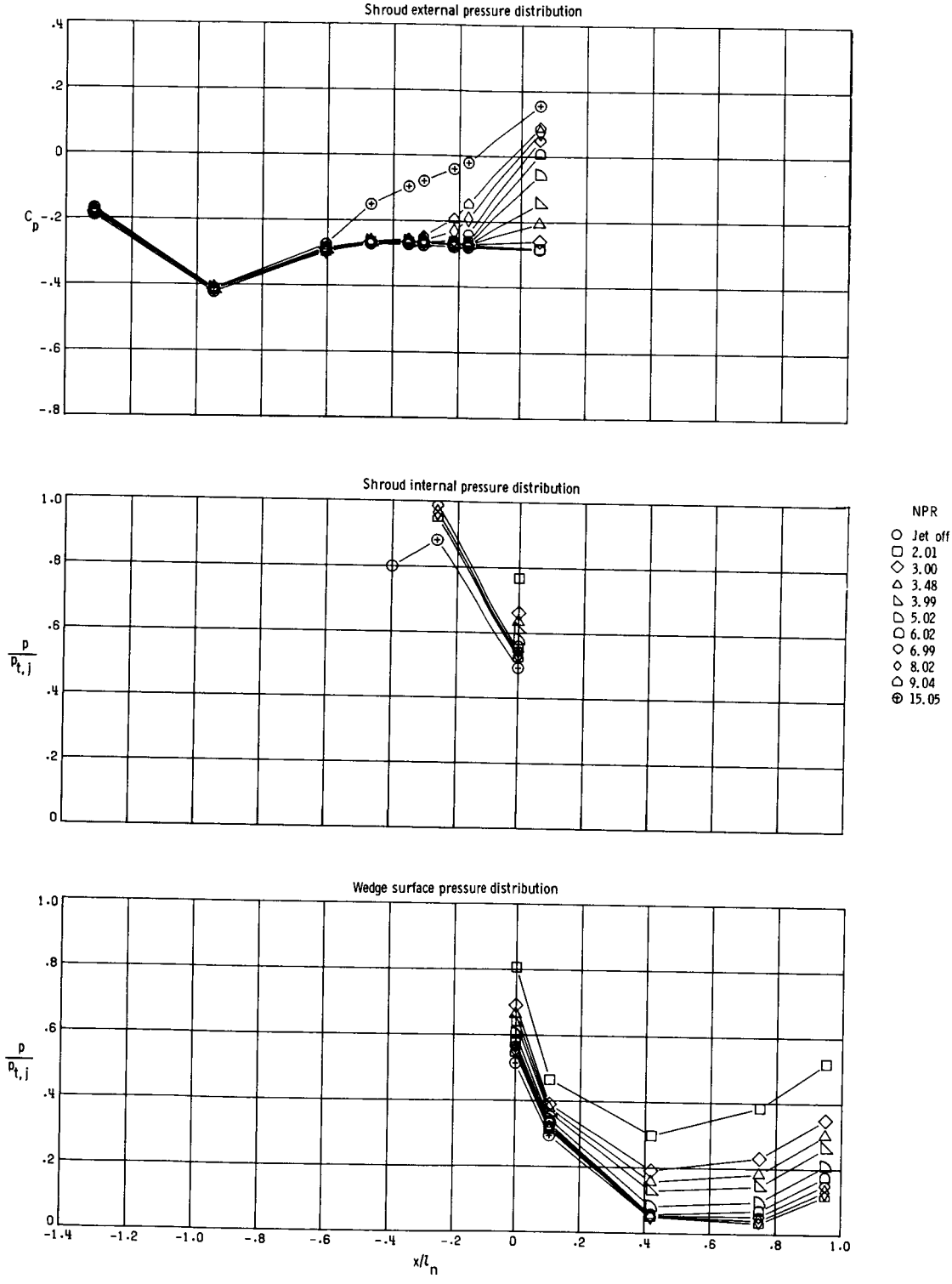

(e) $M = 1.20$.

Figure 13. Concluded.

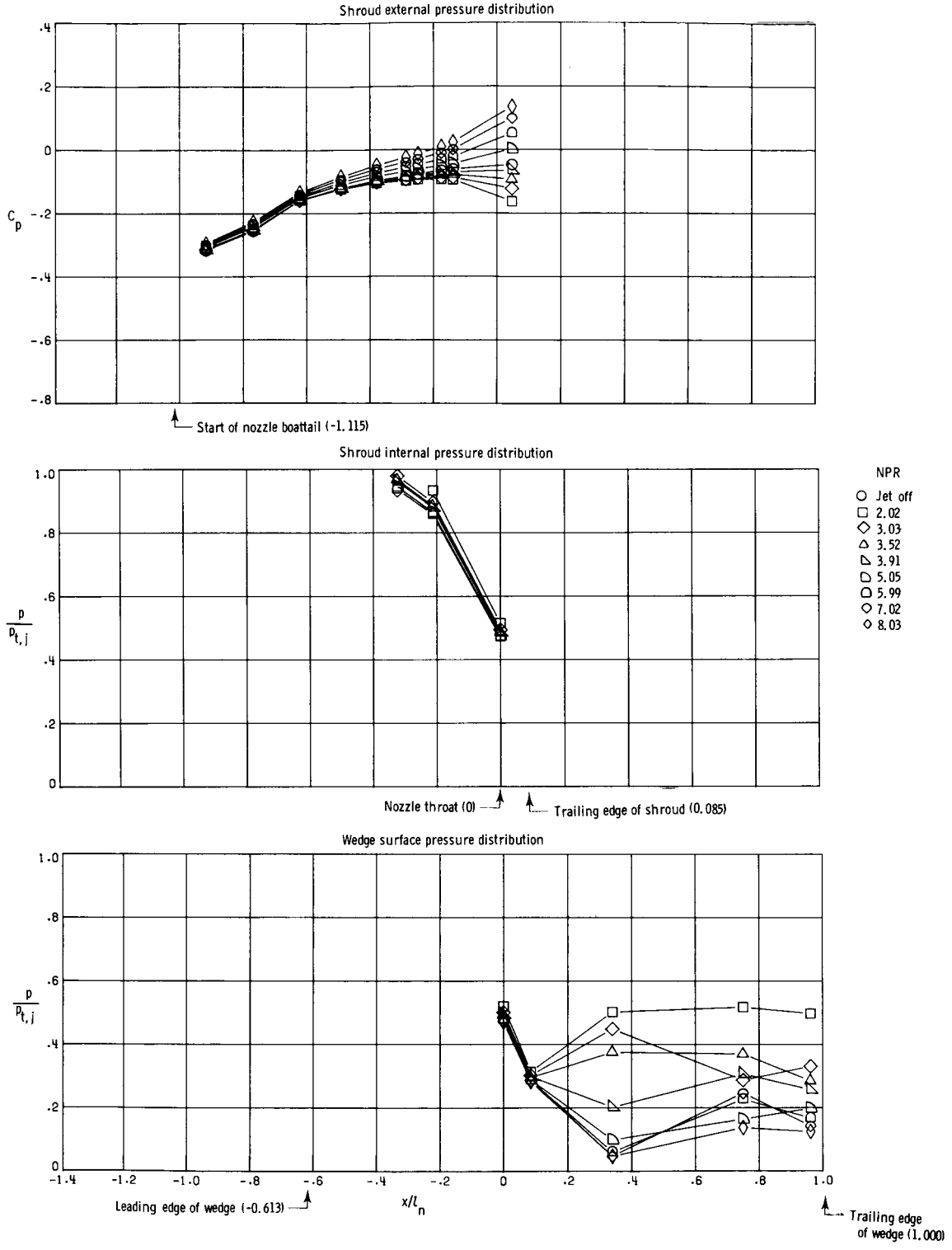

(a) $M = 0.60$.

Figure 14. External and internal surface pressure distributions $(y/(b_n/2) = 0.500)$ of configuration 2 Dry.

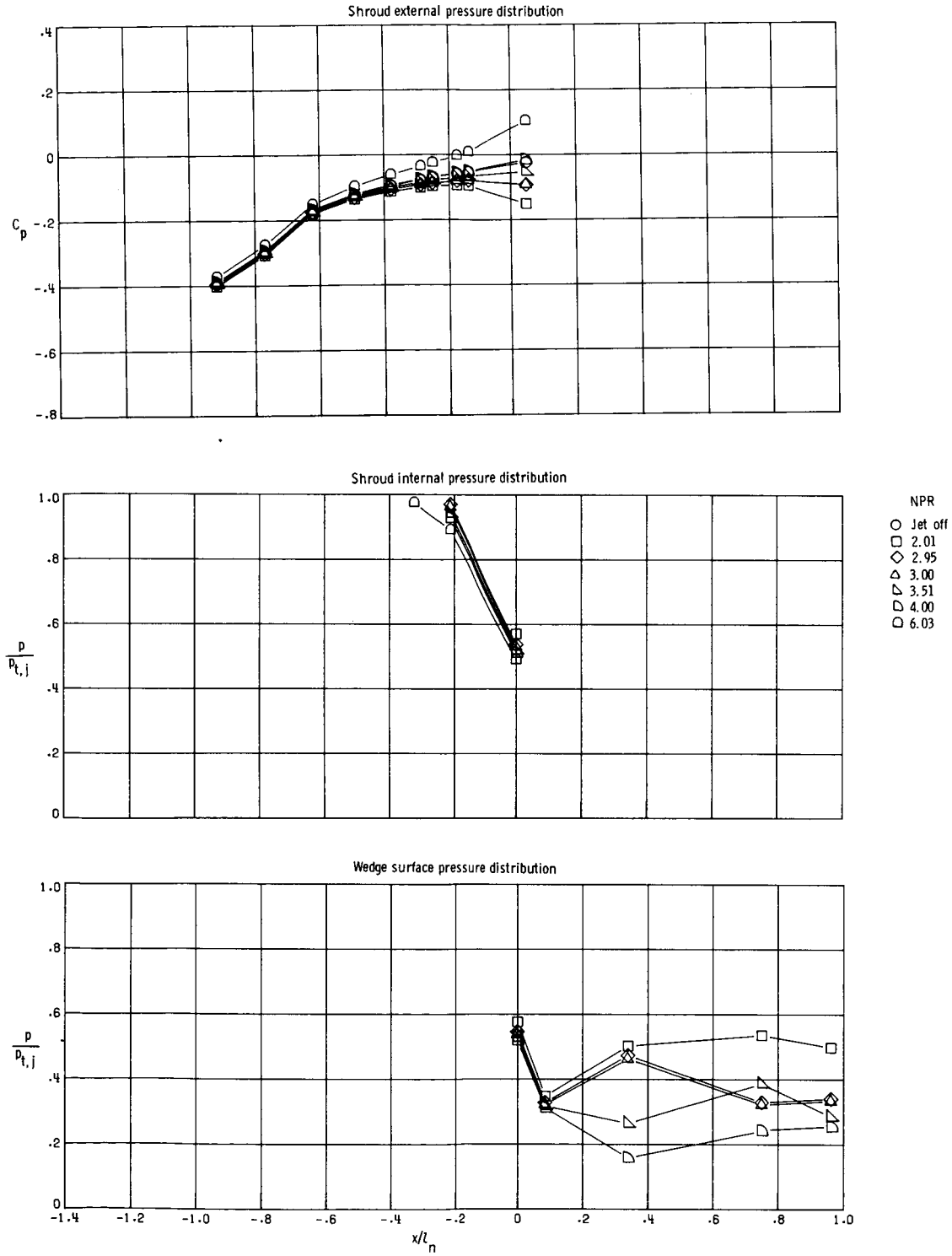

(b) $M = 0.80$.

Figure 14. Continued.

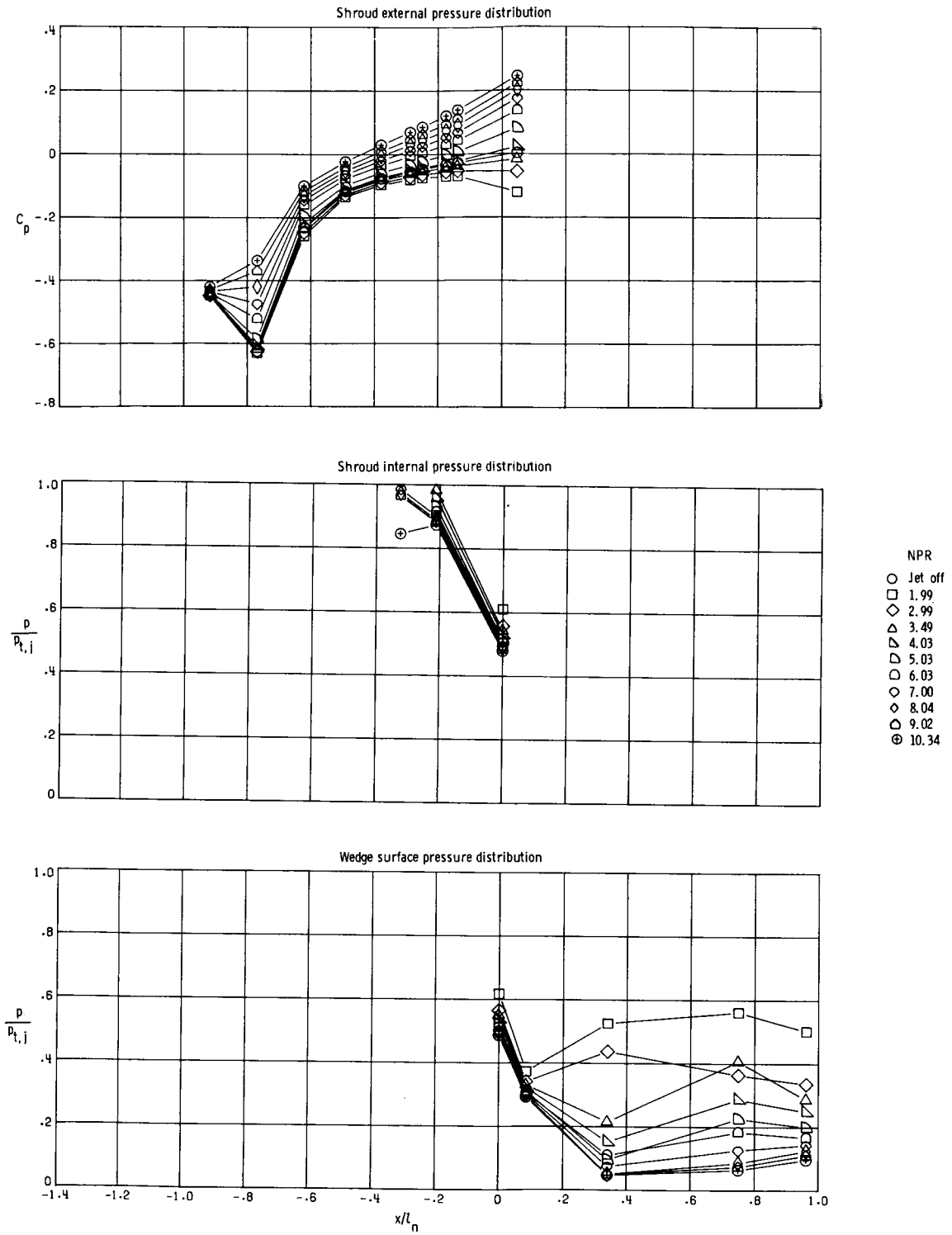

(c) $M = 0.90$.

Figure 14. Continued.

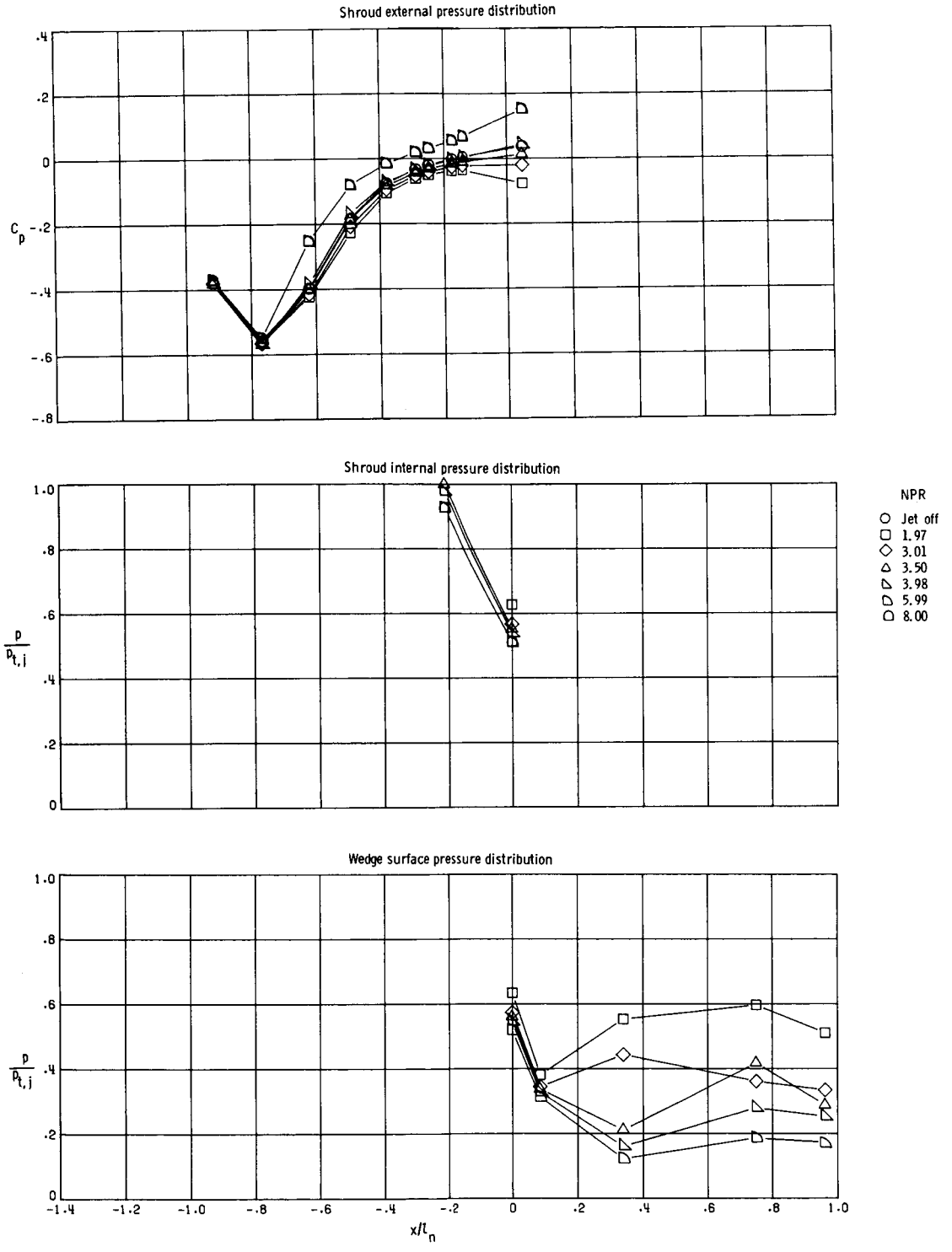

(d) $M = 0.94$.

Figure 14. Continued.

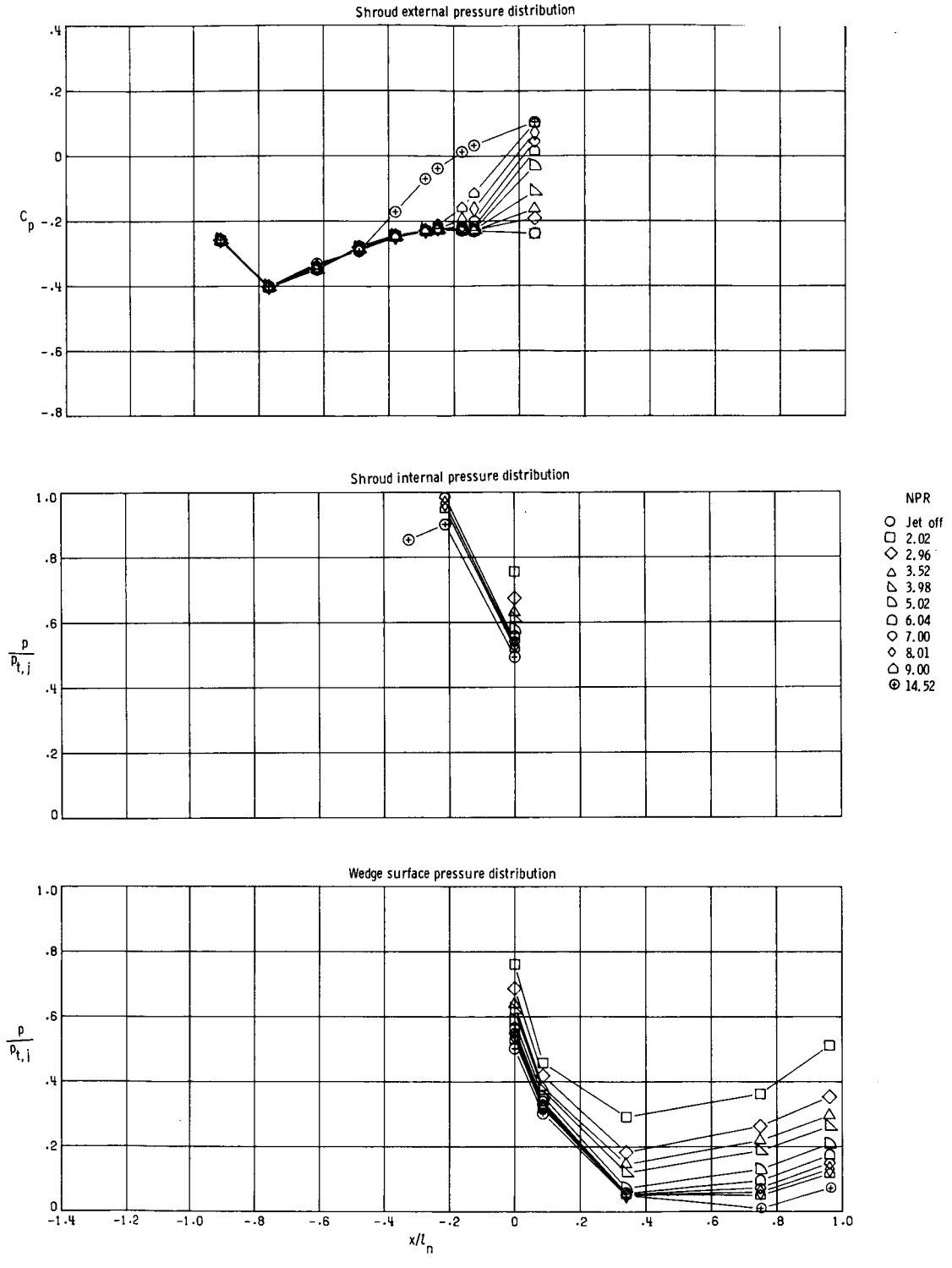

(e) $M = 1.20$.

Figure 14. Concluded.

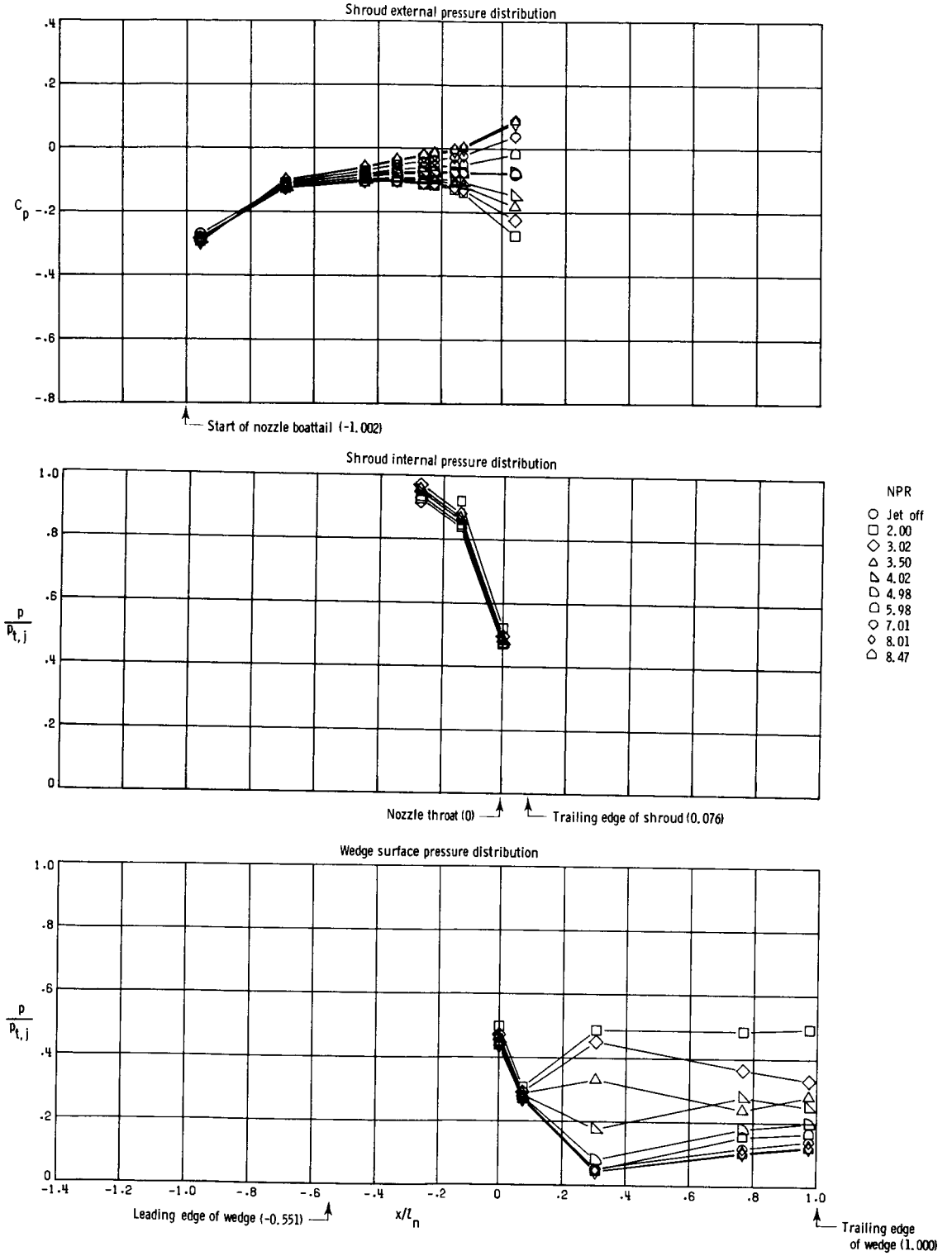

(a) $M = 0.60$.

Figure 15. External and internal surface pressure distributions $(y/(b_n/2) = 0.500)$ of configuration 3 Dry.

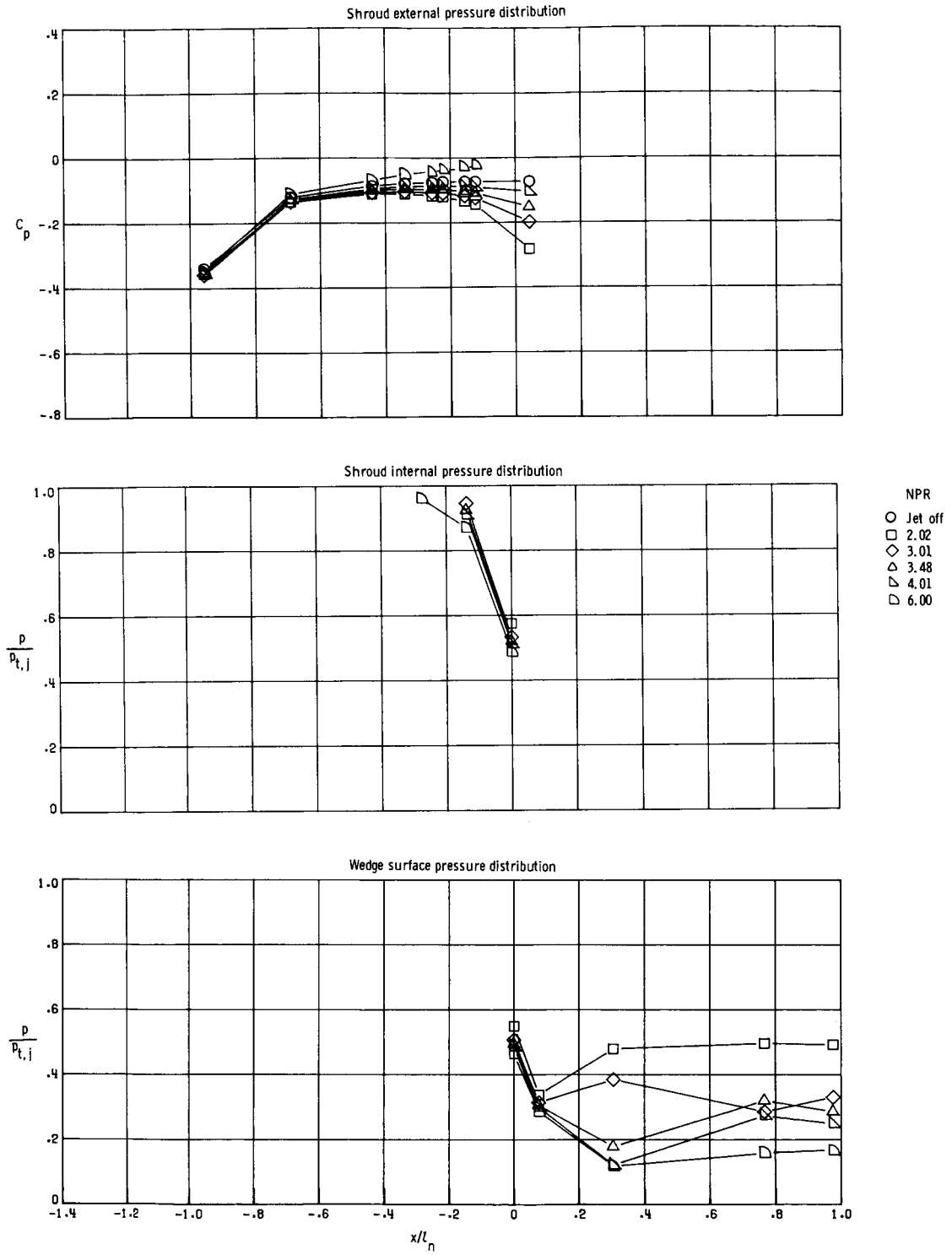

(b) $M = 0.80$.

Figure 15. Continued.

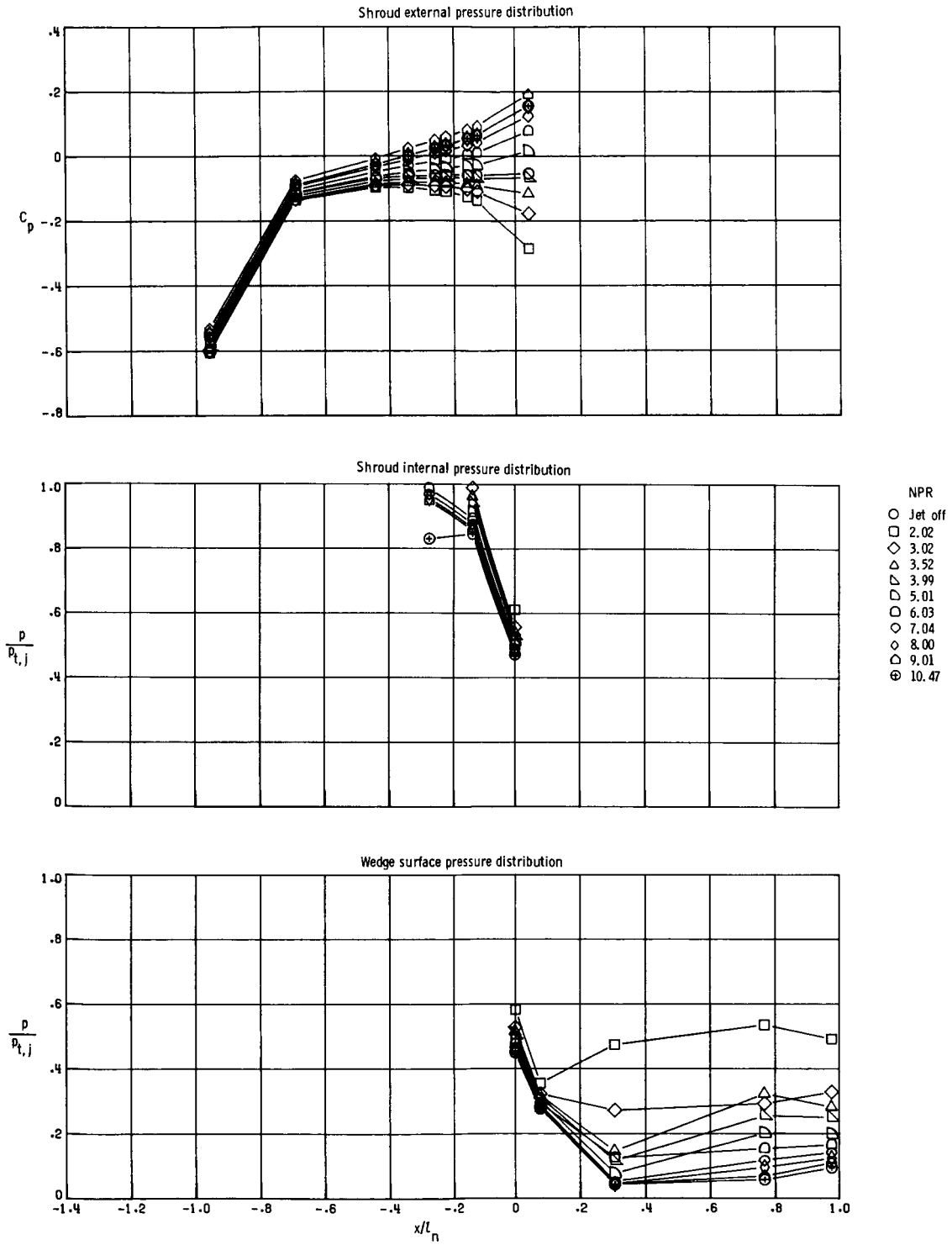

(c) $M = 0.90$.

Figure 15. Continued.

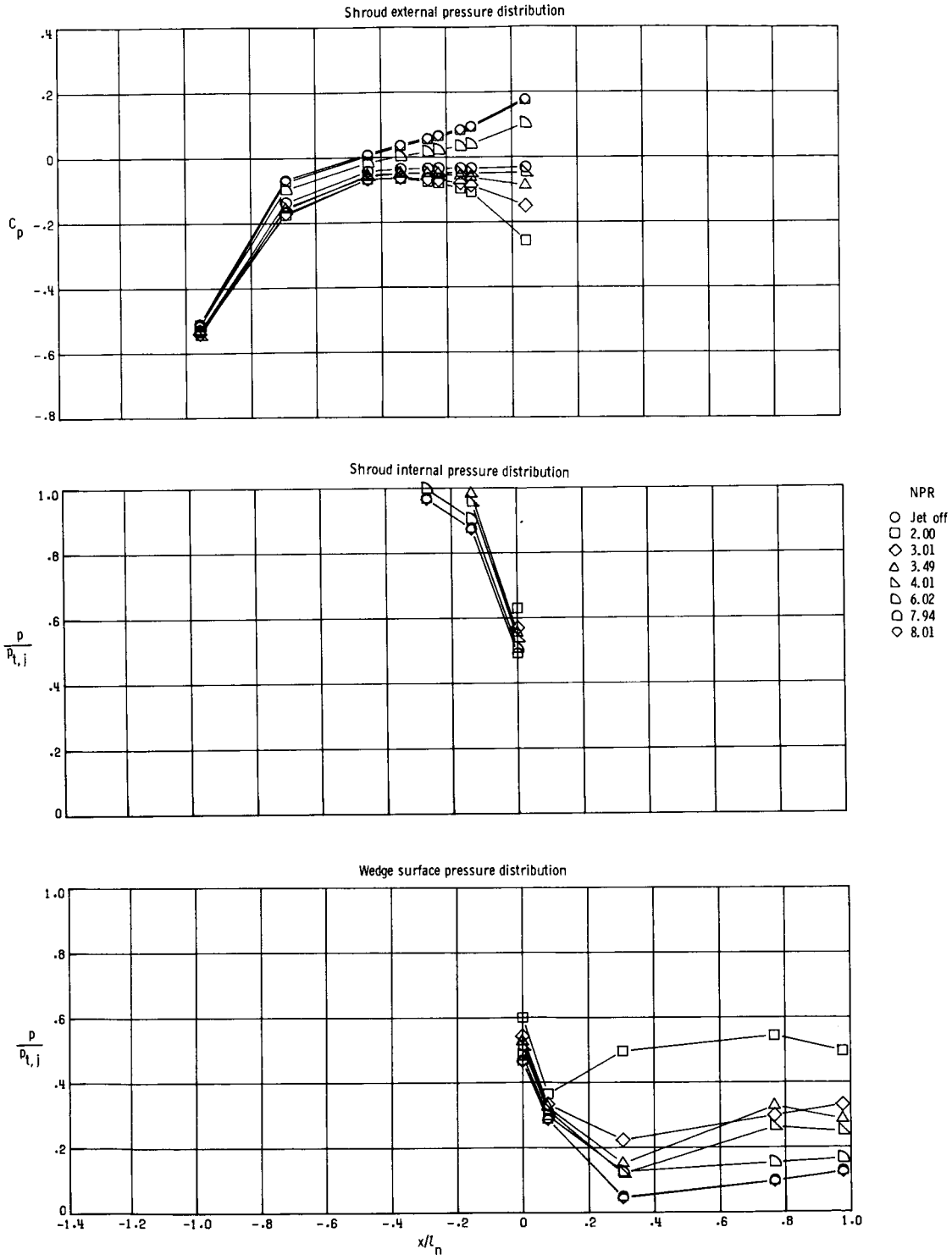

(d) $M = 0.94$.

Figure 15. Continued.

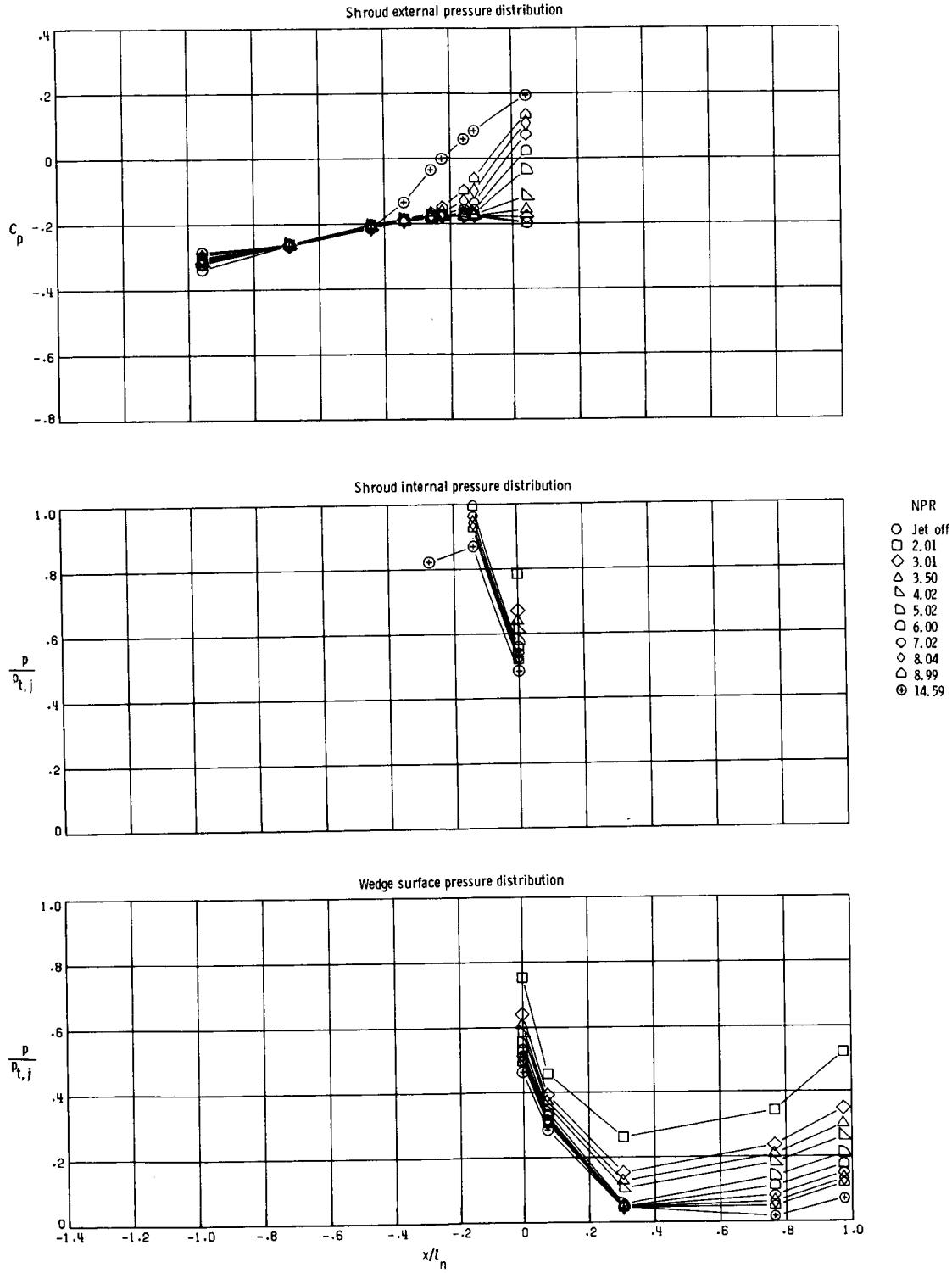

(e) $M = 1.20$.

Figure 15. Concluded.

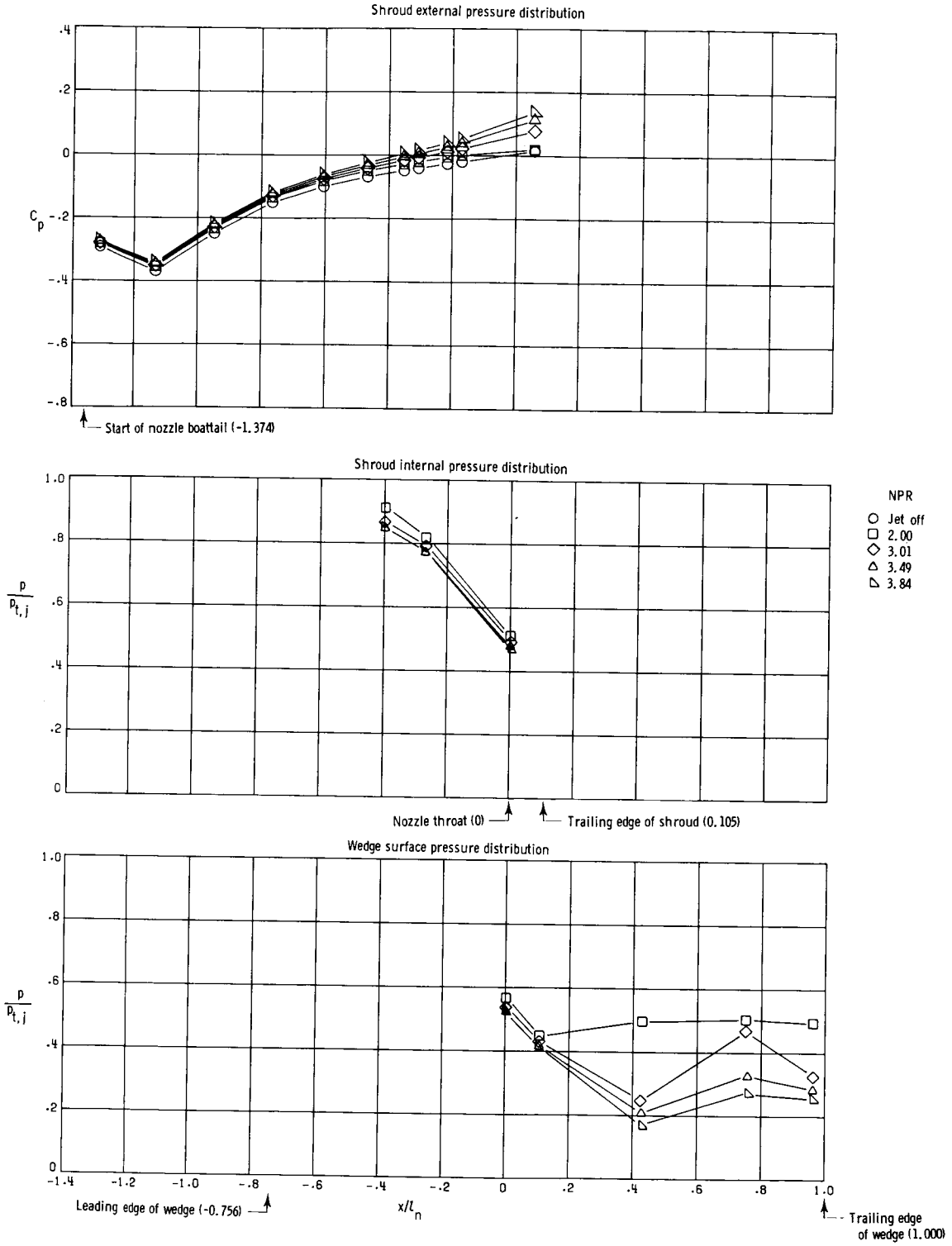

(a) $M = 0.60$.

Figure 16. External and internal surface pressure distributions $(y/(b_n/2) = 0.500)$ of configuration 1 A/B.

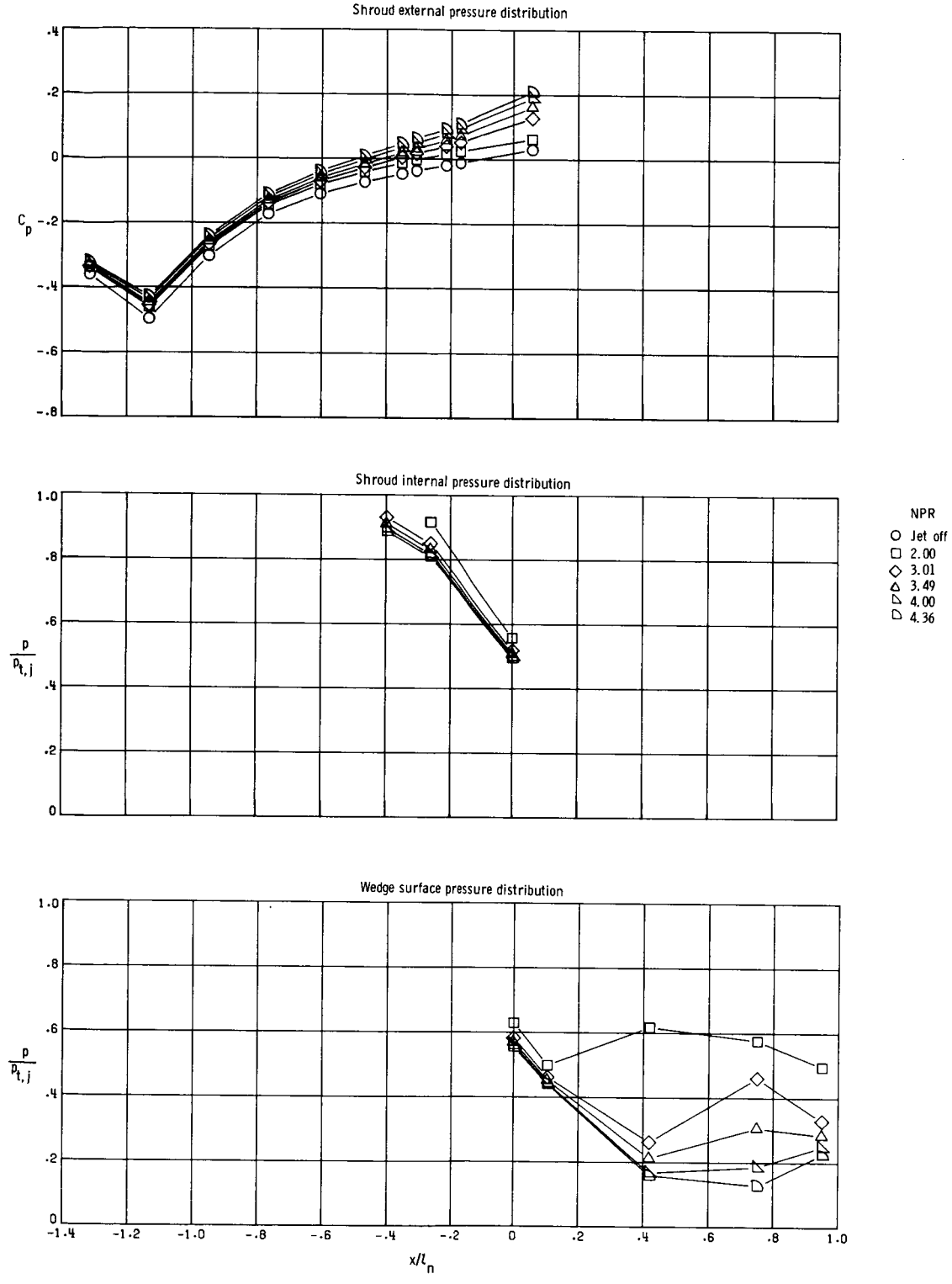

(b) $M = 0.80$.

Figure 16. Continued.

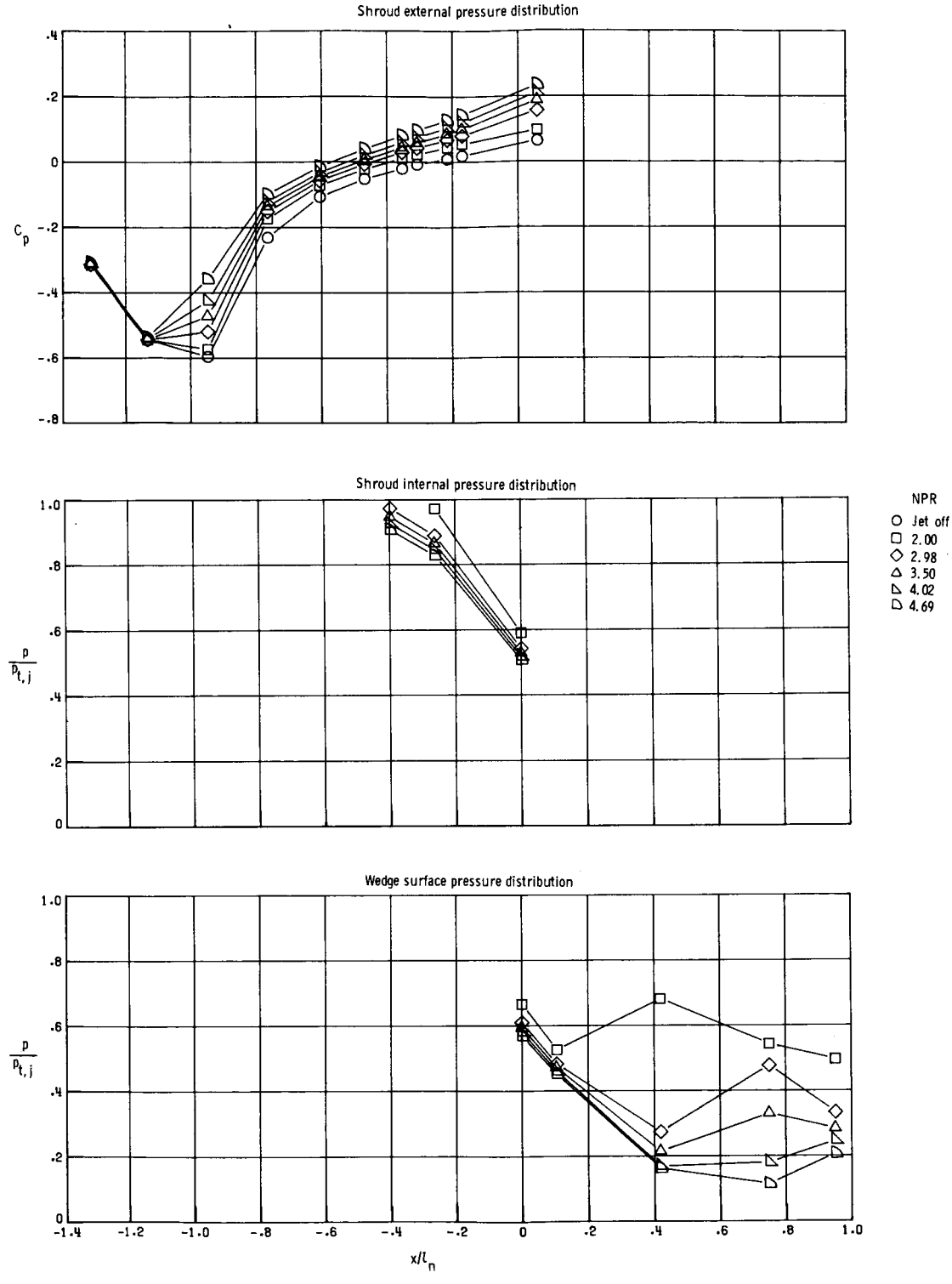

(c) $M = 0.90$.

Figure 16. Continued.

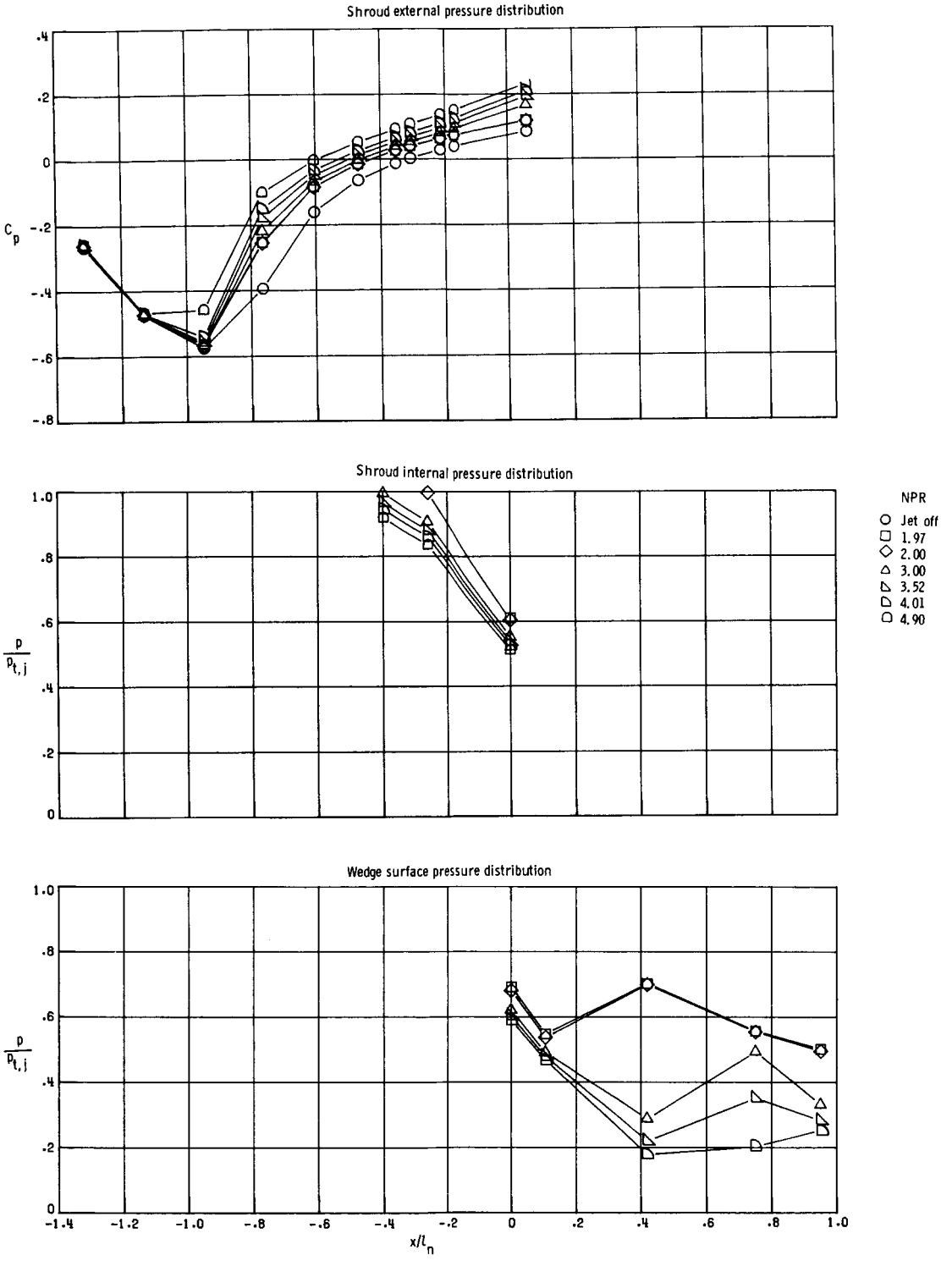

(d) $M = 0.94$.

Figure 16. Continued.

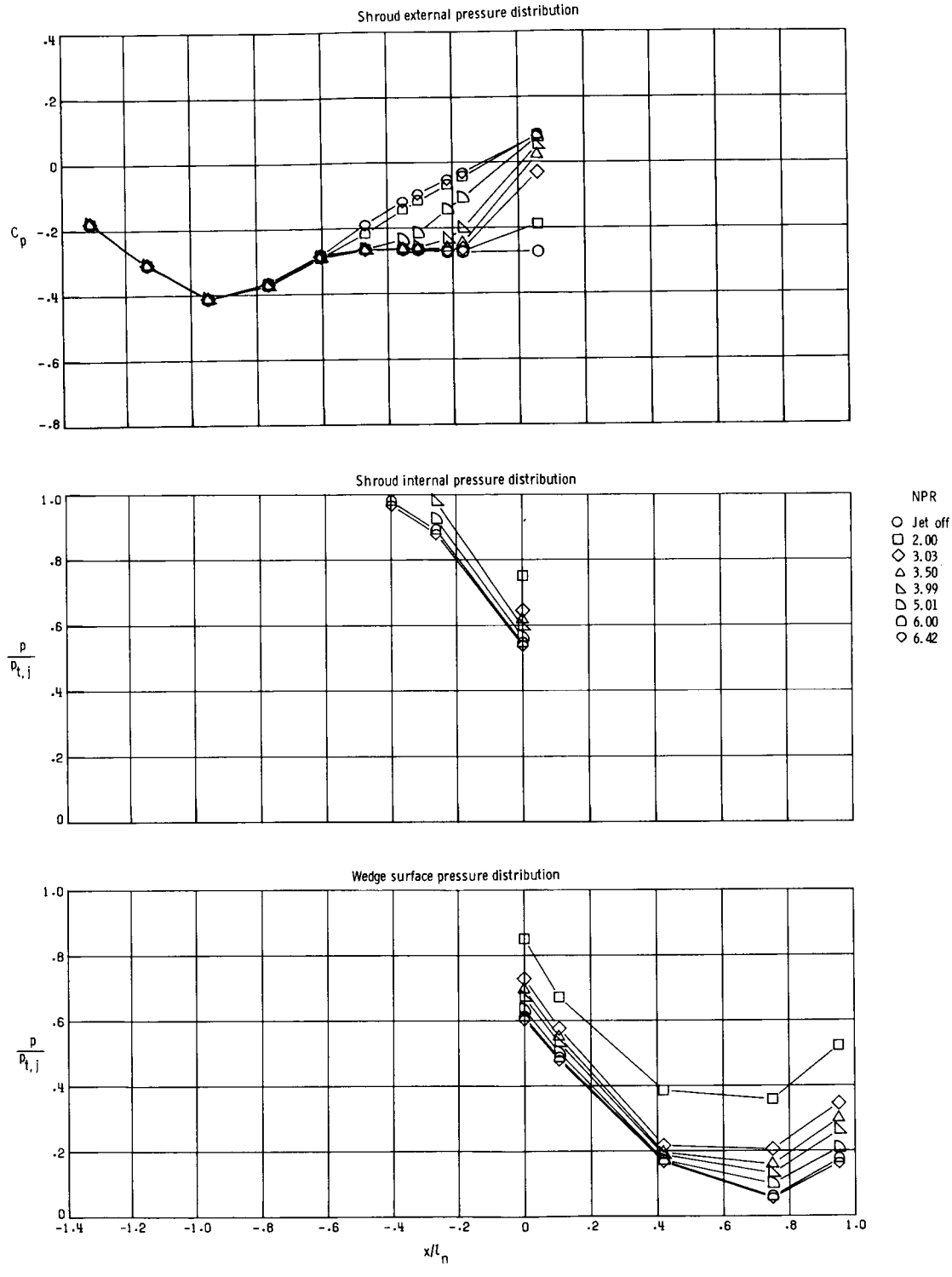

(e) $M = 1.20$.

Figure 16. Concluded.

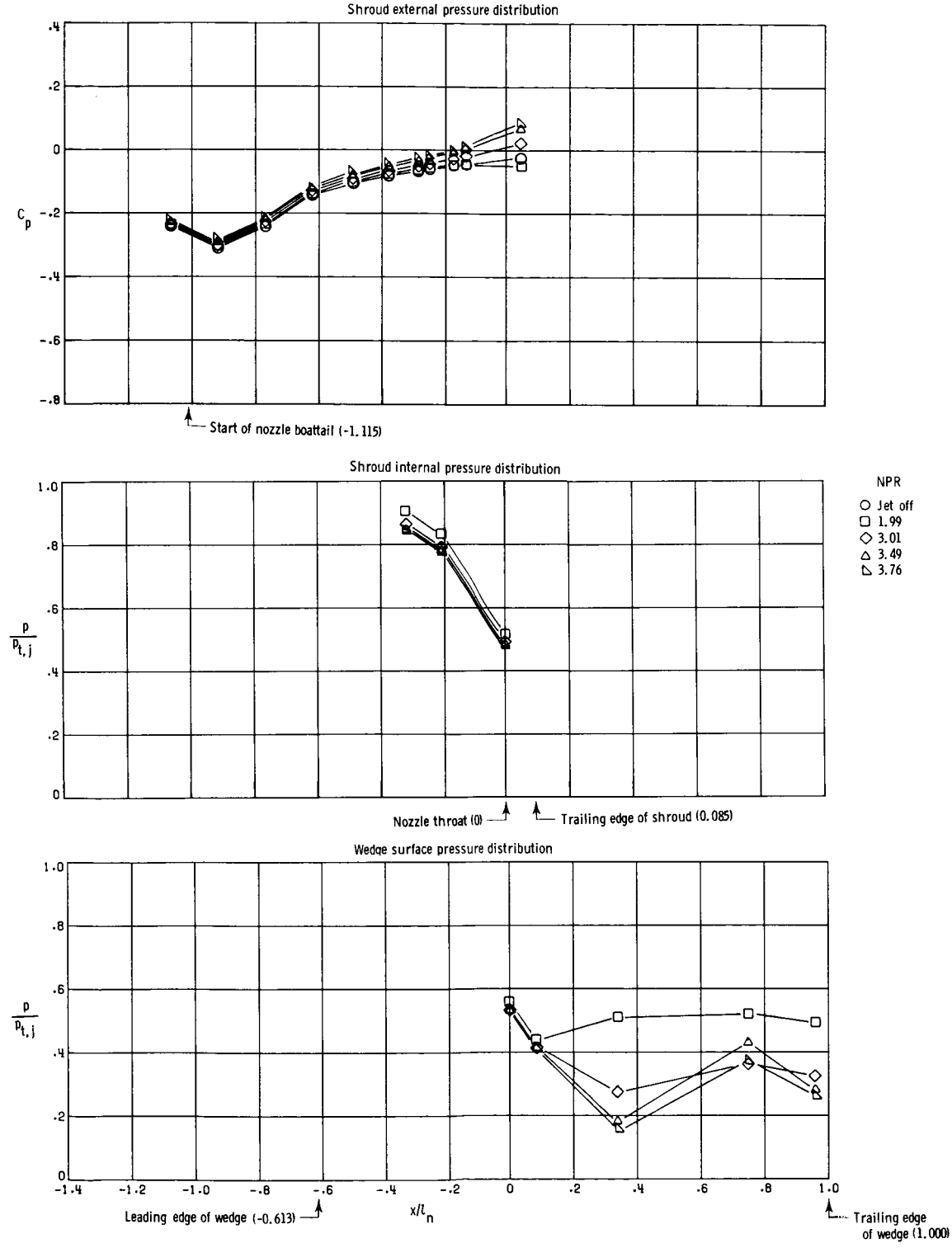

(a) $M = 0.60$.

Figure 17. External and internal surface pressure distributions $(y/(b_n/2) = 0.500)$ of configuration 2 A/B.

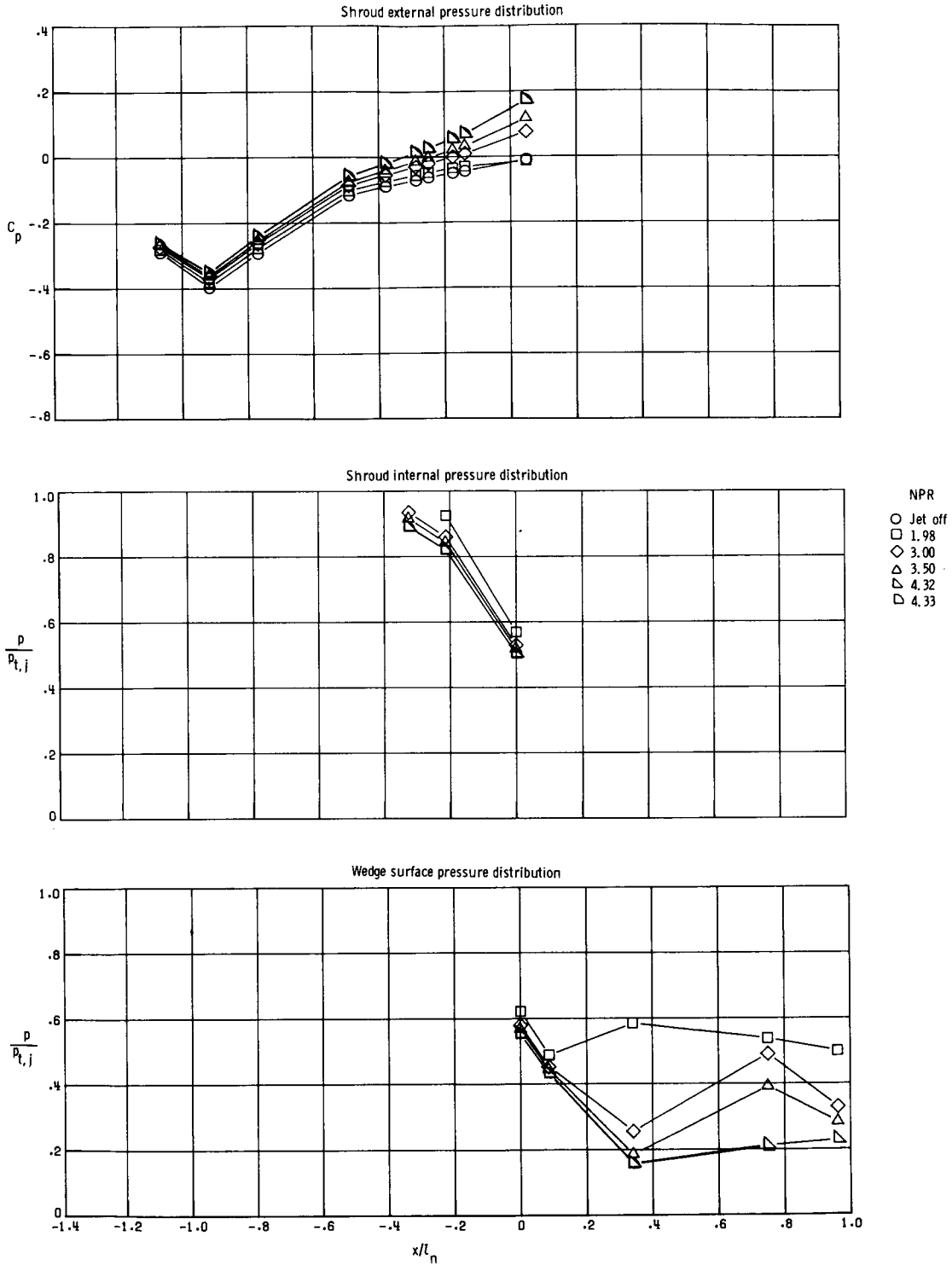

(b) $M = 0.80$.

Figure 17. Continued.

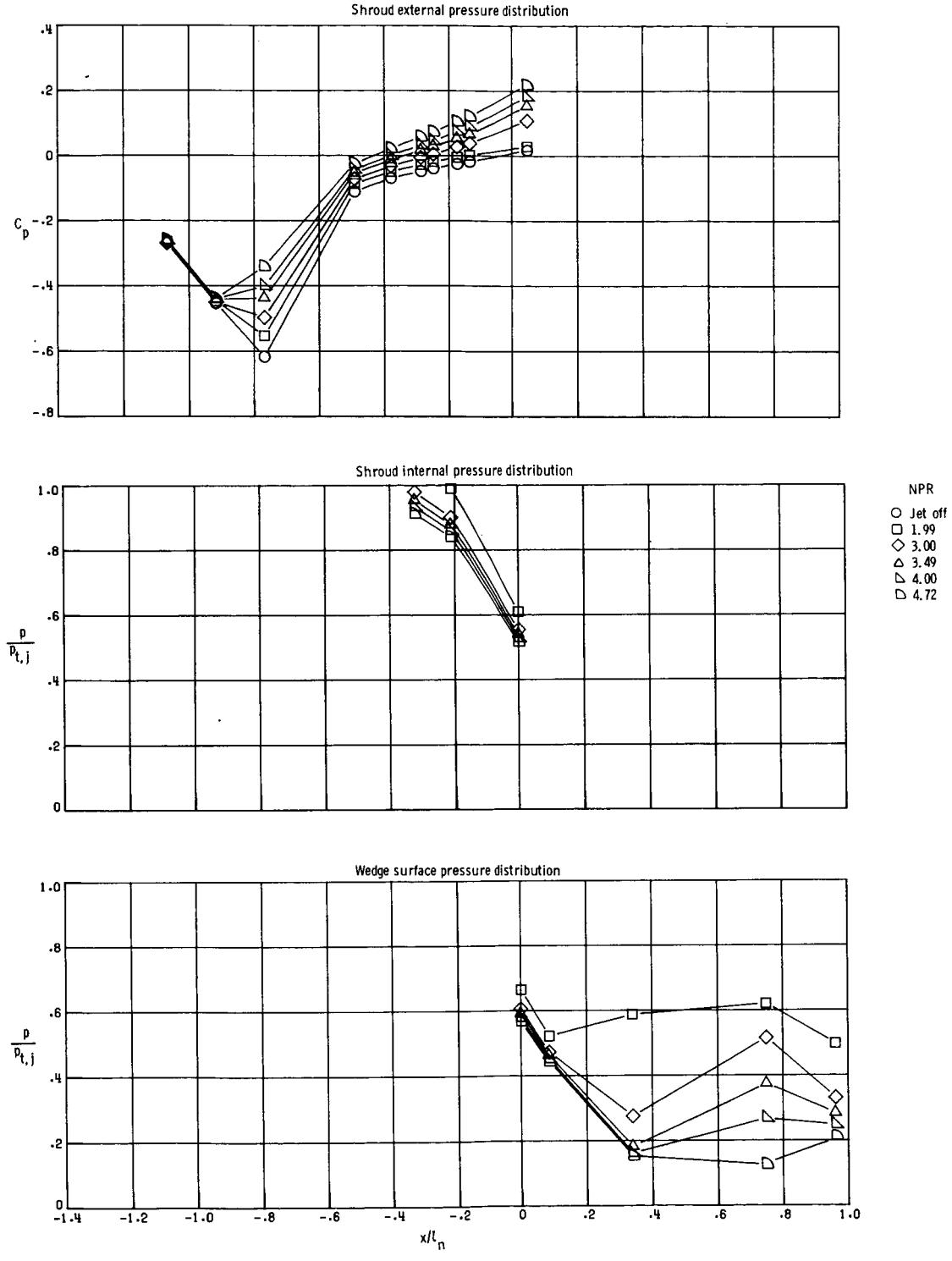

(c) $M = 0.90$.

Figure 17. Continued.

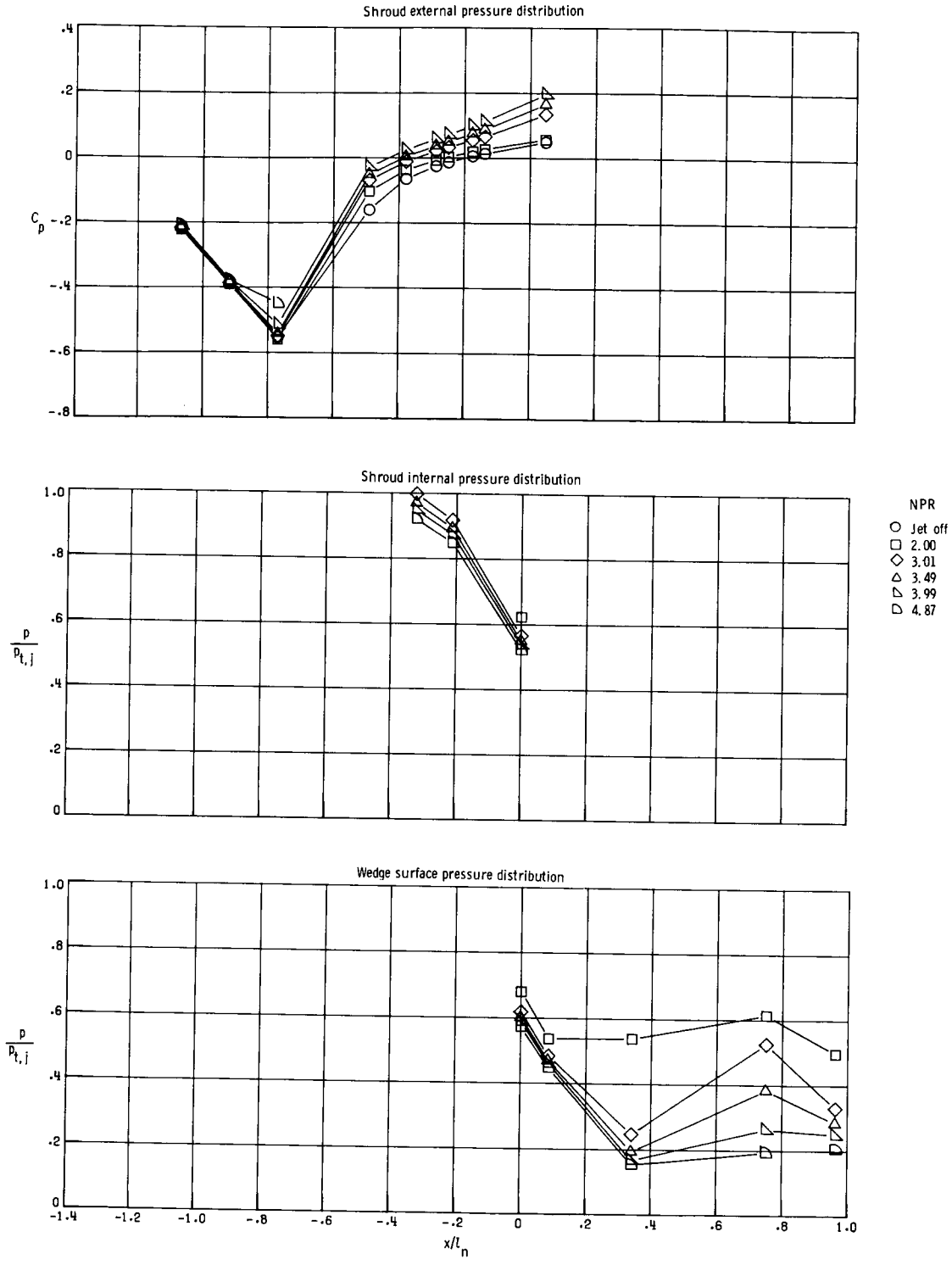

(d) $M = 0.94$.

Figure 17. Continued.

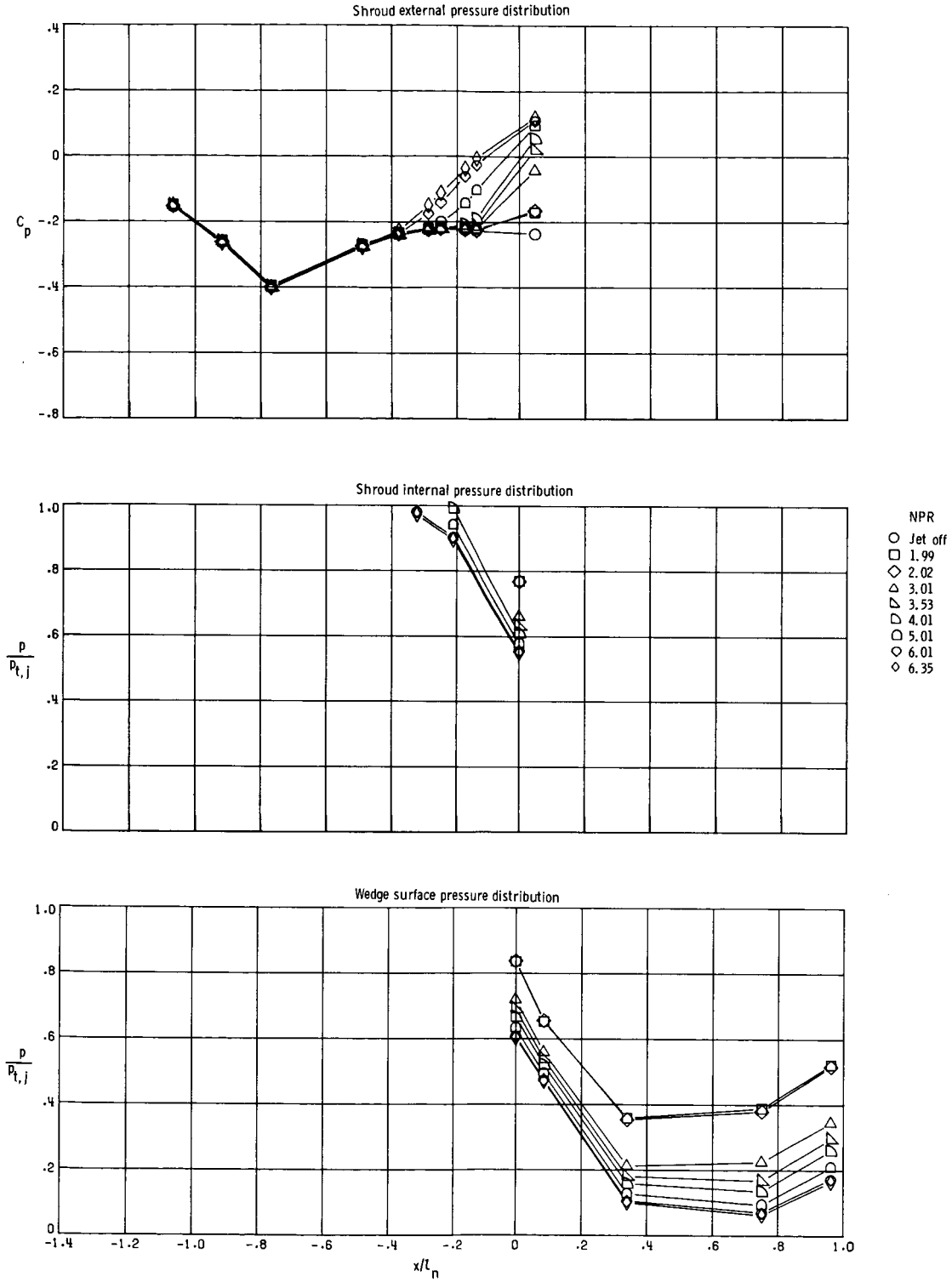

(e) $M = 1.20$.

Figure 17. Concluded.

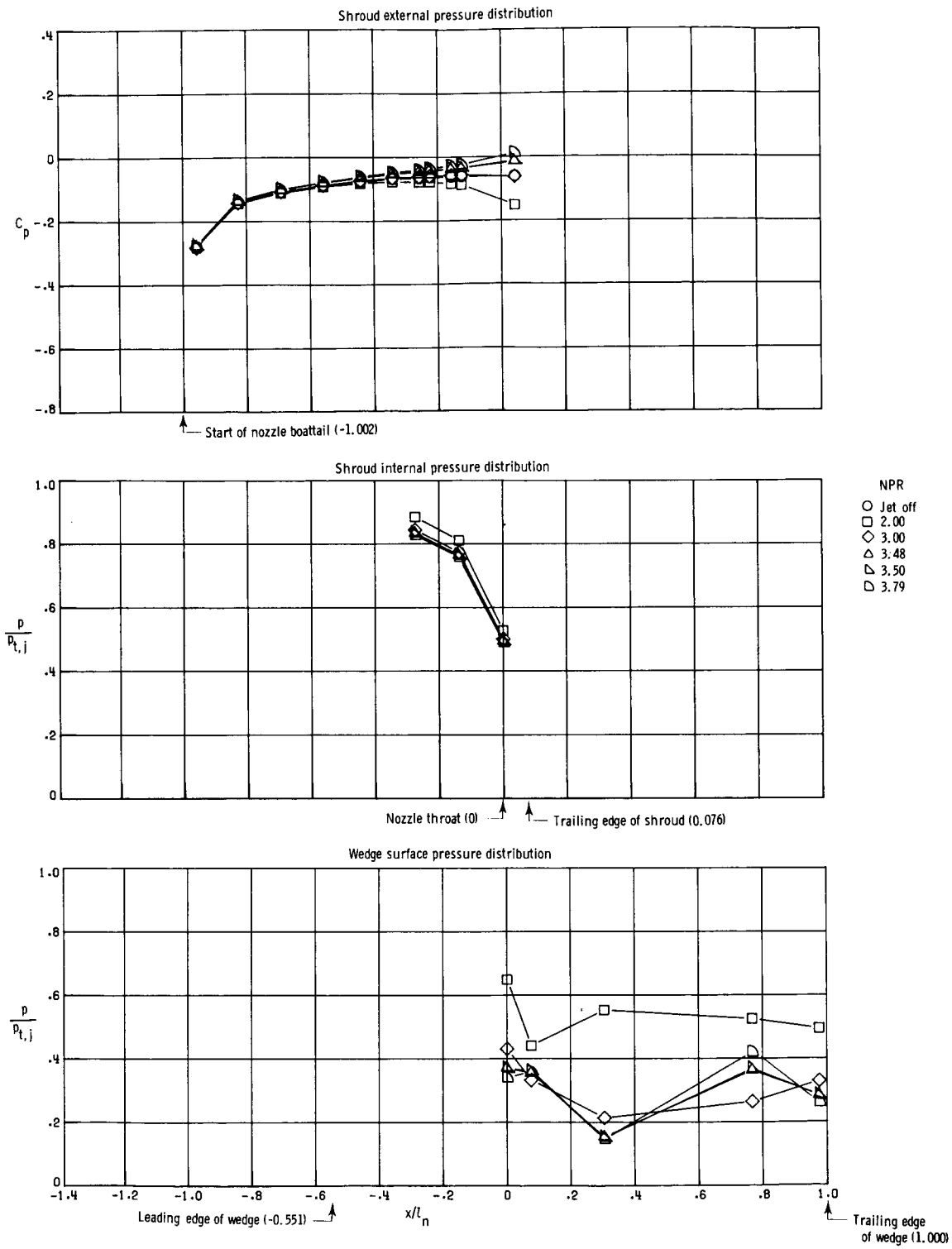

(a) $M = 0.60$.

Figure 18. External and internal surface pressure distributions $(y/(b_n/2) = 0.500)$ of configuration 3 A/B.

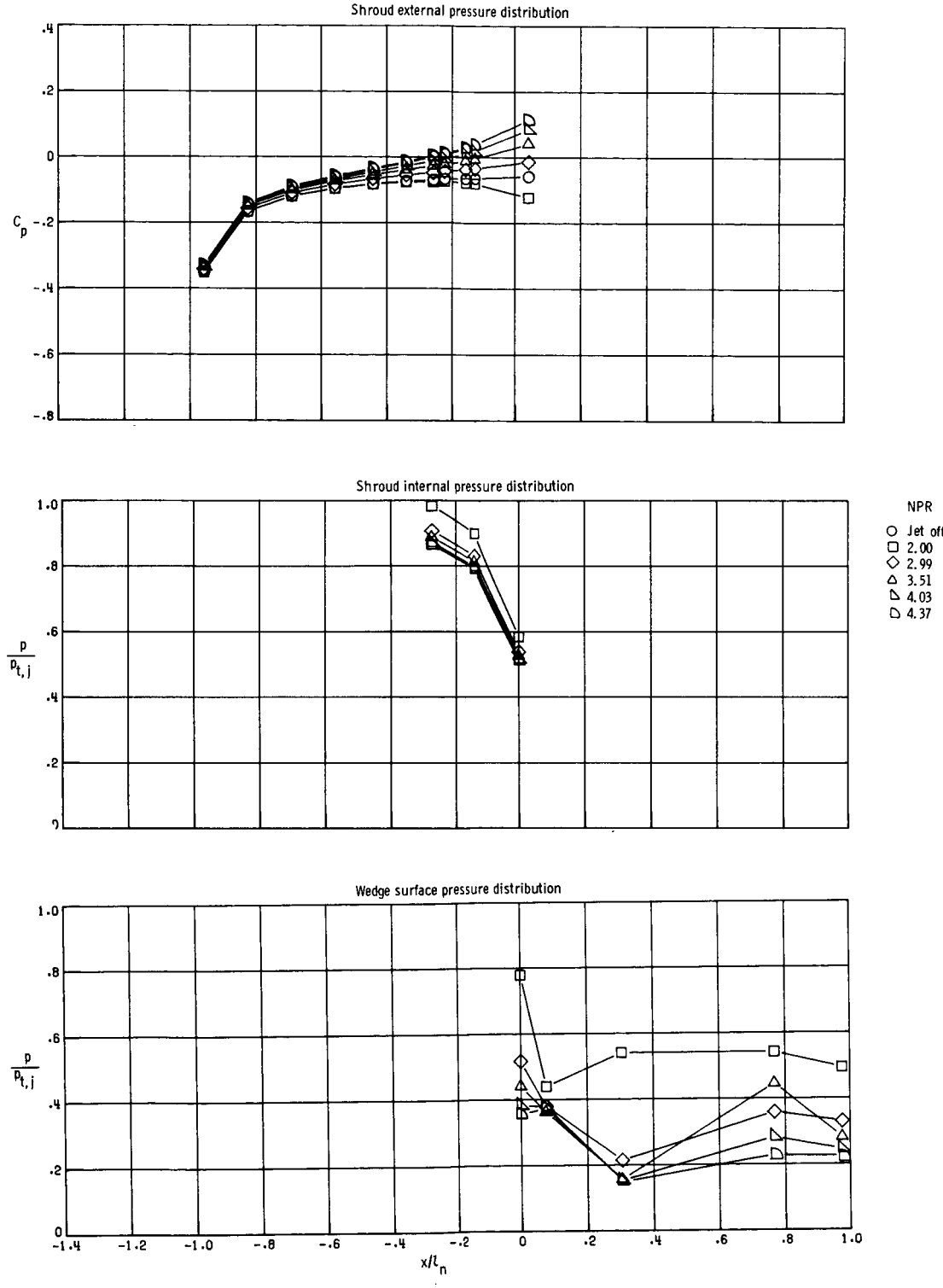

(b) $M = 0.80$.

Figure 18. Continued.

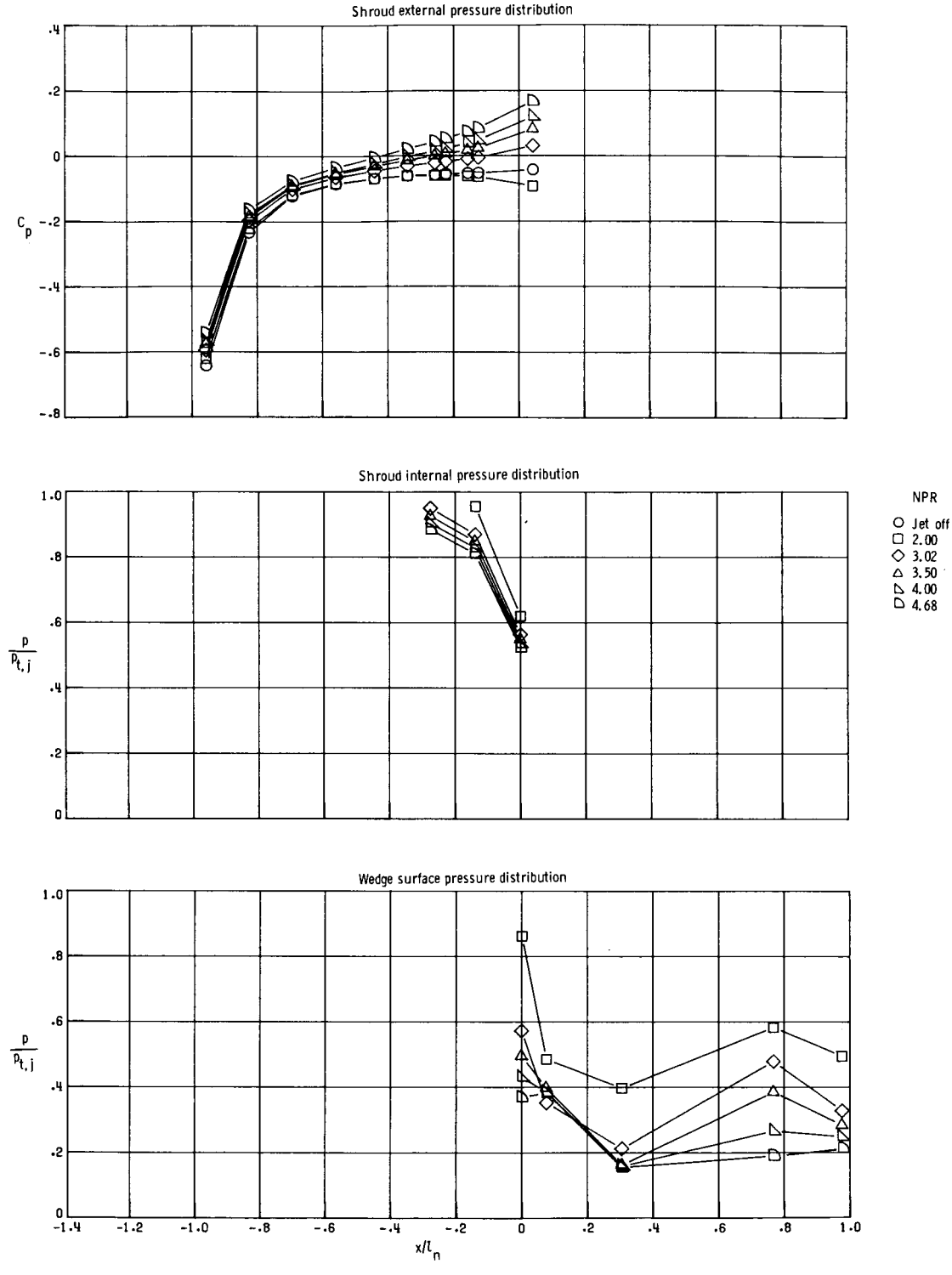

(c) $M = 0.90$.

Figure 18. Continued.

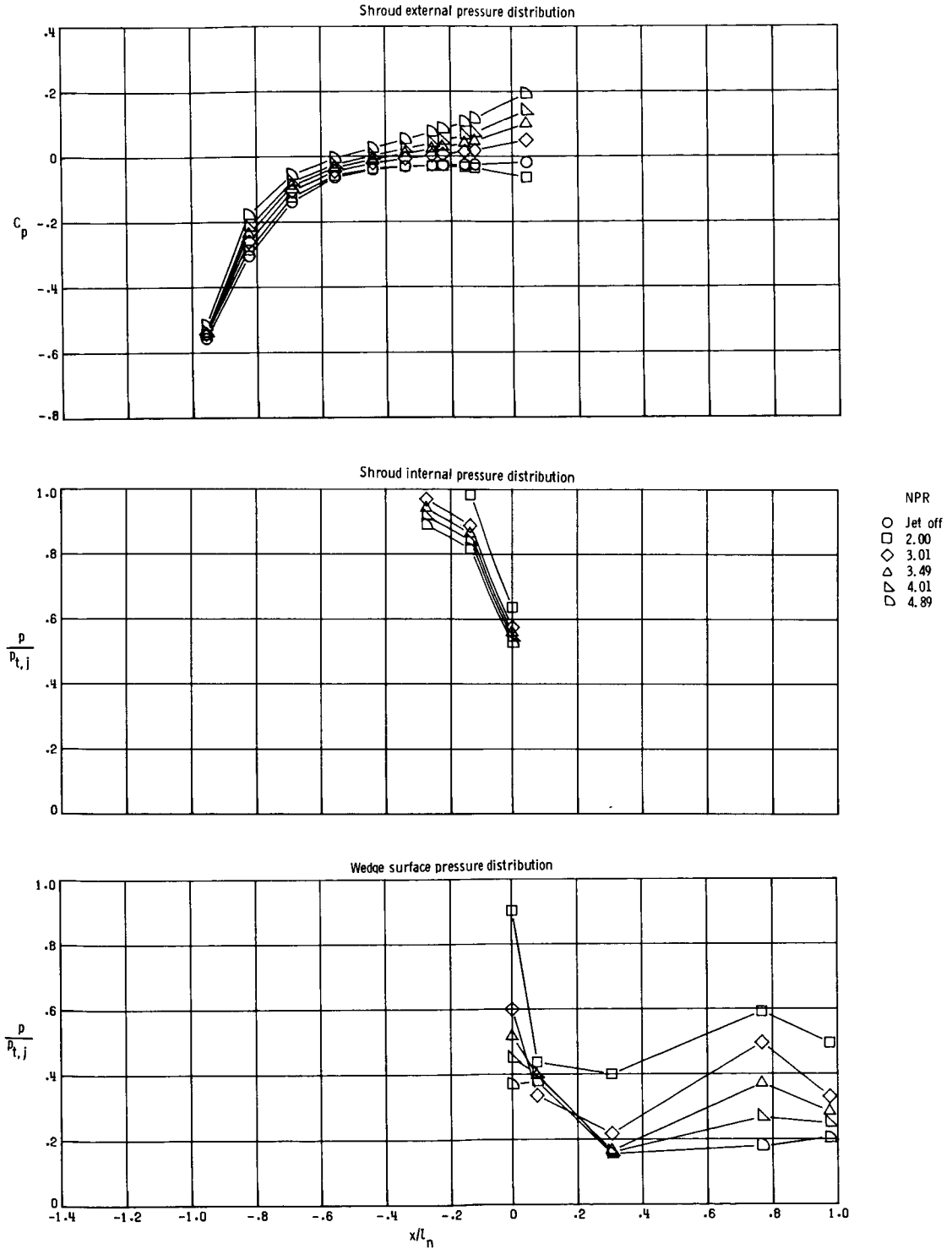

(d) $M = 0.94$.

Figure 18. Continued.

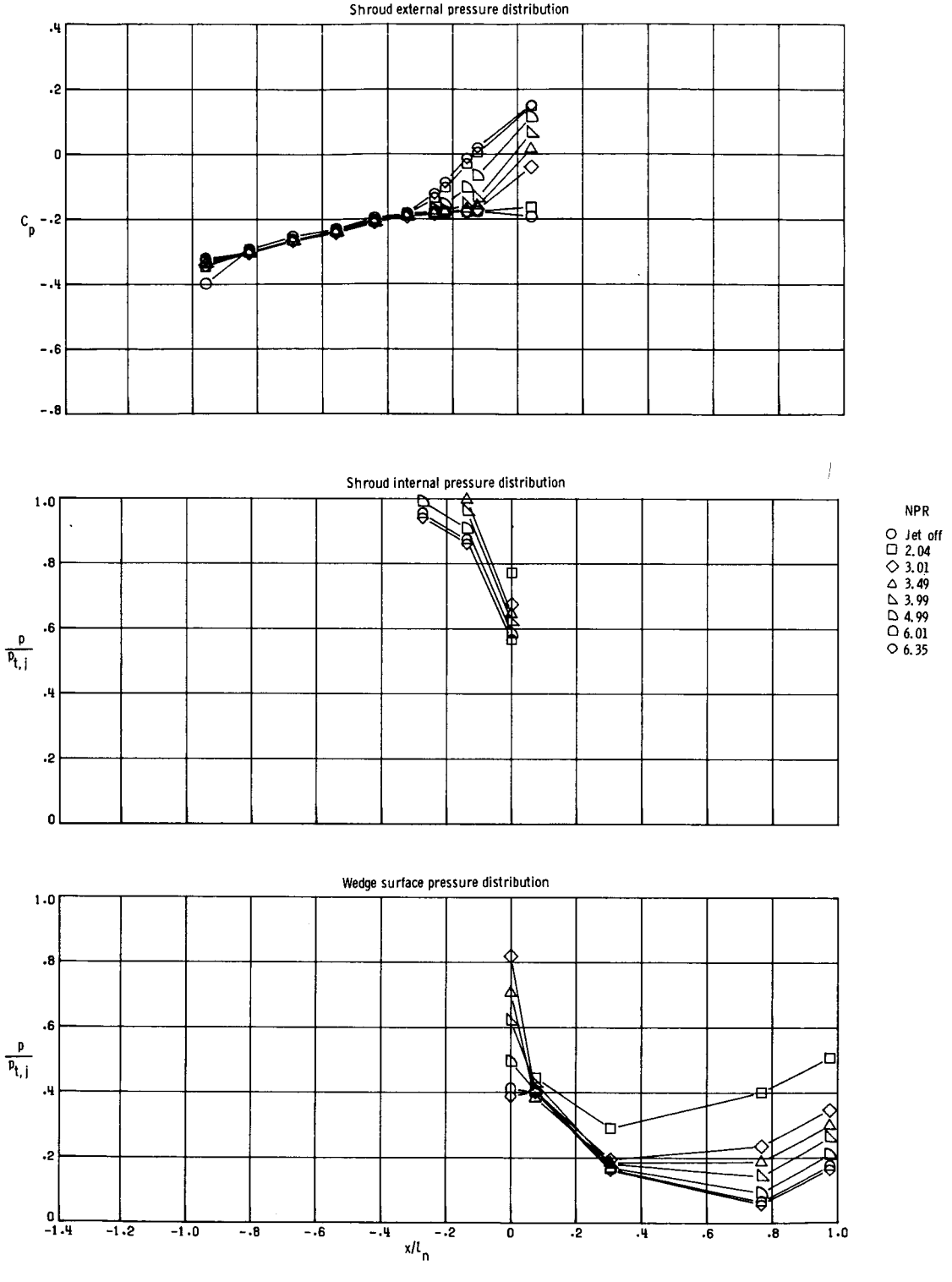

(e) $M = 1.20$.

Figure 18. Concluded.

NASA
National Aeronautics and Space Administration

Report Documentation Page

1. Report No.	2. Government Accession No.	3. Recipient's Catalog No.
NASA TP-2717		

4. Title and Subtitle	5. Report Date
Effect of a Trade Between Boattail Angle and Wedge Size on the Performance of a Nonaxisymmetric Wedge Nozzle	July 1987
	6. Performing Organization Code
7. Author(s)	8. Performing Organization Report No.
George T. Carson, Jr., E. Ann Bare, and James R. Burley II	L-16248
9. Performing Organization Name and Address	10. Work Unit No.
NASA Langley Research Center Hampton, VA 23665-5225	505-62-91-01
	11. Contract or Grant No.
12. Sponsoring Agency Name and Address	13. Type of Report and Period Covered
National Aeronautics and Space Administration Washington, DC 20546-0001	Technical Paper
	14. Sponsoring Agency Code

15. Supplementary Notes

16. Abstract

An investigation was conducted in the Langley 16-Foot Transonic Tunnel to determine the effect of a boattail-angle and wedge-size trade on the performance of nonaxisymmetric wedge nozzles installed on a generic twin-engine fighter aircraft model. Test data were obtained at static conditions and at Mach numbers from 0.60 to 1.25. Angle of attack was held constant at 0°. High-pressure air was used to simulate jet exhaust, and the nozzle pressure ratio was varied from 1.0 (jet off) to slightly over 15.0. For the configurations studied, the results indicate that wedge size can be reduced without affecting aeropropulsive performance.

17. Key Words (Suggested by Authors(s))
Nonaxisymmetric nozzles
Wedge nozzles
Nozzle boattail angle

18. Distribution Statement
Unclassified—Unlimited

Subject Category 02

19. Security Classif.(of this report)	20. Security Classif.(of this page)	21. No. of Pages	22. Price
Unclassified	Unclassified	65	A04

NASA FORM 1626 OCT 86

NASA-Langley, 1987

For sale by the National Technical Information Service, Springfield, Virginia 22161-2171